TAMPEREEN TEKNILLINEN YLIOPISTO
TAMPERE UNIVERSITY OF TECHNOLOGY

Outi Vilhelmiina Kontkanen

Modeling of Charge Transfer at Dye-Semiconductor Interfaces in p-type Solar Cells

Julkaisu 1530 • Publication 1530

Tampere 2018

Tampereen teknillinen yliopisto. Julkaisu 1530
Tampere University of Technology. Publication 1530

Outi Vilhelmiina Kontkanen

Modeling of Charge Transfer at Dye-Semiconductor Interfaces in p-Type Solar Cells

Thesis for the degree of Doctor of Science in Technology to be presented with due permission for public examination and criticism in Festia Building, Auditorium Pieni Sali 1, at Tampere University of Technology, on the 2nd of March 2018, at 12 noon.

Tampereen teknillinen yliopisto - Tampere University of Technology
Tampere 2018

Doctoral candidate: Outi Vilhelmiina Kontkanen
Laboratory of Physics
Faculty of Natural Sciences
Tampere University of Technology
Finland

Supervisors: Tapio Rantala, Professor
Laboratory of Physics
Faculty of Natural Sciences
Tampere University of Technology
Finland

David Beljonne, Doctor of Philosophy
Laboratory of Novel Materials
Faculty of Science
University of Mons
Belgium

Instructor: Terttu Hukka, Adjunct professor
Laboratory of Chemistry and Bioengineering
Faculty of Natural Sciences
Tampere University of Technology
Finland

Pre-examiners: Mikko Linnolahti, Associate professor
Department of Chemistry
University of Eastern Finland
Finland

Philip Hoggan, Professor
Institut Pascalgma
Université Clermont Auvergne
France

Opponent: Egbert Zojer, Professor
Institute of Solid State Physics
Graz University of Technology
Austria

ISBN 978-952-15-4097-4 (printed)
ISBN 978-952-15-4107-0 (PDF)
ISSN 1459-2045

Abstract

Dye-sensitized solar cells are composed of cheap and recyclable materials. These colorful and flexible cells convert sunlight into renewable energy. However, dye-sensitized solar cells are inefficient due to their low-charge current. The goal of this thesis is thus to create better understanding of the various components of these cells in order to improve their efficiencies. The main focus of dye-sensitized solar energy research lies in charge-transfer reactions between three main components: dye molecule; semiconductor surface, and electrolyte. In dye-sensitized solar cells, the charge is transferred from the excited dye molecule to the semiconductor surface. The charge is then transported to the electrode to create the electric current.

The studied components are derivatives of boron-dipyrromethene, perylene monoimide, and trisphenyl amine as dye molecules. Nickel oxide and titanium dioxide are used as semiconductor surfaces. The studied anchoring groups are carboxylate, 1,2-diol, and pyridine. These are studied in isolation, and then, their interactions in contact are investigated. In this study theoretical modeling is used, which includes the hybrid functional B3LYP and CRYSTAL09 software. The hybrid functional, B3LYP, is not widely used in studies within periodic boundary conditions such as dye-semiconductor interfaces. Thus, the mentioned systems have not been studied earlier at this level of theory.

In the first part of the study, the isolated systems, namely derivatives boron-dipyrromethene and titanium dioxide, are investigated. Results with BODIPY show that i) the vinylene group makes no difference for the electron transition nor orbital localization of orbitals, ii) phosphonate draws the most and carboxyl the least amount of the electron localization from the anchor, iii) methyl groups block completely the electron localization from the anchoring group, and iv) the absence of donor decreases the energy of HOMO level. BODIPY with vinylene and methyl groups were chosen for the synthesis, because the methyl groups increase the life-time of electron–hole pair. Doping with nitrogen shows that the amount of nitrogen atoms makes difference for electronic structure, yet do not distort the lattice. The electronic structure changes due to the created empty gaps states that enhance electron conductivity.

In the second part of this study, derivates of perylenemonoimide based dye molecules trisphenyl amine based anchoring groups on the NiO(100) surface and their interactions are investigated. The study with complete dye molecules on the nickel oxide surface is straightforward: the dyes' highest occupied molecular orbital is above nickel oxide's valence band maximum, thus, the spontaneous charge transfer is hard to obtain. Next it is shown that the anchoring group impacts the energy level alignment because of created dipole moment of the system that creates a shift within an electrostatic potential. Due to the shift, the highest occupied molecular orbitals of the dye mole-

cule are either above (in case of carboxylate) or below (in the cases of pyridine and 1,2-diol) valence band maximum. In the case of complete molecules, which have the carboxylate as an anchoring group, HOMOs are above the VBM.

The results and analysis of the study show the importance of the size of the molecule and the anchoring group. The smaller the dye molecule, the smaller the distances are inside the interacting system, and shorter distances to transfer the charge. In the case of complete molecules, which have the carboxylate as an anchoring group, HOMOs are above the VBM. In conclusion, the largest effect is caused by the anchoring group inside the interacting system.

Tiivistelmä

Värikkäät ja taipuisat väriaineherkistetyt aurinkokennot rakentuvat edullisista ja kierrätettävistä materiaaleista muuntaen auringonvalon energiaksi. Edellä mainituista hyvistä puolista huolimatta, nämä kennot ovat heikkoja teholtaan. Siksi tarkoituksena on tutkia väriaineherkistettyjen aurinkokennojen eri komponentteja ja niiden toimintaperiaatteita erikseen ja vuorovaikutuksessa. Tutkimus painottuu eirtyisesti varauksensiirtoreaktioihin väriaineen ja puolijohdepinnan välillä. Pääreaktio näissä kennoissa yksinkertaistettuna on seuraava: viritetty väriaine molekyyli siirtää varauksen puolijohdepinnalle, josta se jatkaa elektrodille luoden (sähkö)virran.

Tutkimuksen aikana mallinnuksessa käytettiin booridipyrrometeenin, peryleenimonoimidin ja trisfenyyliamiinin johdannaisia väriainemolekyyleinä. Nikkeli- ja titaanidioksidi olivat käytetyt puolijohteet. Mallinnetut ankkuriryhmät olivat: karboksylaatti, 1,2-dioli ja pyridiini. Yhdisteet mallinnettiin teoreettisesti eristettynä (tyhjiössä) ja vuorovaikutuksessa keskenään. Kuten mainittu, tutkimus tehtiin teoreettisesti mallintamalla B3LYP hybridifunktionaalia CRYSTAL09 ohjelman avulla. Yleisesti hybridifunktionaalia ei käytetä periodisten systeemien, esimerkiksi väriaine-puolijohde –systeemien, mallinnuksessa. Siksi näillä mallinnusmenetelmillä saadaan uutta tietoa.

Ensimmäisessä vaiheessa booridipyrrometeenin johdannaisia ja titaanidioksidi puolijohdepintaa (typpi-doppauksella) mallinnettiin erikseen. Booridipyrrometeenin tulokset osoittavat, että i) vinyleeniryhmä ei vaikuta elektronien siirtymätiloihin eikä orbitaalien sijaintiin/muotoihin, ii) fosfonaatti vetää vähiten ja karboksylaatti eniten elektroneja puoleensa, iii) metyyliryhmät poistavat kokonaan elektronilokalisaation pois ankkuriryhmästä (pidentäen elektroni-aukkoparin elinikää) ja iv) ilman donoria alimman miehitetyn molekyyliorbitaalin energia laskee. Edellä mainittujen tulosten perusteella booridipyrrometeeni vinyleeni- ja etyyliryhmillä ehdotettiin syntetisoitavaksi kokeelliselle ryhmälle. Titaanidioksidin doppaus typellä osoittaa, että typen määrällä on merkittäviä muutoksia elektronirakenteeseen, koska pinnassa olevat typpiatomit luovat tyhjiä tiloja ‘gappiin’ parantaen elektronien johtavuutta. Typpi ei kuitenkaan vaikuta pinnan geometriseen rakenteeseen.

Toisessa vaiheessa peryleenimonoimidin ja trisfenyyliamiinin johdannaisia mallinnettiin erikseen ja nikkelioksidin kanssa vuorovaikutuksessa. Tulokset peryleenimonoimidin ja nikkelioksidin vuorovaikutuksista ovat selkeitä: väriaineen korkeimmalla miehitettyllä molekyyliorbitaalilla on korkeampi energia kuin puolijohdepinnan valenssivyön maksimi, eli spontaani varauksensiirtoreaktio on epätodennäköistä. Kun trisfenyyli oli vuorovaikutuksessa nikkelioksidin kanssa eri ankkuriryhmillä, havaittiin suora riippuvuus dipolimomentin ja energiatasojen ryhmittymisen välillä. Dipolimomentin

vaikutuksesta, systeemeillä on elektrostaattinen siirtymä z-akselin suuntaan, joka joko nostaa (karboksylaattin tapauksessa) tai laskee (1,2-diolin ja pyridiinin tapauksessa) molekulaarisia energiatasoja. Koska peryleenimonoimidin johdannaisilla oli käytetty karboskylaattia ankkuriryhmänä, molekulaaristen orbitaalien energiatasot ovat valenssivyötä korkeammalla energialla.

Tutkimuksen johtopäätöksiä ovat: väriainemolekyylin rakenteella (ankkuriryhmä) ja koolla on väliä puhuttaessa, miten niitä käytetään aurinkokennoissa. Lyhyet välimatkat varauksen siirrolle parantavat mahdollisuuksia spontaaniin reaktioon. Kuitenkin ankkuriryhmällä olisi suurin merkitys elektronikofiguraatioon.

Résumé

Des cellules solaires à pigments photosensible sont composes des matériaux pas cher et recyclable. Ces matériaux de couleur et flexibilité convertissent la lumière de soleil à énergie. Toutefois, elles sont inefficaces parce que courant photonique bas. L'objet de thés est de comprendre des propriétés électronique ???? pour les cellules solaire à pigments photosensible plus efficace. La réaction plus importante dans le système est des transferts de charge entre les pigments photosensible et le semi-conducteur. La réaction simple suit le chemin: le molécule excité donne l'électron pour le semi-conducteur, ou l'électron est transféré d'électrode et créé courant électrique.

Les pièces recherchés sont des dérivés bore-dipyrométhene, perylene monoimide et tris phényle amine. Nickel oxydé et titane dioxyde sont des modes pour surfaces semi-conductrices utilisées. Finalement, on utilise carboxylate, 1,2-diol et pyridine comme des groupes ancrer. Ils sont recherché séparé et ensemble pour d'info d'interaction électronique. On utilise B3LYP fonctionnel hybride dans CRYSTAL09. Les fonctionnels hybride ne sont pas utilisé partout à étudier des systèmes périodiques. Alors, les résultes qui sont présentés dans ce-ci thés offrissent des idées nouvelles.

Au début, les dérivés bore-dipyrométhene et titane dioxyde (avec le impureté de azote) sont modelé séparés. Les résultes de bore-dipyrométhene proposent que i) la groupe vinylene ni change pas des transitions d'électron ni des localisations d'électron, ii) l'ancrer phosphonate attire le moins et l'ancrer carboxylate le plus de localisation d'électron, iii) la groupe méthyle bloque le localisation d'électron pour la groupe d'ancrer, alors, ça s'accroit de temps de 'electron-hole pair', et finalement iv) l'absence de donneur diminue l'énergie de highest occupied molecular orbital. Donc, on a choisi à porposer un dérive bore-dipyrométhene avec les groupes vinylene et méthyl. Les résults de titane dioxyde présent que la quantite d'azote fait la grande différence dans la structure électronique, mais il y n'a pas de changement dans la structure du réseau. Les changements dans la structure électronique paraissent à 'band gap' comme des états vides d'azote qui s'améliorent la conductivité des électrons.

Ensuite, les dérivés perylene monoimide et tris phényle amine (avec trois ancrers differents) sont éxaminé sur NiO(100) surface. Les résulte des dérivés perylene monoimide sont limpides: HOMO de molécule pigment a plus haute energie comme VBM de surface, NiO. Alors, les réactions des transferts de charge spontanés sont improbables. Les résulte de l'ancres différentes montrent que le moment dipôle a en effet grande pour de niveau d'énergie. Le changer de niveau de vacuum soit relève (carboxylate) soit réduit (1,2-diol, pyridine) la niveau de HOMO.

Enfin, les résulte et les analyses indiquant que le taille et la groupe d’ancrer sont très important. Si le molecule est petite, le distance pour des élecrtons est court et c’est plus facile pour l’électron transfére entre le molecule et semi-conducteur. Aussi, la groupe d’ancrer présente que il a l’effet pour de niveau d’energie. Alors, on peut dit que l’effet le plus grande est causé par la groupe ancrer.

Preface

I would like to thank my funders. I acknowledge Terttu Hukka for providing funding from 2014 to 2015. In addition, the grants from Suomen kemian päivien säätiö (2014), the Walter Ahlström Foundation (2014–2015), and Emil Aaltosen säätiö (2017 and 2018) are greatly appreciated. In addition, I am grateful to the Laboratory of Chemistry and Bioengineering for providing workspace. Lastly, thank you to Université de Mons for providing funding and working place in 2016 and 2017. The study's computational resources were provided by both the CSC - IT center for Science Ltd. that is administered by the Finnish Ministry of Education and Université de Mons, all of which is gratefully appreciated.

I am grateful to Tapio Rantala for his supervision during this thesis. He provided valuable insight on the semiconductor physics, and I learned many new concepts and perspectives from him. I also want to thank Terttu Hukka for her comments, questions, and persuasive methods of supervision. She showed that I have much to learn and taught me to never let my guard down. She also negotiated my international exchange position in Mons, which I am very grateful for. Thank you as well to David Beljonne and Jérôme Cornil for pushing me further in my critical thinking and for showing me how to take even the smallest of details into account; in the quantum world, nothing can be overlooked. Not to mention that their wild ideas showed me that it is possible to take research in many directions but that careful thinking is always wise before taking the first step. I am also grateful to David for providing me with the opportunity to study abroad. In addition, I would like to show my gratitude to Mika Niskanen, who taught me how to use CRYSTAL. He provided ideas and tips on how to utilize this application to its full potential and gave me the tools to pass this knowledge on to others. Lastly, many thanks to Lauri Judin for proofreading.

Thank you for all the dear people in my life! Thanks to my mom, my dad, and my brother, Niilo, for tolerating me. Thank you to my best friends, Miina and Sinna, for always having a shovel ready. I am grateful to Tomi for constantly reminding me that both the roots and the head are important to mental health. Thank you as well to Terhi, Ankka, Anni Hoo, and Jarski for being wonderful people who I could always hang out and share good food and drinks with. In addition, it is great to have people who will always have a sofa ready for me; I trust that this sofa will still be free for me in the future. Thank you to Saara and Joni, Meira and Mikko, and Tiitu. I will happily remember tea breaks with Katariina and Laurie on the weekends. In addition, thank you to my local friends, to my Italian family (Francesca, Andrea "the Godfather," "Jaakko", Gabriele, Claudia, and Mattia), and of course, to Sandra and Lian. Imane, it has been more than a pleasure to work with you. All the best in your research! Lastly, I would like to thank Claudio for his teachings, patience, and kindness.

Mons 23.8.2017 *Outi Vilhelmiina Kontkanen*

Contents

List of Symbols and Abbreviations

1G	First generation (solar cells)
2G	Second generation (solar cells)
3G	Third generation (solar cells)
B3LYP	Becke-Lee-Yang-Parr hybrid functional
BF	Bloch functions
BODIPY	Derivatives of boron-dipyrromethene
C60	Fullerene
CARB	Carboxylate
CBM	Conduction Band Minimum
Co(II/III)	Cobolt electrolyte
CT	Charge transfer
$CuAlO_2$	Copperaluminium oxide, a delafossite
CuO	Copper(II) oxide
D-A	Donor-Acceptor
DFT	Density Functional Theory
DIOL	1,2-Diol
DOS	Density of states
EA	Electron affinity
E_F	Fermi level (also called Fermi energy)
$[Fe(acac)_3^{0/1-}]$	Tris(acetylacetonato) iron(III/II)
HOMO	Highest Occupied Molecular Orbital

I^-/I_3^-	Iodide/triiodide
IP	Ionisation potential
LCAO	Linear Combination of Atomic Orbitals
LUMO	Lowest Unoccupied Molecular Orbital
NDI	Naphthalene diimide
NiO	Nickel oxide surface
PAW	Projector augmented wave
PBC	Periodic Boundary Conditions
PHOS	Phosphoric acid
Ph	Phenyl
PMI	Perylene monoimide
PYR	Pyridine
SC	Semiconductor
TDDFT	Time-Dependent Density Functional Theory
TiO_2	Titanium dioxide
TPA	Trisphenyl amine
VBM	Valence Band Maximum
WF	Work function
ZnO	Zinc oxide

$\boldsymbol{A}_{\mu}$	Coordinates of the nucleus within PBC
c_i	Normalization coefficients
∇^2	Laplacian operator
∂/∂x	Partial derivative with respect to x
E	Energy
e	Charge of the electron
e^-	Electron (particle)
Ψ	Eigenfunction in form of N-particle wave function
ϕ	Delocalized basis functions
φ	Local atomic orbitals, basis functions
ψ	linear combination of atomic orbitals
$\boldsymbol{g}$	Lattice vector
H	Hamiltonian operator
h^+	Hole (particle)
$\hbar$	Plank's constant divided by 2π
i	Imaginary unit
$\boldsymbol{k}$	Wave vector
m_e	Mass of an electron
m_k	Mass of the nucleus k
m^*	Effective mass (of electron)
$\boldsymbol{r}$	Coordinate of the particles
$\boldsymbol{r_{ab}}$	Distance between particles a and b

Author’s Contribution

The results presented in this monograph were partially published earlier [1] and will be published later (in a manuscript). In addition, this thesis consists of an unpublished analysis of potential dye molecules and of the effect that nitrogen doping has on a titanium dioxide surface. In all cases, the author performed the calculations, participated in designing the calculations and models, wrote up the results, and participated in the interpretation of those results.

1 Introduction

Energy consumption is increasing every year; hence, lasting solutions are needed to ensure that energy is produced in an efficient way. Fossil fuels cannot be relied upon because they are expensive [2-4] and will be fully consumed by 2070. Therefore, humans have to find a way to produce energy that is more efficient and less expensive than fossil fuels such as coal. One solution is to use renewable energy sources, as there are no practical limits to the extent of solar, water, wind, or thermal energy. However, renewable energy sources do have limitations. First, it is not easy to change from using nonrenewable energy sources to using renewable ones. For example, many industries and technologies rely on energy produced by fossil fuels such as coal. [2, 5] Second, renewable energy sources are expensive to build due to, for example, the size of windmills and the costly materials used in solar cells. Third, renewable energy sources demand certain conditions: i) solar cells cannot collect photons during the night or when the weather is cloudy, ii) windmills require strong winds, and iii) water power plants are limited to specific areas. Lastly, despite advances, renewable sources are still inefficient. As an example, the highest efficiencies found solar cells are still just 15–20%. [6]

Renewable energy sources need development; fortunately, they are improving quickly. Solar energy is the fastest-growing renewable energy source, with a 48% year-over-year increase in total energy consumption in 2016. [2] In addition to solar energy's fast development, it is a plentiful source. The amount of radiation emitted from sunlight is gigantic: 3×10^{24} J per year. In practice, covering just 0.1% of the Earth's surface with solar cells (at an efficiency of 10%) would satisfy humans' present needs for energy consumption. [7] For this reason, solar energy is especially appealing. Dye-sensitized solar cells (DSSCs) are particularly promising, as they are meant to provide high efficiency with low-cost materials. In addition, they differ from ordinary solar cells, which

have a semiconductor (SC) component, in that they separate the functions of light absorption and charge transfer (CT). [8] In addition, DSSCs have a high predicted efficiency and use more recyclable materials than conventional silicon solar cells.

1.1 History of the photovoltaic effect

This section covers the main points related to DSSCs and addresses their importance. The photovoltaic effect was first outlined approximately 200 years ago, in 1839, when Becquerel discovered that light created an electric current in a solvent by using platinum electrodes in metal halide salt solution. [9] The second step was taken in 1887, when James Moser introduced a photoelectrochemical cell that used dye-sensitized molecules; this technology had applications in photography. Moser used erythrosine on silver halide, [10] as Vogel had done four years earlier in the laboratory. [11] After Moser and Vogel, however, the discoveries in photovoltaics have been slow. It took almost 100 years before Chapin and coworkers built the first functional solar cell in 1954. [12] This was a silicon solar cell that attained 6% efficiency. [12] Since that time, silicon solar cells have ruled the industry. However, other possibilities have been studied; the notable challengers include DSSCs.

In 1988, Grätzel and coworkers became the first to notice that a current can be created inside a solution of dye molecules; they started to study the topic in a more detailed manner, similar to what Becquerel used. [13] In 1991, Grätzel published the discovery of the first silicon-free DSSC [8]—what is now known as a Grätzel cell. At present, the research focusing on DSSCs is growing steadily. As a matter of fact, Google Scholar shows that the number of publications with the keyword “DSSC” has steadily increased from 818 in 2007 to 4540 in 2016.

1.2 Solar energy and solar cells

Photovoltaics are a way to directly convert sunlight into energy. Because of the fast development of solar research, there are many possible ways to construct solar cells. At present, the most commonly used solar cells are made of silicon; these are known as first-generation (1G) and second-generation (2G) solar cells. [14] The 1G solar cells

are constructed of (poly)crystalline silicon cells, n- and p-type substrates, and an oxide layer. The 2G type has lower energy costs than the 1G type due to the 2G type's thin-film technology, which uses less silicon than the style used for 1G cells. Another way to lower costs in 2G solar cells is to use alternative materials such as copper indium diselenide. [14, 15]

At present, silicon solar cells have the highest power-conversion efficiencies of all cells. They can reach 25% [16] and 20.4% [17] power-conversion efficiency for single- and multiple-crystalline silicon, respectively. Still, silicon solar cells are rigid, difficult to re-cycle, expensive, and they do not collect sunlight from a wide spectrum of light. [14, 18] Fortunately, new alternatives to these 1G and 2G solar cells have been investigated to lower costs and to reach higher efficiencies.

New, third-generation (3G) solar cells, have been created to meet the challenge of high-efficiency, low-cost solar cells. So far, the most promising cells are tandem DSSCs, perovskite, polymer, and organic solar cells. [14] In addition to the lack of silicon, these cells differ from the previous generations of solar cells in that they use thin-film technology, are more recyclable, have greener materials, and take in a wider spectrum of sunlight. [18, 19] However, due to the choice of components, 3G solar cells have lower photoinduced currents than do 1G and 2G solar cells; in other words, they are less efficient. However, tandem DSSC and perovskite cells are notable alternatives for future use, as the former has a theoretical efficiency of 40% [20, 21] and the latter has already been found to reach ~20% efficiency. [22-25] At the same time, DSSCs lack efficiency, and perovskites lack thermal stability in processing. [26]

1.3 Dye-sensitized solar cells

As stated before, DSSCs are a good alternative method of harnessing solar energy due to their cheap materials and efficiency. This technology has been gaining attention because of the studies that Grätzel has conducted since 1991. [8] So far, the most well-known and widely used DSSC is the one called the Grätzel cell or the n-type DSSC (n-DSSC). This cell reaches 13% efficiency [27] and thus already challenges 1G and 2G solar cells, which can reach at most ~20%. The second, less known DSSC variety is p-type DSSC (p-DSSC), which has thus far reached only 2.51% efficiency, [27] making it less desirable to use. The third type is a tandem or pn-type DSSC (pn-

DSSC), which is constructed from both n- and p-type cells. The created voltage in pn-DSSC is higher than in the other types, and the collected spectrum of sunlight is wider.

Unfortunately, pn-DSSCs' theoretical efficiency (40%) [21] is still far away, as the highest recorded efficiency for a pn-DSSC in the laboratory is 4.1%. This was achieved with both trisphenylamine derivative (TPA) adsorbed onto titanium dioxide (TiO_2) and diketopyrrolopyrrole adsorbed onto nickel oxide (NiO) surfaces. [28-30] In the case of pn-DSSC, its low efficiency is determined by the weaker of the two components, which is currently the p-DSSC. In light of this information on pn-DSSCs, p-DSSC is an interesting system, [28] and there is growing interest in finding ways to improve it, including within this thesis.

1.4 Modeling of dye-sensitized solar cells

Computational techniques offer the means to determine, at an atomistic level, materials' intrinsic properties. In general, these techniques are fast, systematic, and safe ways to screen promising materials for any system, including DSSCs. In addition, computational methods allow for the collection of information about the CT reaction; this crucial information about DSSCs is hard to obtain through experiments. For this purpose, density functional theory (DFT) is the most commonly used method due to its mathematical simplicity and accuracy; however, it is demanding for large (over 1000-atom) systems. [31] By the same token, time-dependent DFT (TDDFT) can be used to study the systems' excitations and transition energies. [31, 32]

Modeling is used both to study known structures and to screen potential molecules or surfaces for synthesis. For both known dye molecules and SC surfaces, studies have focused on properties such as electron structure, absorption, hole and/or electron injection, orbital localization, and stabilization in liquid (electrolytes). [32-34] In addition, the screening of dye molecules has led to the identification of major differences between these possibilities (in terms of anchoring groups, donors, and acceptors), thus explaining the behavior inside the interacting system. [1, 34, 35] Additionally, modeling has been used to predict symmetries and the surfaces' hole- or electron-carrier properties. [34, 35]

The chemisorbed anchoring groups have also been modeled on SCs to generate better understanding of CT reactions. In particular, carboxylate (CARB) has been widely tested with complete molecules alongside new alternatives. [34, 35] Other modeled an-

chors include silicon [35] and pyridine (PYR). [36] The results for silicon show that the energy levels are below the valence-band maximum (VBM) and indicate that silicon can attach strongly to the NiO surface (*i.e.*, in p-DSSC, it is an alternative for the more widely used CARB). Likewise, PYR anchors show a strong adsorption on the TiO_2 surface and have an acceptor character. [36]

Finally, the interacting systems have been studied to improve understanding of i) how the different components impact each other (based on intramolecular CT), [31] ii) how the dye molecule binds to the surface (based on the molecule's orientation on the surface and the strength of the binding), [31] and iii) the relationship between the structure and the performance (based on impact of the neighboring dyes). [37] In conclusion, the isolated systems are screened using multiple options, and new compounds are designed for DSSCs; the modeling of the interacting system explains the effects of the adsorption (in terms of CT, energy-level alignment, and performance).

1.5 Aims and objectives

The aim of this study is to model the components of p-DSSCs so as to improve understanding of these cells' electron structures and interactions. So far, p-DSSCs' low current is a problem; this is suspected to be due to the materials used. In addition, the effects of the CT reactions inside the system are not well-known. This study focuses on understanding the differences, connections, and interactions between the isolated and interacting systems. Because the selected models are typical for p-DSSC compounds, the calculations are expected to reveal why certain compounds interact better than others. By the same token, the CT reactions between the dye molecule and the SC surface are investigated. Moreover, the complete interacting systems of p-DSSC have not been as widely studied as those of n-DSSC. This study's results can be used to suggest new materials for DSSCs, including dye molecules, functional groups, and modified surfaces. The goal is to suggest tools to build an efficient pn-DSSC that is based on the information presented in this thesis in future.

This thesis is constructed as follows. In the second chapter, the background of the field is presented; within that chapter, the CT reactions and the typical parts of the system (dye molecule, SC surface, and electrolyte) are described. The third chapter presents the typical DSSC compound in more detail and addresses the models that are used. In the fourth chapter, the quantum mechanical background behind the calculations is addressed, starting from Schrödinger's equation and ending with Bloch functions (BFs) and DFT. In the fifth chapter, the results are discussed, and new insights are provided.

2 Background

In this chapter, various DSSC and CT reactions are discussed, starting with the three main components (the dye molecule, the SC, and the electrolyte). The most commonly used compounds are addressed, and insight is provided into the current state of development. The second and last section addresses the background of the field by explaining the CT reactions that occur for all combinations of dye molecule, SC, and electrolyte, with a focus on the desired properties of these reactions. In addition, the possible weaknesses of CT are investigated.

2.1 Construction of the dye-sensitized solar cells

Compared to 1G and 2G silicon solar cells, DSSCs have several advantages. The most visible differences are that DSSCs are more aesthetically please due to their many vivid colors and flexible construction (Figure 2.1), [14, 26] which allows DSSCs to be attached to different-shaped surfaces or even used as windows that turn radiation from sunlight into electric current. [18] DSSCs also utilize materials that are more readily recyclable and that cost less than most of the materials used in inorganic (1G and 2G) silicon solar cells. [8] Additionally, during preparation, DSSCs are more thermally stable than other 3G solar cells such as those made of perovskite [26], and pn-DSSCs have a higher expected efficiency than do organic solar cells.

There are three main parts of a DSSC: i) a layer of dye molecules that is grafted on ii) an inorganic SC surface that is, in turn, embedded in iii) an electrolyte. Fortunately, these materials are widely studied, both separately [27, 29, 34, 35, 38-43] and in inter-

acting systems [1, 28, 35, 44-47]—both theoretically and experimentally. These three parts have to interact to create a photovoltaic current. Below, the three components are examined separately.

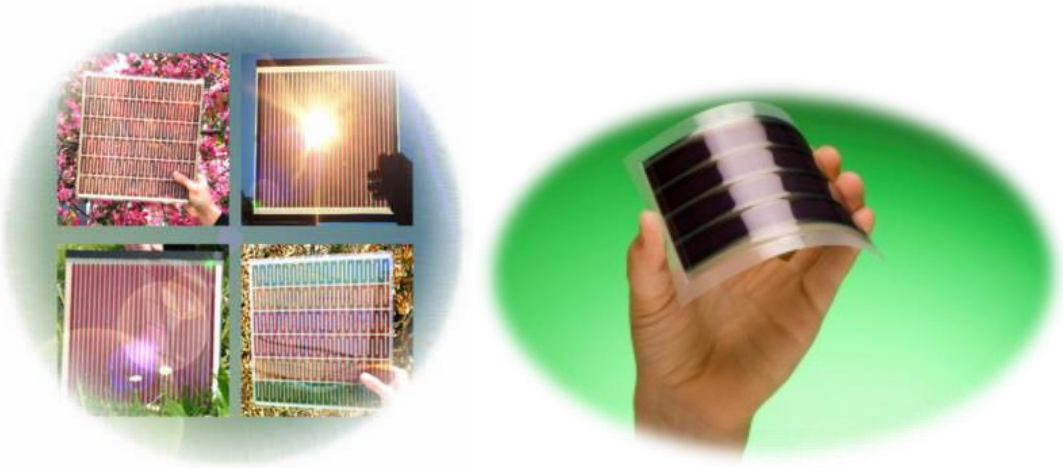

FIGURE 2.1 A visual example of how a DSSC can be colorful (left) and flexible [48] (right).

2.1.1 Dye molecules

There are two types of dye molecules: mono- and multichromophoric. Porphyrins, coumarins, and ketopyrrolopyrrole [38, 43, 47, 49-51] are examples of monochromophoric dye molecules. Multichromophoric dye molecules are constructed from two moieties [6, 28, 37, 38, 52, 53] such as TPA and perylene monoimide (PMI) (Figure 2.2) [1, 53-55] and are also called donor–acceptor (D–A) dyes because the two moieties (which can be separated) have an electron-based interaction while retaining independent character within each separate moiety inside the dye molecule. In this case, one part (the donor) gives the electron to the other part of the molecule (the acceptor). Additionally, D–A dyes are easy to synthetize and can be tuned by changing between various electron-donating and -accepting moieties. [56] Correspondingly, their properties (energy level and the electron-transfer direction) are easy to control through the group's functionalities by, for example, removing or adding parts; this is shown later in this thesis (section 5.2) and in other studies. [57, 58] Thus, compared to monochromophoric dyes, D–A dyes are preferable because their electron–hole pair is formed in various moieties and because their electron transitions are easier to follow. Not only the route but also the CT time is controlled in D–A dye molecules, which have a long-

lived charge-separation state that lengthens the lifetime of the electron–hole pair. [6] As a result, the SC has more time to interact with the dye molecule. For these reasons, D–A dye molecules are used in this study.

At present, PMI is the most used material for p-DSSCs, but other molecules have been studied. Recently, diketopyrrolopyrrole has been gaining attention due to its high photosensitivity, easy synthesis, long-lived charge-separation states, ability to drive electron transition, and high electron-transfer efficiency. [28, 38] The results have been promising, and this material has already been tested inside a pn-DSSC, helping to obtain the highest recorded efficiency (4.10%) for such a cell. [28]

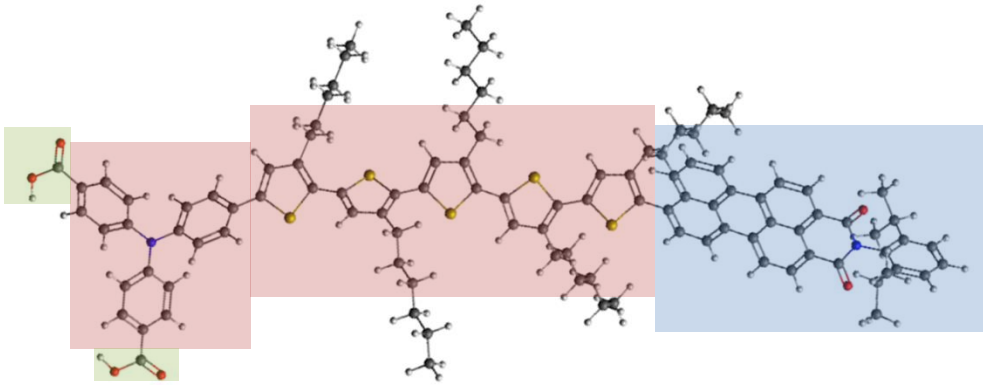

FIGURE 2.2 A commonly used dye molecule, TPA–PMI, whose derivatives are used in p-DSSCs. The donor is in red, the acceptor is in blue, and the anchoring group is in green.

Regardless, the anchoring group links the dye molecule and the SC. The most popular anchoring group is CARB, which is used in both n- and p-DSSCs. Alternatives have been studied, however. The tested anchoring groups have thus far shown similar performance, [59] but despite these similarities, the properties—such as the binding of the anchoring group—determine whether the charge moves between the two systems. For example, bidentating carboxylate have been shown to provide almost double the photovoltaic current as a monodentate binding model with the same molecular structure. [60] Additionally, the surface that the anchoring group binds onto also matters, as CARB binds stronger onto NiO than onto TiO_2. [61] Anne and coworkers suspected that the latter was due to the dye molecule's redox potential. [61] To conclude the discussion of dye molecules, it is important to investigate a variety of anchoring groups and to consider new possibilities for the dye molecule (on various surfaces). Therefore, it is intriguing to study a dye molecule's properties when it is in contact with SC surface.

2.1.2 Semiconductors

The second component of a DSSC is the SC surface. The SC is a solid that is neither metal nor insulator but that has conductivity due to an excess or shortfall of electrons, which can be caused by photon excitation, a magnetic field, an electric field, doping, temperature change, or other particles. An excess or shortfall of electrons can be tuned (using the methods mentioned before) to affect the electron structure—including the VBM, the conduction-band minimum (CBM), and the band gap—which makes SCs interesting materials that can be used in many applications, *e.g.*, in solar cells and as transistors in electronic devices. [62] In DSSCs, the SCs accept either the electron or the hole, based on the SCs' character and on the attached dye molecule. Depending on the system, the position of the CBM and/or VBM are interesting, particularly in comparison to the dye molecule's highest occupied molecular orbital (HOMO) and the lowest unoccupied molecular orbital (LUMO) levels. The energy-level alignment is addressed later in this chapter.

Certain variables are important for SC surfaces: ionization potential (IP), electron affinity (EA), work function (WF), and Fermi level (E_F). IP is the energy needed to transfer an electron from a compound to the vacuum; in other words, it is the minimum energy needed to create a cationic system. In contrast, EA is the energy released when adding an electron to the system; in other words, it refers to the energy needed to create an anionic system. E_F refers to the level at which the Fermi–Dirac distribution of electrons has the value of 0.5—approximately the average of the IP and EA values. Finally, WF is the energy difference between the E_F and the vacuum. [62] These numbers link the theoretical and experimental work and make them comparable.

The most commonly used SCs for DSSCs are zinc oxide (ZnO) and TiO_2 in n-DSSC [28] and NiO in p-DSSC. [1] These SC surfaces can be used because they are pristine or because they can be modified via doping or coatings of other SC layers. Additional layers and doping are used to specify the SC system's energy levels. Because this thesis focuses on p-DSSC, it uses the most common p-type SC surface, NiO. Even though NiO is the most used type, it is not an optimal choice because of its shallow VBM, [63] low hole mobility, [63] and strong color. [55] In particular, due to NiO's strong color, it absorbs photons in competition with the chemisorbed dye molecule, decreasing the device's efficiency. Due to these deficiencies, both alternatives to NiO and new ways to improve the NiO surface have been studied. Some notable suggestions for the replacements are delafossites such as copper(I) aluminum oxide ($CuAlO_2$) [64, 65] and

copper(II) oxide (CuO) [66]. Thus far, however, these materials have lower photocurrents than NiO, so it continues to be used.

2.1.3 Electrolytes

The electrolyte is the final important part of a DSSC. It regenerates the dye after a charge injection and carries the current to the corresponding electrode. The electrolyte consists of a redox couple (or redox shuttle or redox mediator), a solvent, and additives.

First, the redox mediator is introduced. The most commonly used redox mediator is iodine/triiodine (I^-/I_3^-). [6] However, this material is not ideal for DSSCs because it is corrosive and volatile, absorbs photons, has a low generated current, and causes inherent energy loss. [6] As a result, alternatives to I^-/I_3^- have been considered. A few other possibilities are worth mentioning; cobalt (Co) (II/III), thiol/dithiol, and tris(acetylacetonato) iron(III/II) ($[Fe(acac)_3]^{0/1-}$), which have been successfully used to gain efficiencies of 1.30%, 6.4%, and 2.51%, respectively. [67-70] However, these mediators have been used with p-DSSC but with not with pn-DSSC. Therefore, there is no data on how they will perform with n-DSSC or pn-DSSC. In conclusion, I^-/I_3^- is used because it is the only redox mediator that is known to work with both types.

The second and least studied component of the electrolyte is the solvent, which plays an important role, as it provides the medium for the system. Hence, the solvent affects all the components that are dissolved into the system and should not be overlooked. A few examples of solvents are acetonitrile, esters, lactones, alcohols, and tetrahydrofuran. A good solvent has low toxicity, low cost, low light absorbance in the near infrared and visible regions, high salt solubility (for the mediator and the additives), and both a low melting point and a high boiling point to avoid freezing and evaporation during outside use. [6]

The last component, the electrolyte additives, are compounds, *e.g.*, triazole [71] that can be used to improve performance; these have been mainly studied in n-DSSCs, and only a few studies have been found for p-DSSCs. [6] Still, the absence of additives in a p-DSSC is not an issue as long as any such additives enhance the performance of the n-DSSC without harming the p-type reactions.

2.2 Charge-transfer reactions

DSSCs are typical CT systems in which photoinduced excitation causes a current. The main difference in terms of CT between DSSCs and other SC-based solar cells is that the excitation of the electron in DSSCs is different from the CT that creates the electric current inside the SC surface. [8] The main idea is that the charge is transferred inside the solar cell between moieties, such as from donor to acceptor (intramolecular CT) or from dye to surface or electrolyte (intermolecular CT). The confirmed main reactions are as follows:

$$nSC|Dye + hv \rightarrow nSC|Dye*, \tag{2.1}$$

$$nSC|Dye* \rightarrow nSC|Dye^{+} + e^{-}(nSC), \tag{2.2}$$

$$nSC|Dye^{+} + e^{-}(El.) \rightarrow nSC|Dye, \tag{2.3}$$

$$pSC|Dye + hv \rightarrow pSC|Dye*, \tag{2.4}$$

$$pSC|Dye* \rightarrow pSC|Dye^{-} + h^{+}(pSC), \tag{2.5}$$

$$pSC|Dye^{-} + h^{+}(El.) \rightarrow pSC|Dye, \tag{2.6}$$

where *Dye* is the molecule (on the surface); *Dye** is the excited molecule; *nSC* and *pSC* are the n-type and p-type SC, respectively; h^{+} is hole; e^{-} is an electron; *El.* is the electrolyte; and *hv* is a photon. Green color (Equations 2.1–2.3) indicates that the CT reactions take place inside the n-DSSC, and red color (Equations 2.4–2.6) indicates that the CT reactions occur inside the p-DSSC. Consequently, all presented reactions (Equations 2.1–2.6) happen inside a pn-DSSC. [20, 32, 44, 72] The same CT reactions are visualized in the Figures 2.3 and 2.4. In Figure 2.3, the CT inside the D–A dye is illustrated for the p-type molecule (*i.e.*, the electron is transported away from the surface). Meanwhile, Figure 2.4 shows the CT reactions for the three components (dye molecule, SC, and electrolyte). The colors are the same as those in Equations 2.1–2.6: Green part is for the n-type, and red part is for the p-type.

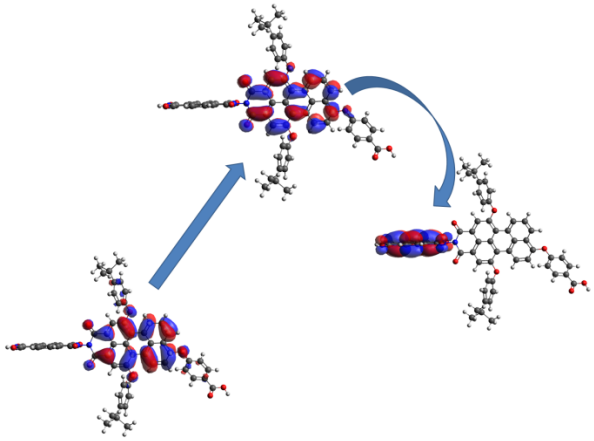

FIGURE 2.3 Charge-transfer reactions inside the donor–acceptor dye molecule. The electron is excited inside the donor and then relaxed so that it moves toward the acceptor.

One part of understanding this system's CT reactions is examining the intramolecular CT that takes place inside the D–A dye molecule. The main idea is illustrated in Figure 2.3. In the first step, the excitation takes place inside the donor unit, so the electron stays within the same moiety. In most cases, this electron transition is from HOMO to LUMO+N (N=1,2,3,…). In the next step, the electron relaxes and is transferred from donor to acceptor, which is in a state within the first transition (*e.g.*, LUMO). However, it is possible for the strongest transition to be from lower energy levels than HOMO, *e.g.*, from HOMO-1. This is not a problem as long as the path is inside the donor and the relaxation is from donor to acceptor, which creates an electron–hole pair.

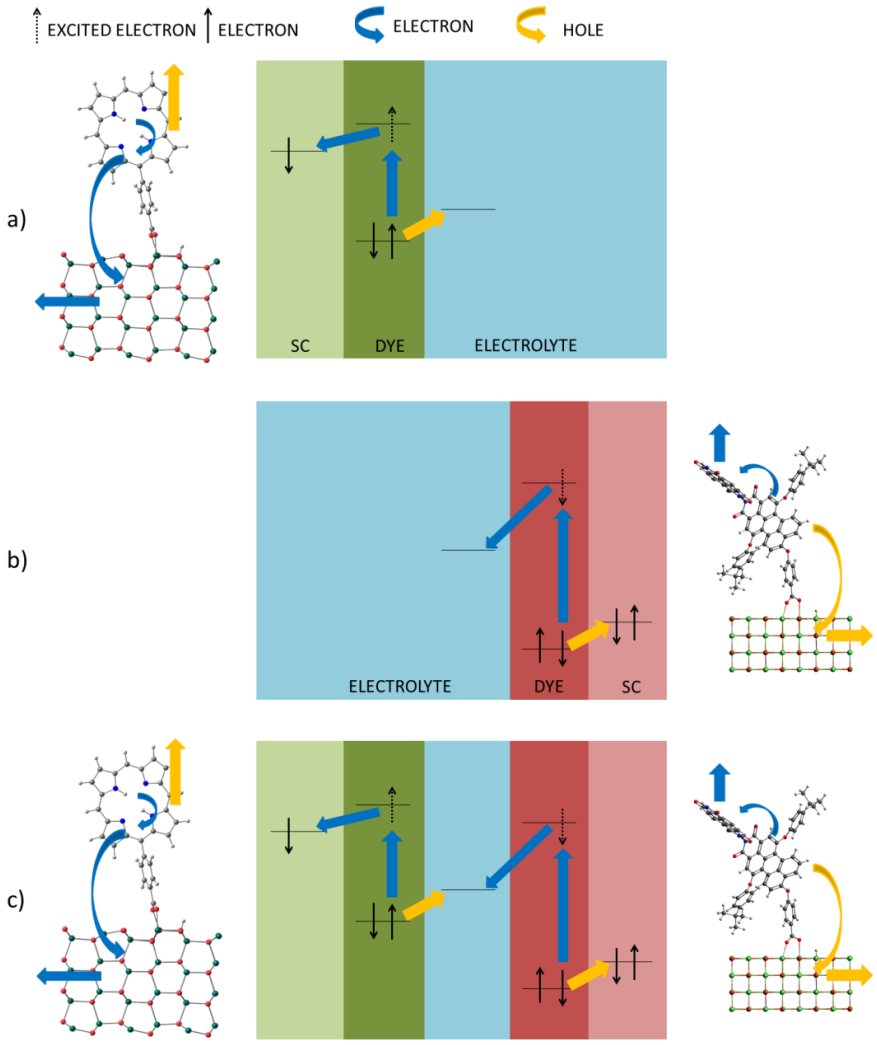

FIGURE 2.4 The charge-transfer reactions presented in Equations 2.1–2.6 are visualized as follows: a) n-DSSC (green), b) p-DSSC (red), and c) pn-DSSC. A single molecule is presented as a model for n-DSSC, and a D–A dye molecule is used as a model for p-DSSC.

Figure 2.4a shows the reaction for the n-type DSSC. This reaction starts when the radiation from sunlight (photon) excites the electron inside (the donor of) the dye molecule, according to Equation 2.1. It is followed by the relaxation of the excited electron to its lower states (from donor to acceptor) and to the anchoring group that is closer to the surface. An electron–hole pair is then created. In the ideal case, the electron is (partially) localized on the anchoring group, and the hole is moved farther from the surface. For a D–A dye molecule, this means that the charge distribution is D^{+}–A^{-}. The anchoring group can be part of the acceptor moiety. Now that the excitation and possible elec-

tron transition are finished, the CT (which creates the current) begins. The n-type SC surface accepts the electron from the dye molecule (through the anchor) and transports it to the anode (Equation 2.2). In the final step, the electron from the electrolyte is transferred to the cationic dye molecule (Equation 2.3); in other words, the electrolyte reduces the dye molecule back to its ground state so that the cycle can start again.

The second CT reaction is for the p-DSSC (Figure 2.4b). The electron transitions are also illustrated for a p-type D–A dye molecule (in Figure 2.3). The reaction begins according to Equation 2.4 and is similar to the previous case (Equation 2.1); the sunlight excites the electron inside (the donor of) the dye molecule. In the following step, the electron relaxes to a lower energy state (from donor to acceptor), and an electron–hole pair is created again. This relaxation is different from previous cases because the electron is transferred away from the surface and the anchoring group to the acceptor moiety. After the electron transitions inside the dye molecule, the CT reaction takes place, and the hole, which is located close to the surface and (partially) on the anchoring group, is transferred to the SC surface (according to Equation 2.5). Finally, as in the previous case, the electrolyte reduced the dye back to its ground state (Equation 2.6) so the reaction can begin again.

The final case relates to the reactions inside pn-DSSC (Figure 2.4c). Because this cell type is a combination of p- and n-DSSC, all the reactions in Equations 2.1–2.6 happen simultaneously. The reactions start with the excitation of the dye molecules and are followed by the transition of the charge (the electron for the n-DSSC and the hole for the p-DSSC) to the SC surfaces. In the final step, the electrolyte reduces the dye molecules by donating the electron (n-type) and accepting the excited electron (p-type).

Nevertheless, CTs are easily interrupted inside DSSCs. For example, when a charge is transferred to the SC surface (Equations 2.2 and 2.5), the electrolyte can interrupt the CT inside the SC. This becomes a real issue if the charge stays close to the surface instead of moving inside the SC. The electrolyte accepts the charge from the surface, which reduces the surface to its ground state. This is a problem in p-DSSC, especially because the positive hole attracts the negatively charged electrolyte. It is also possible for the excited electron inside the dye molecule (Equations 2.2 and 2.6) to not move either toward the surface (n-DSSC) or away from it (p-DSSC), as the electron can be relaxed to the wrong dye-molecule moiety. In other words, the electron stays inside the donor instead of being transferred to the acceptor. [6] The last possible interruption involves the CT reaction being reduced straight back to its ground state, preventing the current. [6] These issues explain why CT modeling is crucial for a DSSC.

One way to minimize distributions is to predict the energy-level alignment of the entire system's spontaneous CT reactions. [73, 74] Figure 2.5 shows the scheme for the ideal case inside a pn-DSSC. Although the system in Figure 2.4 shows the energy levels for a pn-DSSC, the same principles can be applied for the n- and p-DSSCs, as presented earlier with regard to CT reactions. Therefore, Figure 2.5 is a step-by-step explanation of the separate systems, n- and p-DSSC, and the combined system, pn-DSSC.

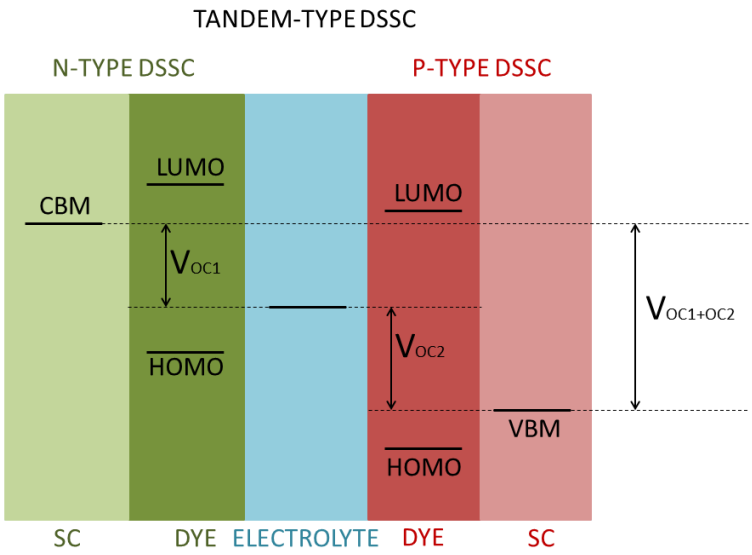

FIGURE 2.5 The open-voltage circuit in a pn-DSSC and the energy levels that affect it. Green and red parts represent the energy levels from the n-DSSC and the p-DSSC, respectively.

Figure 2.5 shows that, inside a n-DSSC (green), the CBM of the SC has to be lower than the LUMO of the dye molecule to ensure that the excited electron transfers to the SC. Because the electrolyte reduces the dye molecule by donating an electron, its corresponding energy level is higher than that of the dye molecule's HOMO. Accordingly, the difference in energy creates voltage:

$$\left(\left(E_{nDye(L+N)}\right) - \left(E_{nDye(H-N)}\right)\right) + \left(\left(E_{nSC(CBM)}\right) - \left(E_{Dye(L+N)}\right)\right) + \left(\left(E_{nDye(H-N)}\right) - \left(E_{el.}\right)\right)$$

$$= E_{nSC(CBM)} - E_{el.} \qquad (2.7)$$

$$= V_{OC1} \ ,$$

where E_X is the corresponding energy level for X = Dye(HOMO-N), Dye(LUMO+N), nSC(CBM), pSC(VBM), and the electrolyte, for N = 0, 1, 2,... . nSC refers to n-type SC surface and pSC similarly to p-type SC surface. As Equation 2.7 illustrates, the voltage is the sum of all the CT reaction energies within the system. The first term is the electron transition (Equation 2.1), the second term is the electron transportation between the dye and SC (Equation 2.2), and the third term is the CT between the dye and the electrolyte (Equation 2.3). Simplifying Equation 2.7 shows that the difference between the CBM and the electrolyte's energy level is the driving force that creates a photovoltaic voltaic current in the n-DSSC case, V_{OC1}.

Another CT takes a place simultaneously on the other side of the pn-DSSC (the red in Figure 2.5). Now, the reaction is inversed, so the VBM has to be higher in energy than the dye molecule's HOMO to enable the spontaneous hole injection from the SC to the excited dye molecule. In a similar manner, the dye molecule's LUMO has to be above the electrolyte's energy level so that it can reduce the dye molecule to its ground state. The created current, V_{OC2}, has the value

$$\begin{aligned} &\left(\left(E_{pDye(L+N)}\right) - \left(E_{pDye(H-N)}\right)\right) + \left(\left(E_{pDye(H-N)}\right) - \left(E_{pSC(VBM)}\right)\right) + \left(\left(E_{el}\right) - \left(E_{pDye(L+N)}\right)\right) \\ &= \ E_{el.} - E_{pSC(VBM)} \\ &= V_{OC2} \ , \end{aligned} \tag{2.8}$$

where the terms are the same as those described in the previous case. The only difference is the energy level of the SC. The VBM is important for the p-DSSC, and the CBM is interesting for use in the n-DSSC. Nevertheless, the summed terms in Equation 2.8 represent the same CT reactions that were addressed in Equations 2.4–2.6. The first term is dye-molecule excitation (Equation, 2.4), the second term is hole injection (Equation 2.5), and the last term is the electrolyte's reduction of the dye molecule (Equation 2.6). As a result, V_{OC2} is the difference between the SC's VBM and the electrolyte's energy level.

Now that the reactions for each individual system have been shown, they can be combined to find the complete pn-DSSC voltage. For this, Equations 2.7 and 2.8 are summed to get the total voltage inside pn-DSSC:

$$V_{OC1} + V_{OC2} = \left(\left(E_{nSC(CBM)}\right) - \left(E_{el.}\right)\right) + \left(\left(E_{el.}\right) - \left(E_{pSC(VBM)}\right)\right)$$

$$= E_{nSC(CBM)} - E_{pSC(VBM)} \qquad (2.9)$$

$$= V_{OC1+OC2} \ ,$$

Thus, the total voltage, $V_{OC1+OC2}$, is related to the energy difference between the two SCs: the n-type CBM and the p-type VBM SC. Because the voltage is the energy per electron, the open-circuit voltage has this final form:

$$\frac{\left(E_{nSC(CBM)} - E_{pSC(VBM)}\right)}{e} = \left|\Delta U_{OC,nSC}\right| + \left|\Delta U_{OC,pSC}\right| = \left|\Delta U_{OC}\right| \propto V_{OC1+OC2} \ , \qquad (2.10)$$

where $\Delta U_{OC,xSC}$ is the potential difference of x-type SC and e is the electron's charge. [75]

However, although the energy-level alignment prefers a spontaneous reaction, it is possible for the created voltage to be small. As shown by Equations 2.9 and 2.10, the difference between VBM_p and CBM_n defines the theoretical voltage. If VBM_p and CBM_n are energetically too close to each other while in contact, the system's open-circuit voltage ($V_{OC1+OC2}$) can be small or nonexistent. For this reason, selecting, tuning, and understanding the behavior of the three components (dye, SC, and electrolyte) in a close interaction are important, as the energy levels can change when in contact. One of the aims of this research is to study the energy levels when a p-type dye molecule is chemisorbed on a p-type SC surface to determine how the energy levels change when they are in contact.

3 Systems and models

In this chapter, the studied compounds are addressed in detail; their advantages and weaknesses are presented as well. These compounds include the derivatives of 4,4-difluoro-4-bora-3a,4a-diaza-s-indacene or boron-dipyrromethene (BODIPY), TPA, and PMI and the SC surfaces of NiO and TiO_2. In the last part of the chapter, the used models and their constructions are introduced. Also, the use of the models is justified. As the main focus of this study is to investigate the interacting dye and SC for p-DSSC, its components, namely NiO and derivatives of PMI and TPA, are discussed in greater detail in this chapter than BODIPY and TiO_2.

3.1 Systems

3.1.1 Semiconductor materials: nickel oxide and titanium dioxide

3.1.1.1 Nickel oxide

As stated earlier, NiO is the most frequently used surface for p-DSSC because alternatives have been found to make no significant difference in efficiency thus far. Its strength is that CARB forms a strong adsorption on the surface, and it is able to transfer holes. It is also widely studied. For example, Shen and coworkers have published experimental information on the band structure of NiO. [76-78] They show that the VBM is constructed of oxygen 2p orbitals while the CBM is constructed of nickel 3d orbitals. [76-79] NiO is also theoretically studied with various methods. These previous theoretical studies show that methods based on Generalized Gradient Approximation, GGA,

and Local Density Approximation, LDA, do not give a band gap larger than 0.7 eV, [79] but it is possible to correct it with Hubbard correction (GGA+U), as shown by Schrön and coworkers. The correction opens up the band gap to 1.8–2.0 eV, depending on the value of *U*. [79]

When the NiO surface is modified by the defects, the energy levels are changed. However, it is shown that the energy levels close up to certain value and do not cross it. This effect is called convergence of energy levels, and it can be examined for all compounds. Lany and coworkers have calculated the E_F saturation for NiO surfaces with defects. According to their study, VBM and CBM will be converged at the certain value of energy when the surface is doped. They used a model that has 64 atoms and is antiferromagnetic (AF). AF spin orientation means that half of the spins are α and β spins, as presented in Figure 3.1. The saturation is recorded for both the n- (removal of oxygen, O^{2-}) and p-type (removal of nickel, Ni^{2+}) doping. It shows that the E_F is changed for 1.6 eV and -0.8 eV for n- and p-type doping, respectively. Their study supports the p-SC nature of NiO. [80]

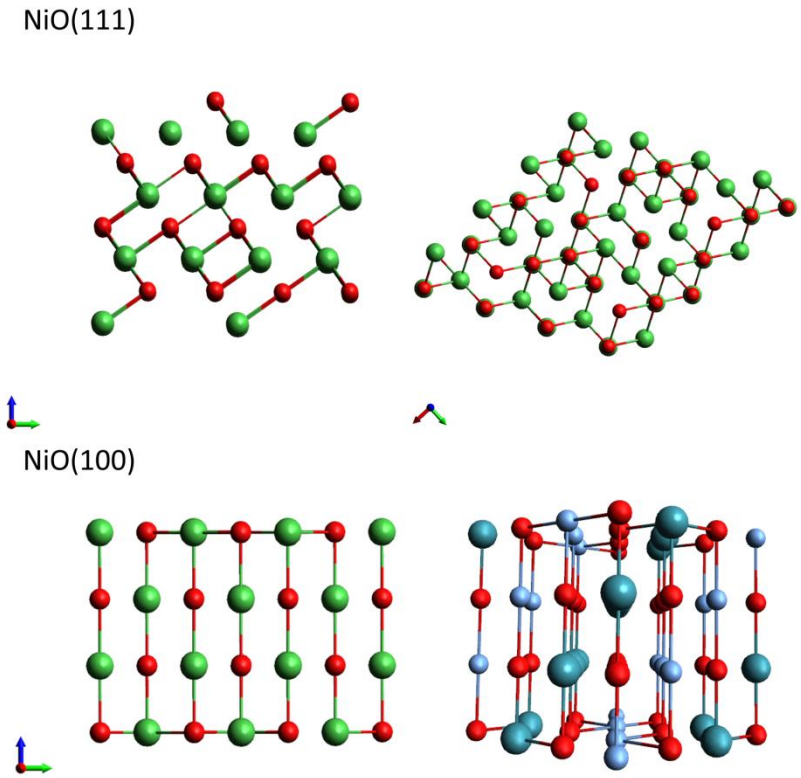

FIGURE 3.1 NiO surfaces. Above, the uncommon NiO(111) surface is shown, and below, the common NiO(100) surface is presented alongside the AF2 spin orientation. Red is oxygen, green is nickel, light blue Ni presents the spin up, and the dark blue presents the spin down. For orientation, the blue arrow is the z-axis, the red arrow is the x-axis, and the green arrow is the y-axis.

In addition, previous studies have shown that WF can vary from 4.7 eV to 6.3 eV for NiO surfaces. [81] This is due to the differences in measurements (ex situ versus in situ, respectively). In most cases, the experimental value is approximately 5.0 eV, as Irwin recorded a WF of 5.3 eV. [81] However, Greiner recorded a WF as large as 6.7 eV, [82] and Kuhlenbeck recorded a WF of 4.3 eV. [83] Therefore, the WF can vary widely depending on the methods, which should consider when the theoretical values are compared with experiments.

As stated earlier, IP is important for the hole carriers, and it links the calculations and experiments together as it approximates the VBM with respect to vacuum level. [84] For NiO, Greiner has recorded an IP of 5.3 eV, [82] and Kuhlenbeck has recorded an IP of 6.0 eV. [83] As the values, both the WF and IP, show, NiO has a shallow VBM;

hence, it is not the best choice for the p-DSSCs. Therefore, i) new ideas are needed or ii) the NiO requires significant improvements. [63]

One way to improve the hole-carrier properties of the NiO surface is to use perovskites. This is done by coating NiO with a perovskite surface. [45] To justify this modification, it is shown that the perovskites have a favorable band-structure alignment with a 0.2 eV difference to the NiO surface, low excitation binding energy, long charge-diffusion lengths, and a broad absorption range with a high absorption coefficient at ~800 nm (near the visible region). However, hole mobility and fill factor are still low, so the power-conversion energy is not so high. [45] Despite the problems with hole carrying, modification with perovskites has shown improvement: The highest power-conversion energy among dye molecules and perovskites is 19.3% with TiO_2 and perovskite versus the classical Grätzel cells, 13%. [85] Despite the perovskite's positive characters, this thesis focuses on the interactions with the NiO surface, as it is still the most popular choice for p-DSSC.

3.1.1.2 Titanium dioxide

TiO_2 is a typical n-type SC. In nature, TiO_2 exists in three forms: rutile, anatase, and brookite. The first two are shown in Figure 3.2. According to the literature, rutile is thermodynamically the most stable, which also makes it the most common in nature and the main source for titanium metal. In contrast, anatase is the most commonly used, as i) it has a larger band gap (3.20 eV) than rutile (3.00 e V), ii) CBM is 0.2 eV higher in energy, and iii) it has higher capability for (-COOH) binding than rutile. [22, 26, 86-88] As a matter of fact, it is widely used in n-DSSC due to its capacity to yield the highest photoconversion efficiencies, chemical stability against photocatalytic reactions, and a good balance between quality and production costs; its nontoxicity and optimal electron injection time also play a role. [89] Even though TiO_2 has a large band gap, it has a low conversion energy because it absorbs only at the ultraviolet part of the photon spectrum. [7] TiO_2 is used in this study due to its frequent use in DSSC, especially in n-DSSCs.

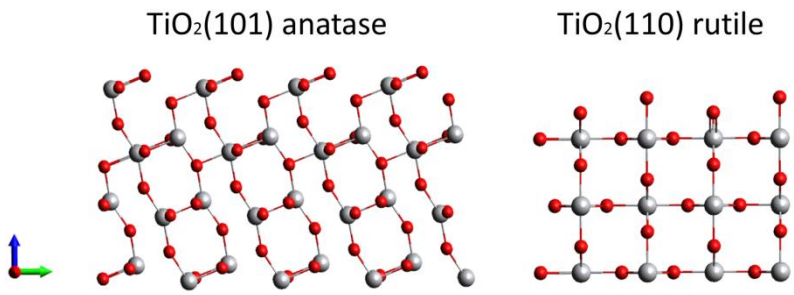

FIGURE 3.2 On the left is anatase, which is the most commonly used inside n-DSSCs. On the right is rutile, which is the most stable at room temperature.

3.1.2 Anchoring groups

The anchoring group is an important link between the dye molecule and the surface. [35] It is the moiety that transfers the charge to the SC's surface. There are several properties that need to be considered before choosing the anchoring group for the dye molecule. One of them is the energy-level alignment with the surface, as it has to favor the CT from the dye (through the anchoring group) to the surface. The second is the binding to the surface, which is just as important as the energy-level alignment. Fortunately, there are many possibilities for the anchoring group.

Due to the wide selection, it is possible to tune dye molecules with various surfaces to enable the maximal CT. [40] The most common anchoring groups with DSSCs are CARB and cyanoacrylic acid, [22, 90] catechol or 1,2-diol (DIOL), [91, 92] pyridine (PYR), [36] phosphonate (PHOS), [93] and acetylacetone. [34] As an example, CARB, DIOL, and PYR are shown in Figure 3.3.

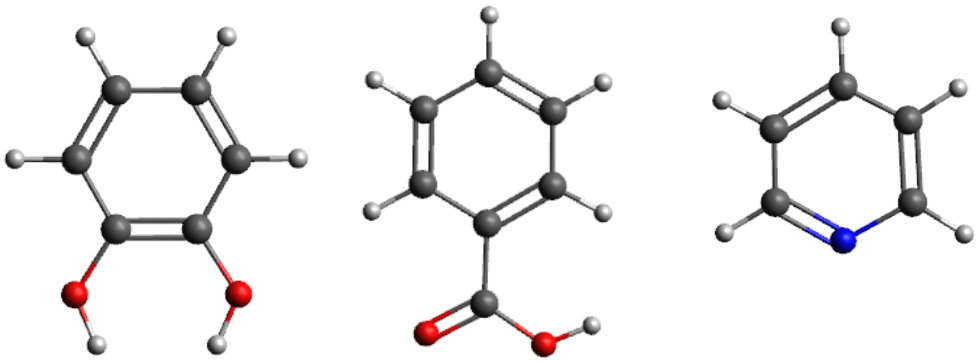

FIGURE 3.3 Examples of the anchoring groups. They are, from left to right, as follows: DIOL, CARB, and PYR.

From the aforementioned anchoring groups, CARB is the most popular and frequently used due to its electron-withdrawing and UV-vis absorption properties with both n-type and p-type DSSCs. [90] Additionally, its electron transfer properties are well known. Not to mention, it is known to bind to NiO surfaces more strongly than to TiO_2. [61] Therefore, it is widely used with NiO(100) surfaces. For these reasons, it has been chosen for this study. The second anchoring group chosen for the study is DIOL. This is because it is said to be a better anchoring group for p-type dye molecules. [92] Its strength lies in its HOMO level, which is physically located on the anchor group (near the surface). Secondly, LUMO or higher orbitals are further localized (away from the surface). [92] The third anchoring group, PYR, has been chosen because it is known to act as an electron acceptor when in contact with TiO_2 surfaces. [36] It is intriguing to see, through calculations, if it can also be tuned with a NiO surface.

3.1.3 Boron-dipyrromethene

BODIPY is used as a dye molecule in n-DSSC (Figure 3.4). It shows strong photoactivity, and it is used for fluorescent switches, [94] laser dyes, [95] dye molecules in DSSCs, [96] and chemosensors. [97] It is also highly tunable by synthesis and various chemical functionalities, [97, 98] such as vinylene groups.

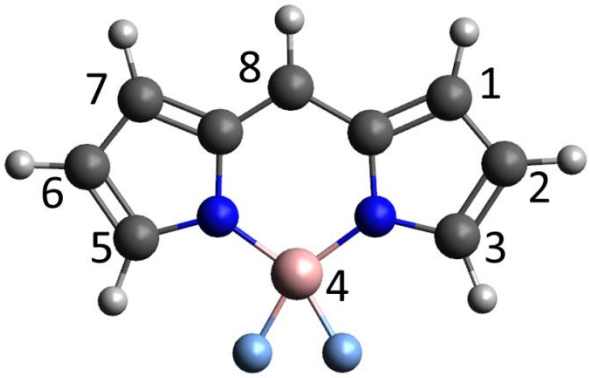

FIGURE 3.4 Derivative of BODIPY and the numbering of the ring.

In this study, BODIPY is screened with four modifications in geometry. First, with three anchoring groups (CARB, DIOL, PHOS), with and without methyl groups in positions 1 and 7 (Figure 3.4), with and without vinylene groups between the donor and BODIPY, and lastly, without a donor. All the structures have two chains of thiophenes attached on positions 3 and 5, followed by the donor, TPA (Figure 3.5), at the end of the chain. The length of the chain is modified because it is interesting to know if the orbitals' energy levels are converged. The BODIPY dye molecules are modeled according to the wishes of the experimental group in Strasbourg [99]. BODIPY is seen as a potential dye molecule for DSSC applications. It is used to screen for various effects in the structure.

3.1.4 Perylene monoimide and trisphenyl amine

Derivatives of PMI (Figure 3.5) are common D-A dye molecules and the most studied with p-DSSC. In fact, PMI–naphthalene diimide (NDI) was the first dye molecule designed solely for p-DSSC. [6, 100] Morandeira and coworkers suggested that the properties of the p-type dye should be reversed in contrast to typical n-type dyes, which inspired the design of PMI–NDI. [100] Firstly, the LUMO is strongly localized on the PMI unit, which is (crucial for the p-type dye) far from the surface. Secondly, it has a long-lived charge-separation state, which prohibits the reversible reaction from reaching the excited state. [53, 54] Thus, PMI and its derivatives are studied as isolated molecules and in contact with the surface to explain their electronic structure and CT.

Finally, TPA is presented. Its derivatives are widely employed for both in-type and p-type dye molecules due to their high efficiencies. Its strengths are a long charge-separation state, high photo current in commonly used electrolytes, and its use as a p-type dye on NiO. [55] In dye molecules, it takes the role of donor, and various linkers have been tested, namely thiophene chains, to improve the photovoltaic current. [6] At present, PMI–TPA with six thiophene rings as a bridge is the best dye molecule for the p-DSSC. [6]. In p-type dyes, it is the moiety that is attached on the anchoring group; therefore, it is utilized with the anchoring group study

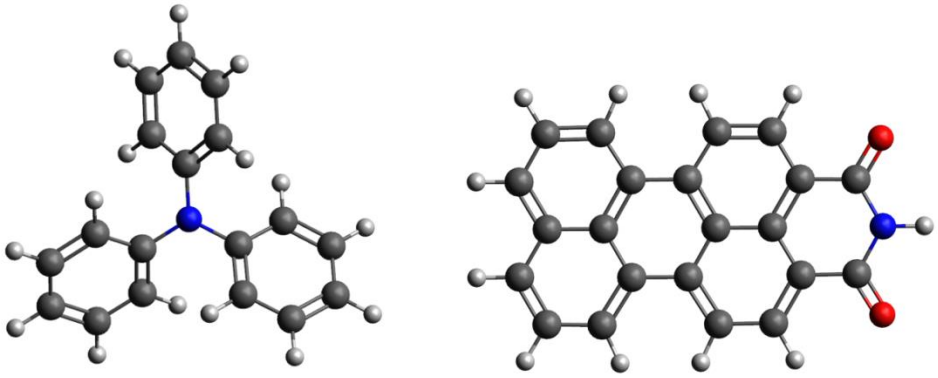

FIGURE 3.5 TPA is shown on the left and PMI on the right. Both are commonly used moieties inside p-type dye molecules.

3.2 Models

The models have been divided into three categories: isolated dye molecules, isolated SCs, and interacting systems. The interacting system is constructed of chemisorbed dye on the NiO(100) surface. The first part covers the isolated dye molecules, BODIPY, PMI, and TPA derivatives. The isolated SC systems are NiO (which is the main focus of this study), and TiO_2. In the last part, the interactions between the derivatives of PMI (complete dye molecules) and TPA (anchoring groups) on NiO(100) surfaces are presented.

3.2.1 Isolated dye molecules: perylene monoimide, boron-dipyrromethene, and trisphenyl amine

The localization of orbitals and the absorption properties of BODIPY derivatives [46] are screened by changing its geometry. The geometrical changes are suggested by an experimental group [99]. One moiety is systematically changed while the thiophene chain is increased from zero (0) to five (5) rings. i) The vinylene group is added between the BODIPY and thiophene chain (Figure 3.6a). ii) Three anchoring groups are modeled: CARB, DIOL, and PHOS (Figure 3.6d–f). iii) The next step is to model methyl groups that are added in 1,7-position (Figures 3.4 and 3.6b). iv) In the last step, the TPA (donor) is removed from the structure (Figure 3.6c). Cyanoacrylic acid is used as the anchoring group in cases i), iii), and iv).

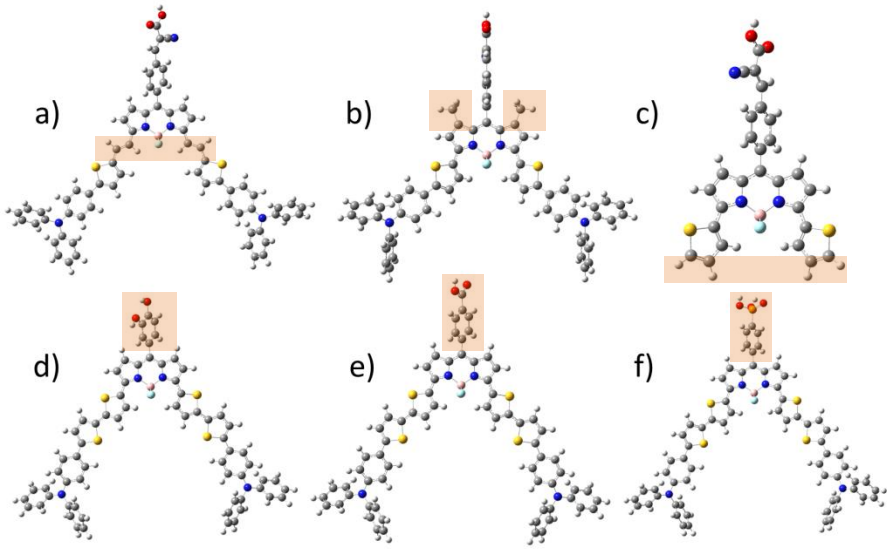

FIGURE 3.6 The modified parts of the BODIPY are a) an added vinylene group, b) methyl groups in positions 1 and 7, c) absence of donor group, TPA, d) CARB, e) DIOL, and f) PHOS as anchoring groups. The modified part is marked with orange.

Four PMI derivatives [53] have been studied. The used models are visualized in Figure 3.7. The first model, TPA–PMI (Figure 3.7a), has TPA with a thiophene chain as a donor and PMI as an acceptor. The last three models have PMI as a donor and NDI (Figure 3.7b–c) or fullerene (C60) (Figure 3.7d) as an acceptor. The latter two (Figure 3.7c–d) also have a phenyl ring (Ph) as a bridge between the donor and acceptor. PMI and its derivatives have been chosen because i) there is experimental data that sup-

ports the fact that they work inside a p-DSSC system and ii) PMI is designed as a p-type dye molecule.

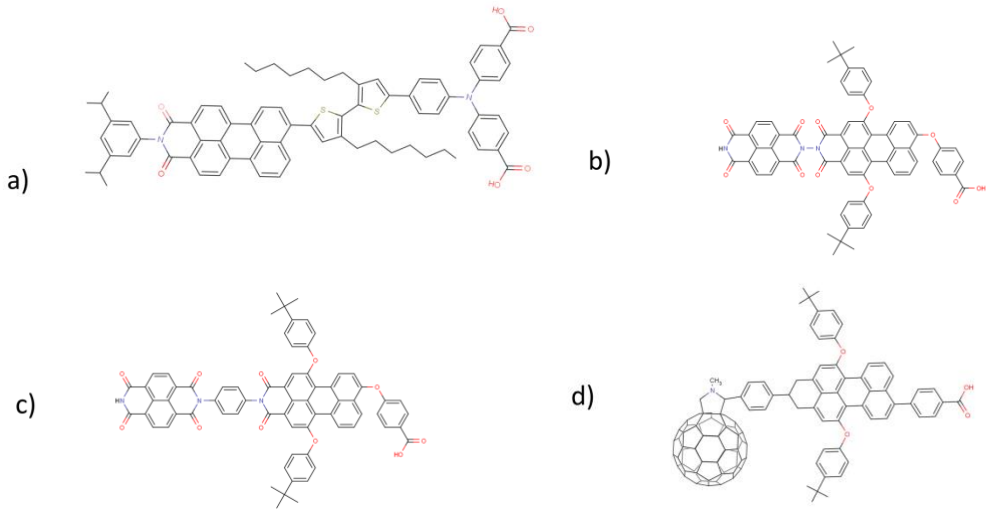

Figure 3.7 Models of derivatives of PMI p-type dye molecules. The dye molecules are a) TPA–PMI, b) PMI–NDI, c) PMI–PhNDI, and d) PMI–PhC60. [1]

In addition, three anchors are studied: CARB, DIOL, and PYR (Figure 3.8) in contact with NiO. The anchoring group is attached on the TPA, which is part of the TPA–PMI, the dye molecule that has one of the highest efficiencies within p-DSSCs. [54] Even though CARB is widely used with both n- and p-type dye molecules due to its CT properties, its HOMO in contrast to VBM of NiO is not suitable for the p-DSSCs. [1] Still, experimentally it has been shown to create a current, so it has been used. The other anchor, DIOL, however, has a favorable energy-level alignment compared to the NiO, as its HOMO is lower than VBM, which favors the hole transport from dye molecule to the SC. The last anchoring group, PYR, has a p-type character; hence, it has been chosen for the study. The main motivation of the PYR is to see alternative anchoring groups and add to our knowledge of the CT properties between the surface and dye molecules within p-type systems. Previous anchoring groups, DIOL and PYR, have been studied with TiO_2 surfaces, but not with NiO.

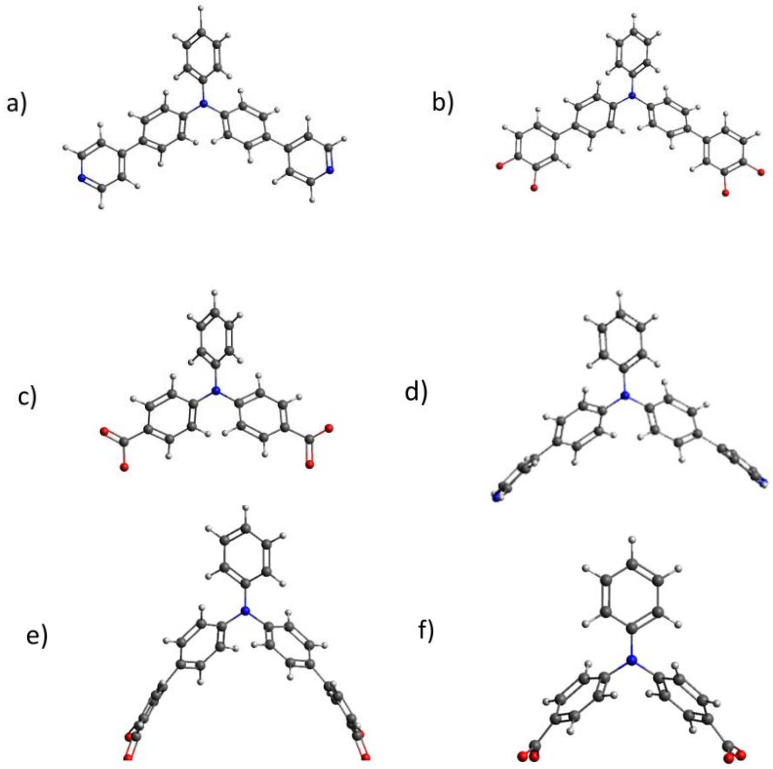

FIGURE 3.8. Models of TPA with three deprotonated (b,c) anchoring groups. Anchoring groups are as follows: a) TPA–PYR, b) TPA–DIOL, and c) TPA–CARB for isolated, relaxed geometry without hydrogens and d) TPA–PYR, e) TPA–DIOL, and f) TPA–CARB for isolated, twisted geometry.

The geometry's effect has been tested by three modifications, including relaxed (minimum energy structure) with hydrogens (except for PYR), relaxed without hydrogens (Figure 3.8a–c), and twisted (without hydrogens, Figure 3.8d–f). The models without hydrogens are neutral (radicals). The twisted geometry is achieved by following two steps: i) First, the interacting system is relaxed; that is, the dye molecule is allowed to relax to a new geometry when in contact with NiO. ii) After the geometry is relaxed, NiO is removed and the received structure of the dye molecule is called twisted (without hydrogens). For the twisted geometry, a single-point calculation is performed to obtain electronic properties. The anchoring groups are: carboxylic acid (CARB), 1,2-diol (DIOL), and pyridine (PYR).

3.2.2 Semiconductor materials: nickel oxide and titanium oxide

An undoped NiO surface is interesting to study for this research because the author desires to see what kind of differences occur between noninteracting and interacting electronic structures. For TiO_2, two motivations exist. i), It is the same as for NiO: to view the differences between the undoped and nitrogen doped (N-doped) surface. ii) It is intriguing to see if the N-doped TiO_2 can be used as a hole-transporting electrode for the DSSC.

NiO has a rock-salt structure and belongs to the *Fm3m* (cubic) space group. [101] The lattice vector of 4.213 Å [1] is used. It was obtained by relaxing NiO bulk (with experimental lattice vector, 4.17 Å [100, 102]) and fixing the surface calculations for both slab models (Figure 3.9), which are cut from the bulk. For the complete dye molecules (Figure 3.6), an 8x8 and four-layer thick surface model (Figure 3.9, left) was used. For the second model, an 8x8 and two-layer thick surface model (Figure 3.9, right) was used with the study for TPA–ANC (Figure 3.5). The (100) surface is utilized throughout the study, as it is known to be the most stable surface. Other surfaces, such as (111) and (110), need to be stabilized by polar liquids or they will form (100) while growing. [103]

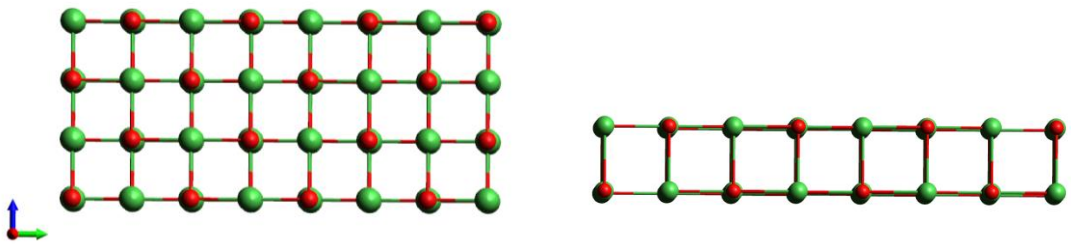

FIGURE 3.9 Used NiO(100) surface slab cuts from the NiO bulk. On the left, the 8×8×4 surface, and on the right, the 8×8×2 surface. Green is nickel, and red is oxygen. The orientation is the same for both surfaces. The blue arrow is the z-axis, the red arrow is the x-axis, and the green arrow is the y-axis.

Anatase TiO_2(101) belongs to the space group of $I4_1/amd$ (tetragonal). A ready slab model (provided by Adriano Panepinto [104]) has been used, and its stoichiometric formula is $Ti_{48}O_{96-n}N_n$, where *n* has values 0, 3, 5, 7, or 9. Nitrogens have replaced oxygens according to Figure 3.10. The levels of doping are 0%, 2%, 3%, 5%, and 6%, respectively. The size of the TiO_2 slab is 20.42×7.55×54.35 $Å^3$, with lattice vectors of a_0

= 3.794 Å, c_0 = 9.518 Å. [105] 500 Å vacuum is used; hence, the real size of the cell is 20.42×7.55×500.00 $Å^3$.

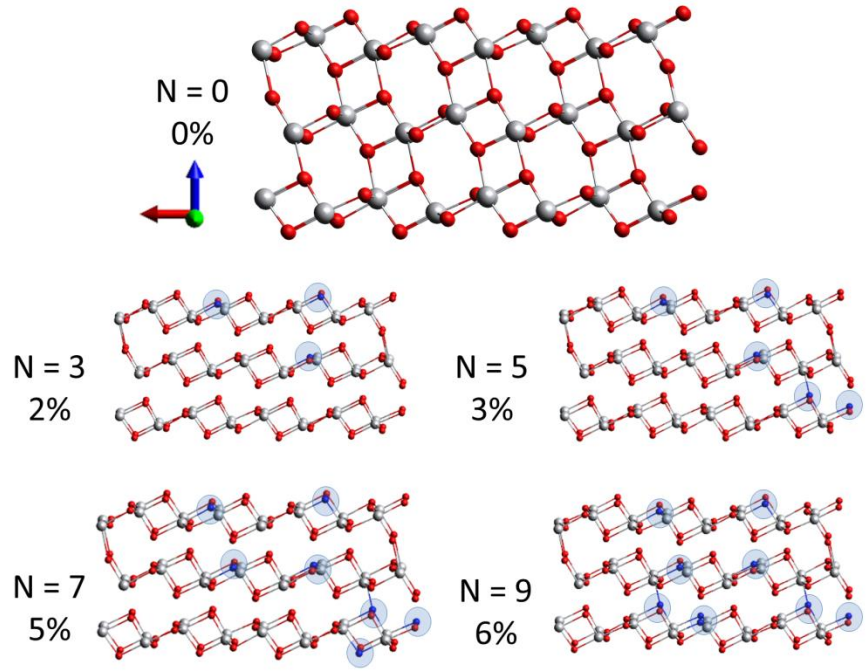

FIGURE 3.10 $Ti_{48}O_{96-n}N_n(101)$ (*n* = 0, 3, 5, 7, 9) anatase. The replaced oxygens are marked with blue circles. Titanium is white, nitrogen is blue, and oxygen is red. The colors for orientation are the same as in the previous figures: The blue arrow is the z-axis, the red arrow is the x-axis, and the green arrow is the y-axis.

3.2.3 Combined systems: perylene monoimide and triphenylamine on nickel oxide

The main motivation to study the combined systems is also the main motivation of the thesis: to understand the interactions when a dye molecule is in contact with the SC surface. This includes the changes in energy-level alignment, possible CT reactions, and interactions between the dye and the surface (chemisorption). In addition, it is worth noting that the systems are not studied at this level of theory (linear combination of atomic orbitals, LCAO, in periodic boundary conditions, PBCs). Most of the systems are studied experimentally or with software (that use PBCs) that utilizes plane waves. The complete description of the methods and the advantages of previous theoretical methods are addressed in the next chapter.

Four PMI dye molecules (Figure 3.11) with a CARB-anchoring group have been chemisorbed on an 8×8×4 NiO(100) surface. The acid groups have been deprotonated, and the free hydrogens have been replaced on the surface oxygens. TPA–PMI has two CARB groups, which allows either one (TPA–PMI-a) or both (TPA–PMI-b) to bind to the surface (dicarboxylate). The rest have one CARB group to bind to the surface. All the structures are relaxed with fixed lattice vectors (4.213 Å). First, the CARB groups chemisorbed on the NiO surface were relaxed to reach the minimum energy structures while keeping the lattice vectors frozen. Second, the rest of the dye molecules were added, covalently bound to the anchor groups, and relaxed.

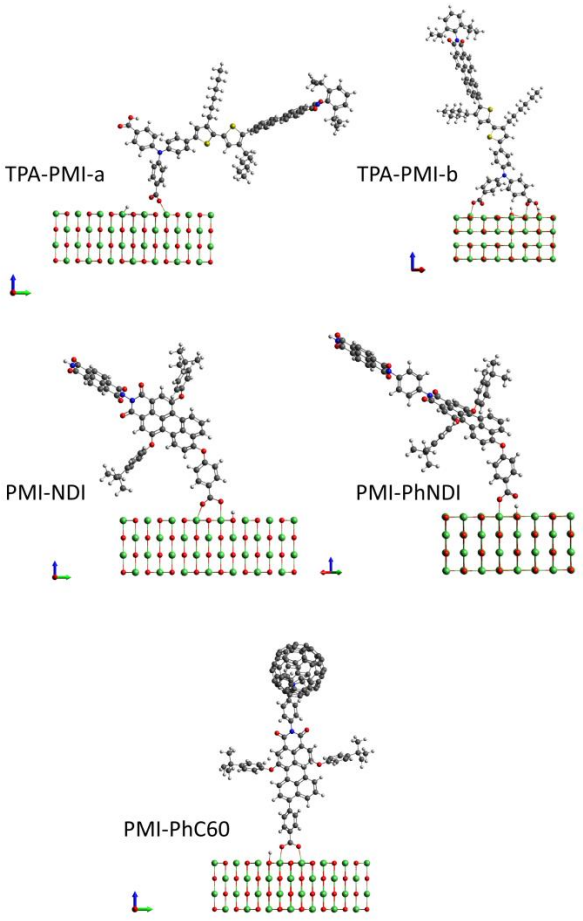

FIGURE 3.11 Combined systems for PMI derivatives. Above, TPA–PMI is presented with both anchoring models next to the PMI–NDI, which is shown without and with the Ph bridge. Below, PMI–PhC60 is illustrated. [1]

The relaxation of PMI–PhNDI and PMI–PhC60 on the NiO(100) surface was more challenging than TPA–PMI and PMI–NDI; hence, there are no results for them. Neverthe-

less, all four dye molecules share similar geometrical structures: PMI is the donor, and CARB is the anchor. Therefore, similar behavior is expected. In addition, dye-dye interactions have been investigated from the combined model when the surface was removed and the dyes were relaxed with fixed lattice vectors.

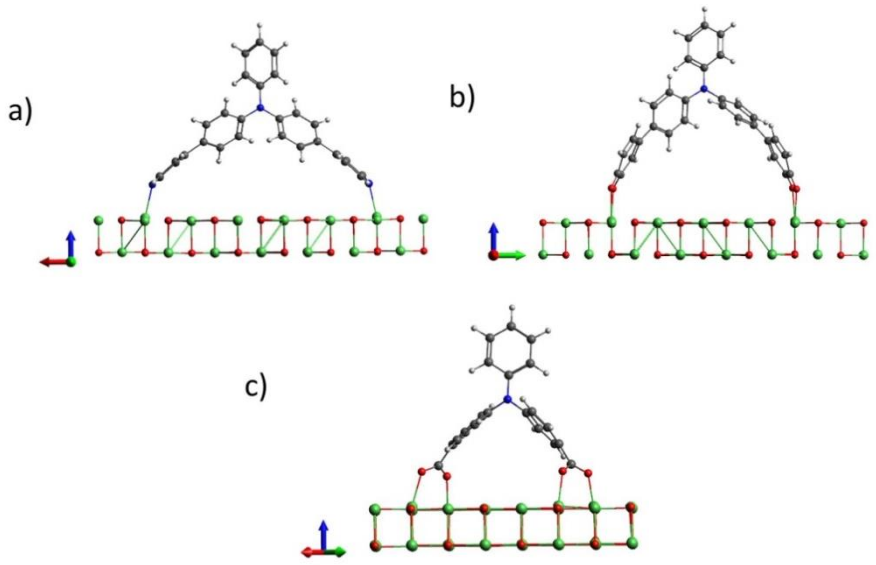

FIGURE 3.12 Models of TPA dye molecules adsorbed on NiO(100) with three anchoring groups. The anchoring groups are a) PYR, b) DIOL, and c) CARB. The colors are the same as in Figure 3.9, with the following additions: Grey is carbon, blue is nitrogen, and white is hydrogen. The blue arrow is the z-axis, the red arrow is the x-axis, and the green arrow is the y-axis

To study the anchoring groups, TPA–ANC (Figure 3.12) has been chemisorbed on the 8×8×2 NiO(100) NiO(100) surface. TPA–ANCs bind on the surface with both oxygens on both anchoring groups. This has been taken into account for our calculations. All the structures are relaxed to the geometry corresponding to the minimum energy structure. Due to the problems with relaxation, hydrogens have not been replaced on the surface. Again, the lattice vector has been fixed (4.213 Å).

4 Computational methods

This chapter starts by explaining the common quantum mechanics behind molecular modeling and quantum chemistry. It begins with the Schrödinger equation, which is the core of quantum mechanical calculations. Also, methods for solving the Schrödinger equation and approximations are presented, namely the Born-Oppenheimer approximation and density functional theory (DFT). Other implications for solving are Variational principle, LCAO, and Bloch functions (BFs). Finally, the types of software used in this study are presented. The following equations are presented in atomic units (a.u.) to render equations for simple form. Therefore, all the units (mass, time, length, etc.), charge of the proton, the mass of the electron, and Planck's constant divided by 2π are fixed to 1 (a.u.)

4.1 Quantum mechanics

4.1.1 Schrödinger's equation

The majority of the properties of matter are determined by its electronic structure. The electrons are responsible for the binding of atoms and other interactions between molecules and solids. Several methods used in this work require calculation of the total energy of a system that consists of many particles. [106] This is done by solving the stationary Schrödinger equation of the systems,

$$H\Psi = E\Psi, \tag{4.1}$$

where *H* is the Hamiltonian operator, which returns the (many-)electron wave function Ψ (eigenvector) and *E* (a scalar), energy. Ψ is the *N*-particle wave function, where *N* is the number of particles (electrons and nuclei). It has a form of $\Psi = \Psi(\boldsymbol{x}_1, \boldsymbol{x}_2, \ldots, \boldsymbol{x}_n)$, where $\boldsymbol{x}_i$ is the coordinates of the particle *i*. From now on, it is considered that Ψ is in Cartesian coordinates (*i.e., 3N* coordinates for *N* particle system). It is also possible to add time, *t*, as a variable and get time-dependent wave function $\boldsymbol{x}_i(\boldsymbol{r},t)$ of the particles. [107, 108] However, for simplicity, the presented equations are time independent. A time-dependent formalism of DFT (TDDFT) is presented later in the chapter. Now, *H* can be written as

$$H = -\sum_i \nabla_{\mathrm{i}}^2 - \frac{1}{2m_k}\sum_k \nabla_{\mathrm{k}}^2 - \sum_i \sum_k \frac{Z_k}{r_{ik}} + \sum_{i<j} \frac{1}{r_{ij}} + \sum_{k<l} \frac{Z_k Z_l}{r_{kl}}\,, \tag{4.2}$$

where, *i* and *j* run over electrons, *k* and *l* run over nuclei, m_k is the mass of the nucleus *k*, ∇^2 is the Laplacian operator (introduced below), *e* is the charge of the electron, *Z* is the atomic number, and r_{ab} is the distance between the particles *a* and *b*. Equation 4.2 consists of both the kinetic (first two terms) and potential energy (last three terms) parts. [107] In the 3D system with Cartesian coordinates, the Laplacian operator has the form

$$\nabla^2 = \frac{\partial^2}{\partial_x^2} + \frac{\partial^2}{\partial_y^2} + \frac{\partial^2}{\partial_z^2}\,, \tag{4.3}$$

where *x*, *y*, and *z* are the 3D coordinates of the particle in a system that has *N* particles. As the size of the system grows (*N* increases), the eigenfunctions become time consuming to solve due to the complex interactions between separate particles. Therefore, the complexity of the functions and the subsequent solving must be reduced.

4.1.2 Born-Oppenheimer approximation

One way to do this is to simplify Equation 4.2 (*e.g.,* with a Born-Oppenheimer approximation). The Born-Oppenheimer approximation decouples the kinetic energy, since the mass ratio of nuclei and electrons is at least 1 800. [107] A stricter, clamped nucleus approximation allows the electronic structure to be solved for fixed nuclear positions

since electron redistribution is much faster than nuclear motion. Therefore, the relaxation of electrons' kinetic energy with respect to the motion of nuclei is imminent. Born–Oppenheimer approximation decouples the terms in regard to the electrons and nuclei and fixes the positions of the latter. Now, the nuclear kinetic energy is independent (of electrons), and nucleus–nucleus repulsion potential energy is constant; that is, the number of particles is reduced to the number of electrons instead of the number of nuclei and electrons. From now on, *N* will refer to the number of electrons in the system. By description, it is clear that the Born–Oppenheimer approximation is very simple and justified in the most of the cases because the quantum character of the nuclei is rarely significant. [107]

4.1.3 Variational principle

The variational principle strives to find a general approximate solution for the wave function, ψ, as close as possible to the true ground-state energy. It works for all observables. Mathematically, it is defined as

$$E_0 \leq \frac{\int \Psi H \Psi d\boldsymbol{r}}{\int \Psi^2 d\boldsymbol{r}^2} = E \ , \tag{4.4}$$

where E_0 is the energy of the true ground state. The trial wave function, ψ, can be normalized, which makes the denominator a unity and simplifies Equation 4.4. In short, the variational principle tells that the energy of the ground state with an approximate wave function is always too high. Thus, the energy is one way to measure the quality of the wave function: the lower the energy, the better the (description of the) wave function. By varying the parameters in the trial wave function, the energy can reach its minimum, which is the estimate of the best ground-state energy. [107]

4.1.4 From the many-body problem to the single-particle problem

Solving the Schrödinger equation is a many-body problem. The most important objective is to understand and predict the properties of many-particle systems and to calculate several measurable quantities, such as bonding energies, polarizabilities, and excitation energies, rather than the wave function itself. [109] With a system of many parti-

cles and interactions, the number of terms in Equation 4.2 increases. It is assumed that the many-electron wave function is an antisymmetrized product of the single-particle wave functions, and the characters of orbitals are independent of the number of electrons. Then, the Hamiltonian (Equation 4.2) is simplified as

$$h_i = -\frac{1}{2}\nabla^2 - \sum_{k=1}^{M}\frac{Z_k}{r_{ik}} + V_i\{j\}, \tag{4.5}$$

where most of the terms are already explained except for $V_i\{j\}$, which is the average potential of other electrons experienced by the surrounding electrons. Now the many-body problem is transformed into the single-electron problem, wherein the electron–electron repulsion is treated in an average way. It is also noted that wave functions are not directly accessible to measurements in this form. However, their quality can be deduced on physical observables *e.g.* electron density.

4.1.5 The linear combination of atomic orbitals

One part of solving Equation 4.1 is to find a quality set of basis functions. It is clear that the function providing the lowest energy is the best, yet the following problem remains: how to find the wave function in an accurate way when the systems size increases. Within a single-particle problem, the system is a linear combination of basis functions. However, in increasing the system size, the amount of functions increases as well. One approach to this problem is to form a wave function using LCAO as a guess wave function. The form of this function is

$$\psi = \sum_{i=1}^{N} c_i \, \Psi_i, \tag{4.6}$$

where ψ (one-electron wave function) is the linear combination of atomic orbitals, Ψ_i are atomic orbitals as basis functions, and c_i are the coefficients. In other words, Equation 4.6 describes the molecular orbital (wave function) of the system as a linear combination of atomic orbitals. [107]

4.1.6 Density functional theory

The most frequently used method to solve Equation 4.1 is called DFT. It reforms the particle-based wave functions in Equation 4.1 with electron density instead. The basic DFT equations differ from 4.1 because with the LCAO described up until now, since Ψ in 4.1 is an anti-symmetrised product of one-electron wave-functions that are independent (except for the Coulomb operator). In DFT, the wave-functions (spin-orbitals for single-particles) and potential in the Hamiltonian depend on the total one-electron density for all electrons in the system. Hohenberg and Kohn established uniqueness and variation principles for exact DFT in 1964, however it was not much used, (particularly outside condensed matter models mainly of metals used) until the Kohn-Sham spin-orbital equations of 1965 which are approximate one-electron expressions containing a potential written as a functional of the density, which also needs to be approximated, in general. [108] DFT is based on two theorems: the existence theorem and the variational theorem. The first, the existence theorem, states that the electron density contains all the information of the electronic structure at the ground state. The second, the variational theorem, states that DFT obeys the variational principle (i.e., the calculated ground-state energy is always equal to or greater than the real ground-state energy). [107, 108]

Despite being a simple and accurate approximation, DFT has its limitations. It does not adequately describe weak interactions such as van der Waals or properties of non-ground states, *i.e.,* excited states, and it is limited in terms of accurately describing “small” (namely thousands of atoms) systems. Fortunately, such limitations can be surpassed by applying various methods, *e.g.* adding a new variable, time *t*, in Equation 4.1. Now, the Equation 4.1 is not stationary and it is possible to calculate electron transition energies, *i.e.* excitations. Naturally, time dependent DFT (TDDFT) is not the only added application to enhance the accuracy of the physical properties. However, the rest are not significantly relevant for this study so they are not mentioned. [31]

To find time dependence, time is added to the Hamilton operator. The relevant theorem is called the Runge-Gross theorem, which is commonly known as TDDFT. The Runge-Gross theorem proves that, for a system evolving from an initial stationary state, there is a one-to-one correspondence between the external time-dependent potential and the time-dependent electronic density. [107-109]

4.1.7 Periodic boundary conditions and Bloch functions

Currently, a system size can reach even one thousand atoms, which is very demanding in terms of solving previous equations exactly. To mention examples of these systems, consider surfaces or the chemisorbed molecules on a surface (dye on an SC surface). Fortunately, these systems tend to be periodic so periodic boundary conditions (PBC) can be applied. With PBC, calculations use relatively small number of particles, in such a way that they experience forces as if they were in fluid. In practice, a part of the system, unit cell, is described and then repeated either in three or two dimensions. [62, 110]

To handle the systems in a realistic way without requiring too much computational time due to the size of the system, a proper mathematical description of wave functions within PBC is needed. The approach is known as Bloch theorem, and it defines the system with BFs. The general form of BFs is

$$\psi(\boldsymbol{r}) = e^{i\boldsymbol{k}\cdot\boldsymbol{r}}u(\boldsymbol{r}), \tag{4.7}$$

where $u(\boldsymbol{r})$ is the position of the (plane) wave and $e^{i\boldsymbol{k}\cdot\boldsymbol{r}}$ is the multiplication factor to generate Bloch wave. The bolded letters are vectors. As stated, BFs follow PBC by repeating a unit cell with translation matrix. This form is typical for plane wave basis set. However, BFs can be expressed within LCAO basis (as in CRYSTAL) as

$$\psi_i(\boldsymbol{r},\boldsymbol{k}) = \sum_{\mu} a_{\mu,i}(\boldsymbol{k})\phi_{\mu}(\boldsymbol{r},\boldsymbol{k}), \tag{4.8}$$

$$\phi_{\mu}(\boldsymbol{r},\boldsymbol{k}) = \sum_{\boldsymbol{g}} \varphi_{\mu}(\boldsymbol{r}-\boldsymbol{A}_{\mu}-\boldsymbol{g})e^{i\boldsymbol{k}\cdot\boldsymbol{g}}, \tag{4.9}$$

where $\phi_{\mu}(\boldsymbol{r},\boldsymbol{k})$ defines the delocalized basis functions, $\varphi_{\mu}(\boldsymbol{x})$ defines the local basis functions, A_{μ} denotes the coordinate of the nucleus in the zero-reference cell on which φ_{μ} is centered, μ specifies a band, $\boldsymbol{\Sigma_g}$ is extended to set all the lattice vectors $\boldsymbol{g}$, $\boldsymbol{k}$ is the wave vector, $\boldsymbol{r}$ is the coordinate of the particles (atoms), and i is the imaginary unit. The sum in Equation 4.8 shows lattice periodicity. Now, the energy exists only at the certain range bands. [111] In short, Bloch theorem and Equations 4.7 and 4.8 state that, after

a translation of a lattice vector, all nondegenerate solutions are also solutions of Equation 4.1.

4.1.8 Different basis sets

The atomic orbitals are localised in real space and delocalised in reciprocal space. Conversely, plane-waves are localised in the first Brillouin zone of reciprocal space and completely delocalised in real space. This confers advantages and disadvantages on the basis set chosen. Atomic orbitals in LCAO are prone to basis set superposition error, since they are local and usually atom-centered, however, they allow for a detailed description of each atom. Plane waves do not suffer from basis set superposition error but are needed in huge numbers for some atom-specific properties. This is corrected in projector augmented waves (PAW), which is based on plane waves and uses pseudopotentials by default. Due to the pseudopotentials, PAW smooths the oscillation that is happening near nucleus in traditional plane wave basis. Both plane wave methods are popular in periodic systems due to their similarity to Fourier series that are periodic by character. [62, 107, 111]

When PBCs are applied, the system usually creates a shift in the vacuum potential (direction orthogonal to the surface). The shift is due to the various potentials at each side of the surface. This phenomenon is visible in systems in which a molecule is on the surface; it can also be seen when the two surfaces of the slab are not mirror images of each other. In other words, the difference in potential is due to the dipole moment (electron rearrangement) of the system. In fact, they are correlated by the equation

$$\Delta E = \frac{-\mu}{A\varepsilon_0}, \qquad (4.10)$$

where $\boldsymbol{\mu}/A$ is the dipole per surface unit in the direction orthogonal (z-axis) to the surface, and ε_0 is the dielectric constant of the vacuum. Equation 4.8 indicates that the direction of the dipole moment is opposite of the shift in the vacuum. [73, 74] This is not a problem within this study because the studied systems are periodic in the xy-plane (parallel to the surface). Thus, the correction has not been applied. However, the potential along the z-axis is possible to calculate, and the dipole moment of the system can be extracted. This information is used later in chapter 5.4 to examine energy levels and to set a common zero for the systems.

4.2 CRYSTAL09 and other software

Due to the periodicity of the studied systems, a software that uses PBC and BF is needed. For this purpose, calculations have been performed by CRYSTAL09. [111, 112] It uses LCAO with BF and is able to apply hybrid functionals, such as the Becke-Lee-Yang-Parr hybrid functional (B3LYP); [113-115] hence, it is an ideal software for the modeled DSSC systems. B3LYP is chosen because these systems are not widely studied with hybrid functionals. However, because it is hybrid functional, it is not pure ab initio method. It will provide overestimated values for energy levels, yet, better agreement with experiments. [116] The choice of used basis set for BODIBY is the same as the basis used by the previous student on the study. This way, a consistency is provided. The basis set used for derivatives of PMI and TPA were tested and it was settled down with the following as they provided both the convergence and accurate results.

The CRYSTAL09 program was used for main calculations: isolated dye molecules, NiO, TiO_2, and interacting systems. The B3LYP density functional was used with 86411/6411/41, [117] 8411/411, [117] 8651/651/3, [118] 8411/411, [118] and 631/31/1 [119] basis sets for Ni, O (of NiO), Ti, O (of TiO_2), and N, respectively. The chosen basis sets are manufactured to the corresponding surfaces and used. The references for these basis sets provide more information. For the complete dye molecules, a TZVP [120] basis set was chosen for molecule TPA–PMI, while a 6-31G(d,p) [119] basis set was used for molecules PMI–NDI, PMI–PhNDI, and PMI–PhC60 and anchoring groups CARB, DIOL, and PYR. The NiO bulk model was optimized using 65 unique k-points, and the surface model contained 34 unique k-points. When dye molecules were adsorbed on the surface, one unique k-point was used in all three directions. Lastly, in the case of the TiO_2(101) surface, 10 unique k-points were used.

As CRYSTAL09 is specialized for PBC calculations, it is not generally a tool that is powerful enough to solve for properties of single molecules in a vacuum, and it does not perform TDDFT calculations (this is corrected in the latest version of CRYSTAL). Therefore, Gaussian09 has been utilized alongside our study to examine single dye molecules and their UV-Vis spectra. In addition, both types of software utilize B3LYP, so the risk of error is minimized when the software is changed between calculations.

Preliminary optimizations were performed with DFT and TDDFT calculations of free dye molecules in a vacuum with the Gaussian 09 program. The global hybrid functional, B3LYP, and the 6-31(d) basis set are equipped to relax the ground-state geometries. Additionally, the vibrational frequencies with DFT and the electronic transitions between the ground and excited states with TDDFT were carried out with Gaussian 09. [121] The absence of the imaginary frequencies ensured the minimum energy structures, while molecular orbital energies and electronic excitation energies were calculated to examine possible CT properties.

4.3 Keywords

The following keywords were used to describe the system: EIGSHIFT, LEVSHIFT, ATOMSPIN, SPINLOCK, FMIXING, BROYDEN, and SMEAR. The AF_2 spin state for NiO has been determined by the keyword ATOMSPIN, and it was locked for 20 self-consistent field cycles by the keyword SPINLOCK. In addition, the preferred Ni α and β d-orbitals were lowered in energy to ease the AF's (Figure 3.1, right) initial guess occupation for the first SCF cycles by the keyword EIGSHIFT. To prevent the occupied states from mixing with the unoccupied states, the VBM was lowered by the keyword LEVSHIFT. FMIXING and BROYDEN describe how much the SCF guess is allowed to change for the next cycle. The difference is that the initial FMIXING value can be changed with BROYDEN after a certain amount of SCF cycles (*e.g.,* 20–50 depending on the system) have passed. In the beginning of the self-consistent field cycles, a higher mixing rate (90 to 80) for 20–30 cycles was used, after which BROYDEN changes the FMIXING value to 55. The same principals were used for both isolated and interacting systems.

5 Results and Discussion

The chapter explains the results of isolated and interacting systems. The isolated systems consist of the derivatives of BODIPY and PMI, SC surfaces (NiO and TiO_2), and anchoring groups (CARB, DIOL, PYR). The studies on interacting systems focus on the electronic structure and electronic interaction between NiO and the derivatives of PMI and TPA. All of the models were previously presented and illustrated in chapter 3. The motivation to study isolated dye molecules and surfaces is to understand their properties and how to enhance them through modifications. The motivation for studying the interacting systems is also simple: to see how the properties change in comparison to the isolated systems and learn from them. The learning is accomplished by suggesting and predicting the changes for non-studied systems and providing insight regarding what to study in the future.

5.1 Modeling of isolated boron-dipyrromethene derivatives

BODIPY and its derivatives have been screened to study the effects of different structural changes for the electron transitions. The aim of the screening is to create a dye molecule suggestion for synthesis, which has the most promising properties. These properties include i) an electron transition toward the anchoring group (or toward the surface) and ii) the saturation of orbitals' energy. The saturation of the orbitals' energy means that the energies of the orbitals are fixed and do not change, even though the chain length increases within BODIPY. It is an interesting concept to address, as it will set the limit for the energies of orbitals for different structures. The localization of orbitals focuses only on the most important energy levels. The importance is defined by the

strongest electron transitions, which are chosen according to the following rules: i) the f-value (or, in other words, the intensity of the peak) of the transition is ~1.0 and ii) the sum of the contributing orbitals is equal to, or greater than, 90%.

All of the models have been shown previous chapters on Figures 3.6 (the models) and 3.4 (numbering of the BODIPY for methyl positions). In all cases, the units of thiophenes have increased from 0 to 5 units. The studied differences are i) the presence or absence of the vinylene group inside the acceptor, ii) various anchoring groups (CARB, DIOL, and PHOS), iii) the position of the methyl groups, and iv) the absence of a donor group (TPA). The motivation to study BODIPY is to find new alternatives for dye molecules and to define the impact of structural changes on electron transitions.

5.1.1 Vinylene group

The BODIPY with the vinylene group (Figure 3.6a) was screened to study its properties as a dye molecule for n-DSSC. The anchoring group that was used is cyanoacrylic acid. It is expected to see that the energy levels, localization of orbitals, and transitions change when the chain length is increased. Figure 5.1 shows the energy levels of the frontier orbitals, which are also illustrated in Figure 5.2. The strongest excitations are presented in Table 5.1

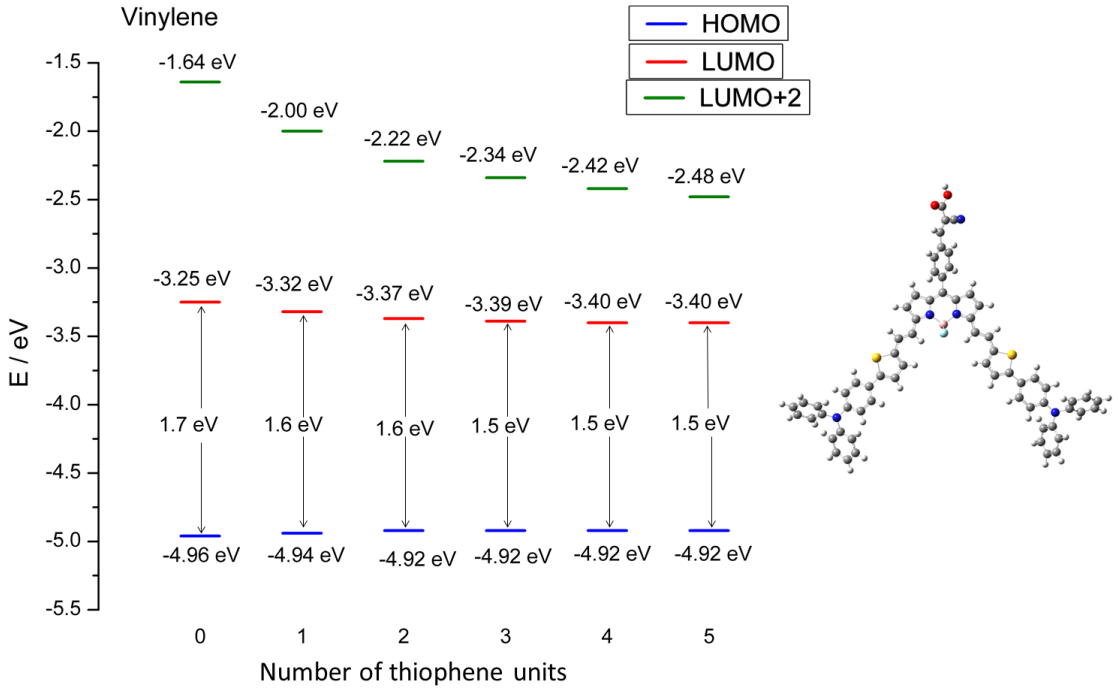

FIGURE 5.1 Energy levels of the energy of the frontier orbitals of BODIPYs with the vinylene group. The energies are also shown with the orbital localization of orbitals in Figure 5.2.

Figure 5.1 shows the saturation of the orbitals' energy levels. First, the energy of LUMO+2 decreases in energy until it is converged to approximately -2.5 eV. The same phenomenon is recorded for the energy of the LUMO orbital, which is converged approximately at -3.40 eV. The saturation energy of HOMO (-4.92 eV) is independent of the number of thiophene units.

Next, the localization of orbitals (HOMO, LUMO, LUMO+2) was analyzed (Figure 5.2). It is evident that the HOMO is localized both on anchoring group and thiophene chain, as is LUMO. In contrast, LUMO+2 is localized only on the thiophene chain. According to Figure 5.2 the localization of the orbitals is not affected by the length of the chain.

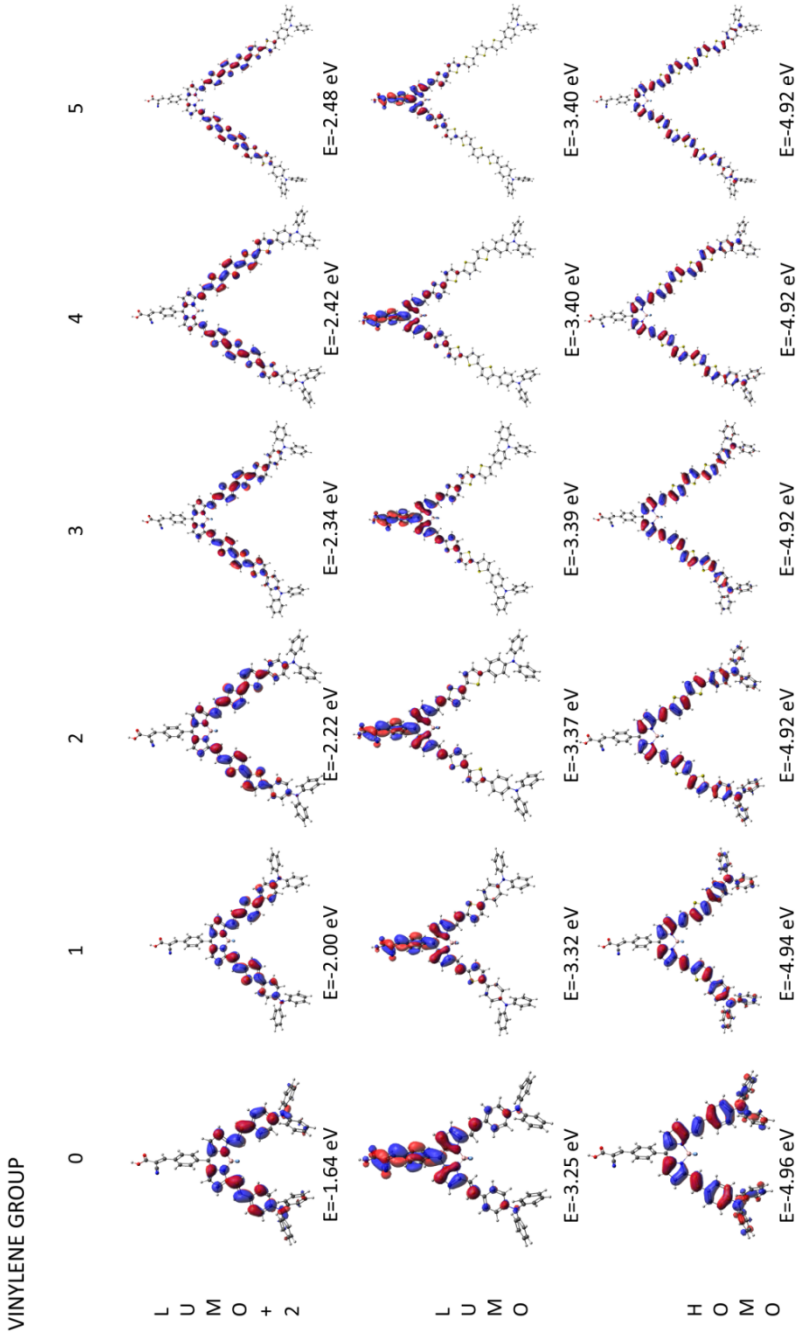

FIGURE 5.2 Frontier orbitals of BODIPYs with the vinylene group. The chain length increases from left to right and the number of oligothiophene units is shown above the molecules. The orbitals are shown from up to down, LUMO+2, LUMO, and HOMO, and their respective orbital energies are shown below the molecule.

TABLE 5.1 The transitions of electrons of the BODIPYs with the vinylene groups and the corresponding absorption wavelengths (λ), oscillator strengths (f), and percentage of the contributing orbitals (%).

Model	Orbital	λ / nm	f-value	%
0	HOMO → LUMO	417	0.8	82
	HOMO-3 → LUMO			13
	HOMO → LUMO	409	1.4	83
	HOMO-3 → LUMO			11
1	HOMO → LUMO	881	1.1	100
	HOMO → LUMO+2	465	2.1	79
	HOMO-3 → LUMO			15
2	HOMO → LUMO	921	1.1	99
	HOMO → LUMO+2	509	2.4	89
	HOMO-3 → LUMO			5
3	HOMO → LUMO	941	1.3	99
	HOMO → LUMO+2	540	2.4	92
4	HOMO → LUMO	949	1.3	98
	HOMO → LUMO+2	559	2.6	91
5	HOMO → LUMO	956	1.4	97
	HOMO → LUMO+2	576	2.6	87
	HOMO-1 → LUMO+3			7

Table 5.1 and Figure 5.3 show the electron transitions. First, Table 5.1 indicates that the strongest excitations are from HOMO to LUMO+2, which happens inside the donor moiety. Therefore, the excited electron will relax to the lower states, which are on the anchoring group (LUMO). The second strongest excitation is from HOMO to LUMO, which is from the donor to the acceptor. Both excitations are good for n-type dye molecules because the electron is moving from the donor closer to the surface. According to Figure 5.3, the strongest absorption goes through a shift from 400 nm to 600 nm when the number of thiophenes is increased in the chain. The same absorption is related to the transition from HOMO to LUMO+2 (inside the donor). As previously stated, the related orbitals are localized on the chain; hence, the chain length lowers the energy for transition. The second strongest absorption peak is at 900 nm – 960 nm, which is related to the transition from HOMO to LUMO (from donor to acceptor). Again, a shift to lower frequency is observed (Figure 5.3).

However, this is not the case for molecule without thiophene unit. It does not have a strong excitation from HOMO to LUMO+2. Instead, it has two strong excitations at 409 and 417 nm with f-values of 1.4 and 0.8, respectively. Taken account that the transition

from HOMO to LUMO+2 with other molecules have f-value ~2.0 (around 410 nm), the peak of molecule 0 seen in Figure 5.3 is a sum of two strong transitions. A closer look reveals that both transitions of molecule with 0 thiophene units are similar by character, so the peak can be treated as one. However, a question arises: why two similar and strong transitions occur separately? One reason might be the methodology. It is known that B3LYP does not always give transitions accurately, thus, CAM-B3LYP is usually performed alongside for accurate transitions. Indeed, the study with CAM-B3LYP was performed and the results were being analyzed during the writing process. Therefore they are not presented within thesis, but they are expected to be published in near future.

To conclude the results of the vinylene group, the length of the chain eventually saturates the energy levels of LUMO and LUMO+2. After three units of thiophene, the energy is said to be converged. Therefore, the chain length of 3 to 5 is enough for an optimal dye molecule because the change in energy of orbitals will be minimal with longer chains. Lastly, the expected properties are favorable because the electron is transferring toward the anchoring group.

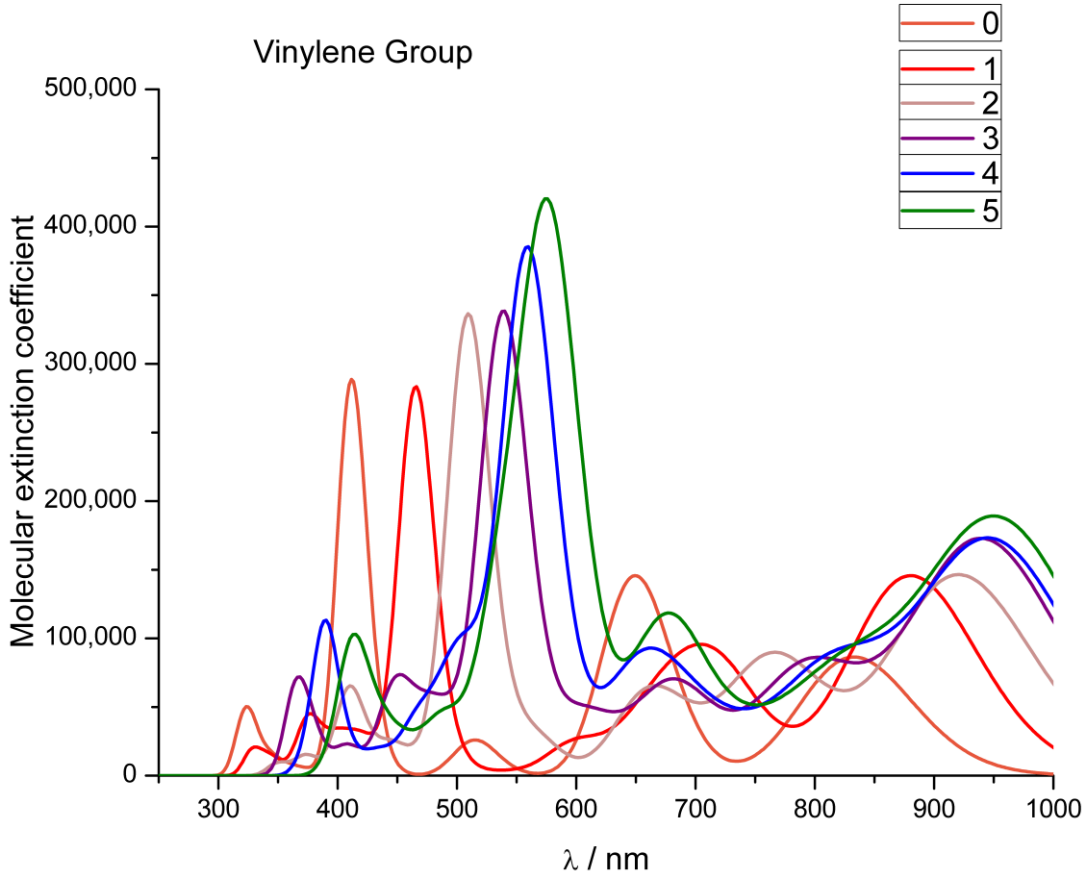

FIGURE 5.3 UV-Vis of the BODIPY with vinylene groups that include different chain lengths.

5.1.2 Anchoring group

The effects of the anchoring groups were studied in the same manner as was applied within the previous case with the vinylene group. Later, in subchapter 5.4, the effects of the anchoring group when it comes into contact with the surface are investigated. Therefore, in this subchapter, the focus is to understand the impact of different anchoring groups on the energy levels, localization of orbitals, and electron transition within molecule. The energy levels of the orbitals are presented in Figures 5.5 and 5.6, electron transitions are provided in Table 5.2, and the UV-Vis spectra is shown in Figure 5.4. The models were previously shown in Figures 3.6d-f.

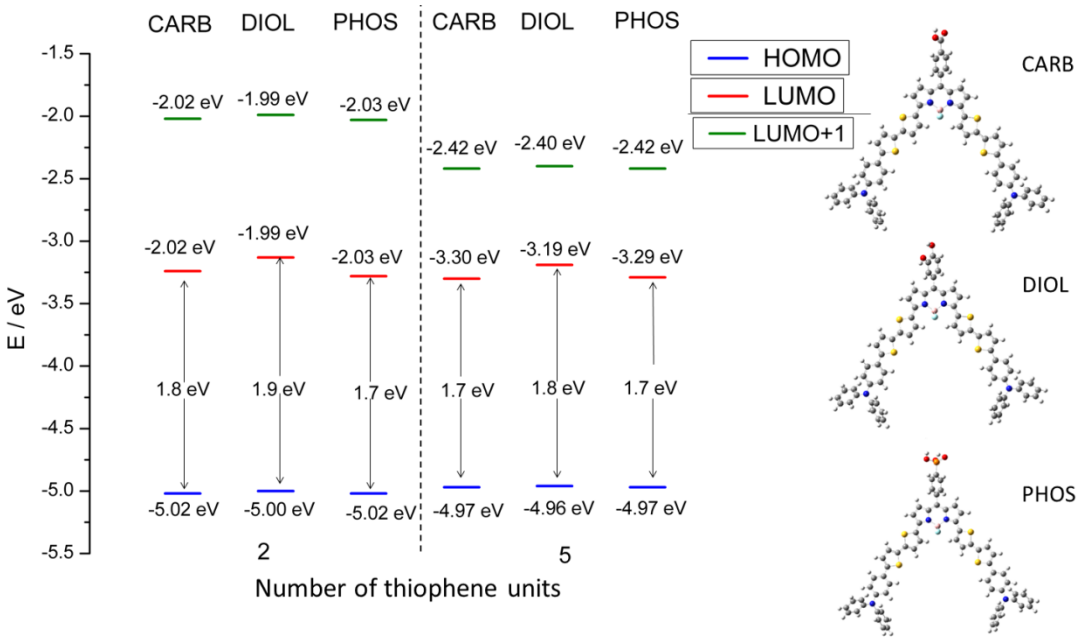

FIGURE 5.4 Energy levels of different anchoring groups of BODIPYs. CARB is on the left, with two and five thiophene units. In the middle, DIOL with two and five thiophene units is shown. On the right, PHOS is shown with two and five thiophene units. The chain increases from left to right.

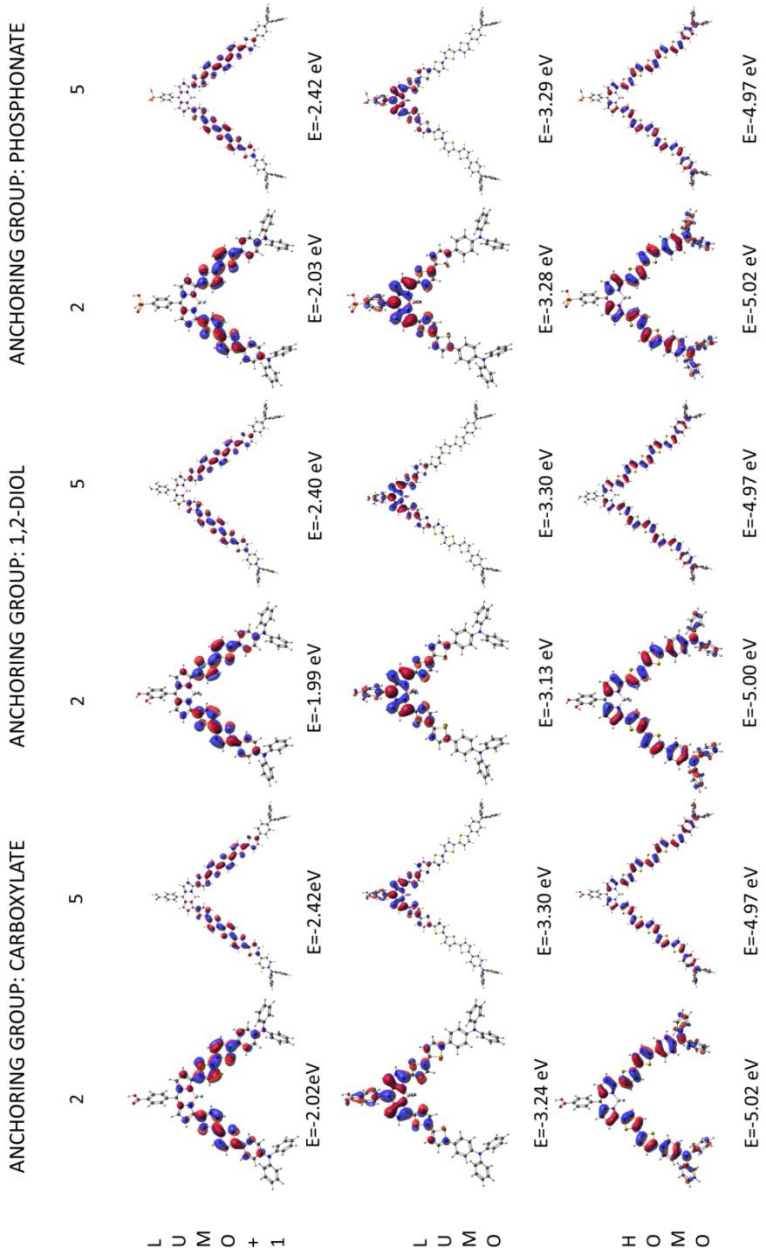

FIGURE 5.5 Frontier orbitals of different anchoring groups of BODIPYs. CARB is on the left with two and five thiophene units. The DIOL is in the middle, with two and five thiophene units. The PHOS is shown on the right, with two and five thiophene units. The chain increases from left to right and the number of oligothiophene units is shown above the molecules. Orbitals, from up to down, are LUMO+1, LUMO, and HOMO. The number below each dye molecule is the respective orbital energy.

As in the previous case, the energy levels are converged when the chain length increases. The converged levels are (-2.42)–(-2.40) eV, (-3.30)–(-3.19) eV, and (-4.97)–(4.96) eV for LUMO+1, LUMO, and HOMO, respectively. As seen, the anchoring group makes a small difference for the energy levels with the same number of thiophenes. The biggest change is for the localization of the LUMO orbitals (Figure 5.5). According to Figure 5.5, LUMO is not completely on the anchoring group compared to the previous case with cyanoacrylic acid. The following order of decreasing localization of orbitals on LUMO is seen: CARB>DIOL>PHOS. This can be taken into account for planning n- and p-type dyes, as was explained earlier in chapter 3. Since the LUMO is localized on the anchoring group in the case of CARB, it is a desired option (for n-type). However, when compared to the previous case, cyanoacrylic acid is more localized on the anchor (and LUMO) than CARB. Therefore, in these three anchoring groups, the BODIPY did not receive any improvement from the point of view of localizing the orbitals because LUMO was drawn away. However, the information can be used to design p-type dyes, as they benefit if the LUMO is not localized on the anchoring group. Accordingly, PHOS could be used as the anchoring group on the p-type SC surface to investigate its CT properties.

TABLE 5.2 Transitions of BODIPY with CARB, DIOL, and PHOS, types of the strongest excitation, corresponding absorption wavelengths (λ), oscillator strengths (f), and percentage of the contributing orbitals (%).

Model	Orbital	λ / nm	f-value	%
CARB(2)	HOMO → LUMO	818	1.0	99
	HOMO → LUMO+1	464	1.8	91
DIOL(2)	HOMO → LUMO	782	1.0	99
	HOMO-4 → LUMO	452	0.8	52
	HOMO → LUMO+1			38
PHOS(2)	HOMO → LUMO	834	1.0	99
	HOMO → LUMO+1	465	1.8	92
CARB(5)	HOMO → LUMO	867	1.2	94
	HOMO → LUMO+1	551	2.4	82
	HOMO-1 → LUMO+2			14
DIOL(5)	HOMO → LUMO	825	1.3	93
	HOMO → LUMO+1	550	2.4	80
	HOMO-1 → LUMO+2			13
PHOS(5)	HOMO → LUMO	864	1.2	94
	HOMO → LUMO+1	551	2.4	82
	HOMO-1 → LUMO+2			14

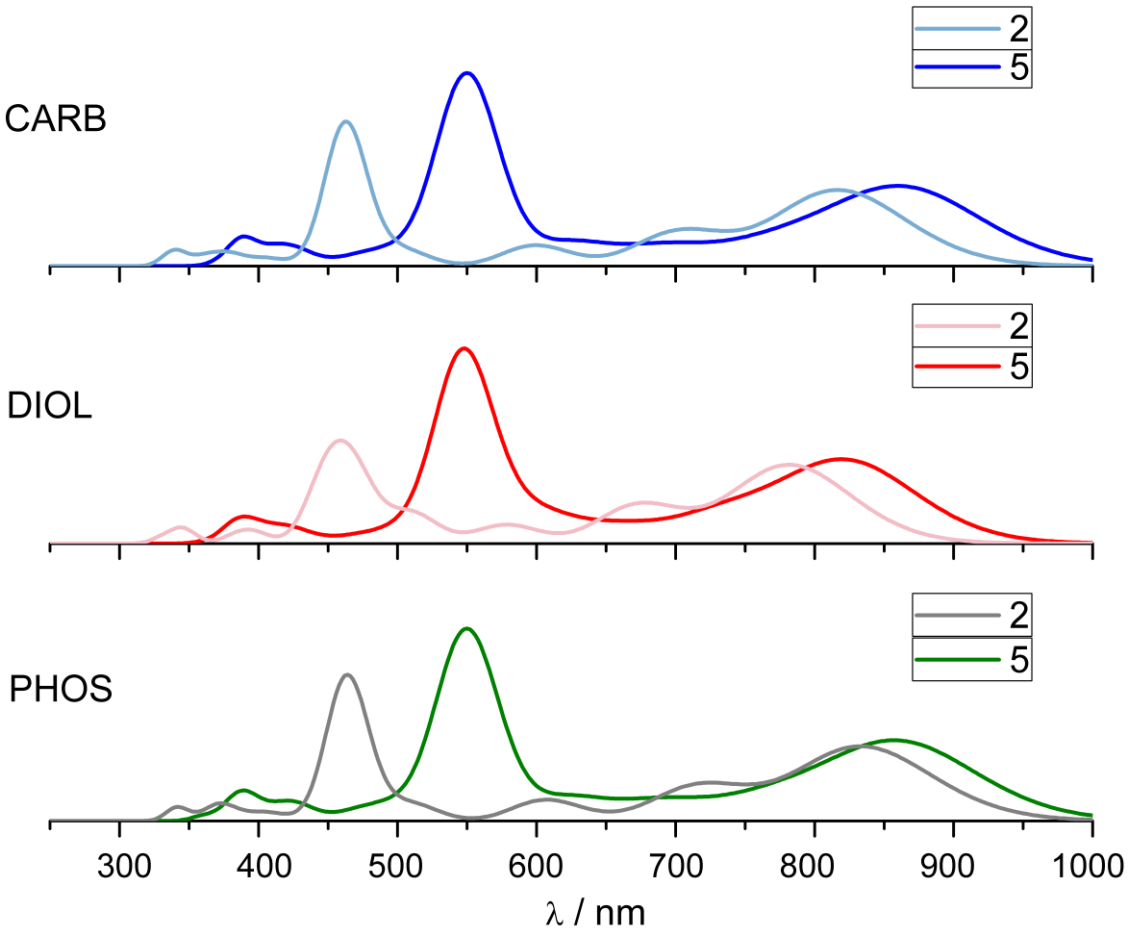

FIGURE 5.6 The simulated UV-Vis spectra of BODIPY with CARB (above), DIOL (middle), and PHOS (below) with different chain lengths. The line is added to provide the ability to view the shift for the second-strongest transition between structures.

Table 5.2 and Figure 5.6 present the electron transitions for different anchoring groups. It is noticed that they are similar to the previous case with the vinylene group. This means that two strong transitions are seen: the strongest transition is from HOMO to LUMO+1 (inside the donor moiety) and the second-strongest transition is from HOMO to LUMO (from donor to acceptor). The first transition that happens inside the donor moiety goes through a shift, from ~550 nm to ~460 nm. Since the transition happens inside the oligothiophene chain, which is the same in all three cases, no differences are observed. Conversely, the second strongest transition (from donor to acceptor), between 800 and 900 nm, has an observable shift between three anchoring groups. This is due to the nature of the transition as it happens from HOMO to LUMO, where LUMO

is partially localized on the anchoring group. As stated earlier, the anchoring group impacts the localization of LUMO; hence, it is natural that it impacts the energy of the transition, too. Figure 5.6 shows that DIOL has a blue shift compared to the CARB and PHOS. The latter two are practically the same.

In conclusion, the CARB and PHOS are good alternatives as an anchoring group for BODIPY. However, as stated earlier, PHOS has the least orbital localization on the anchor (and LUMO) and CARB has less than cyanoacrylic acid. For this reason, cyanoacrylic acid is the best option for BODIPY and PHOS is a good suggestion for the p-type dyes.

5.1.3 Methyl group

The third deviation is the presence of the methyl groups, and we have screened three possibilities. As in the previous cases, the energy levels (Figure 5.7), localization of orbitals (Figure 5.8), electron transition (Table 5.3), and UV-vis (Figure 5.9) are investigated. It is expected to see a change that at least one of the previously mentioned properties for the BODIPY can be improved for the n-DSSC. The model of the structure was presented in Figure 3.6b and the numbering of the positions was shown in Figure 3.4.

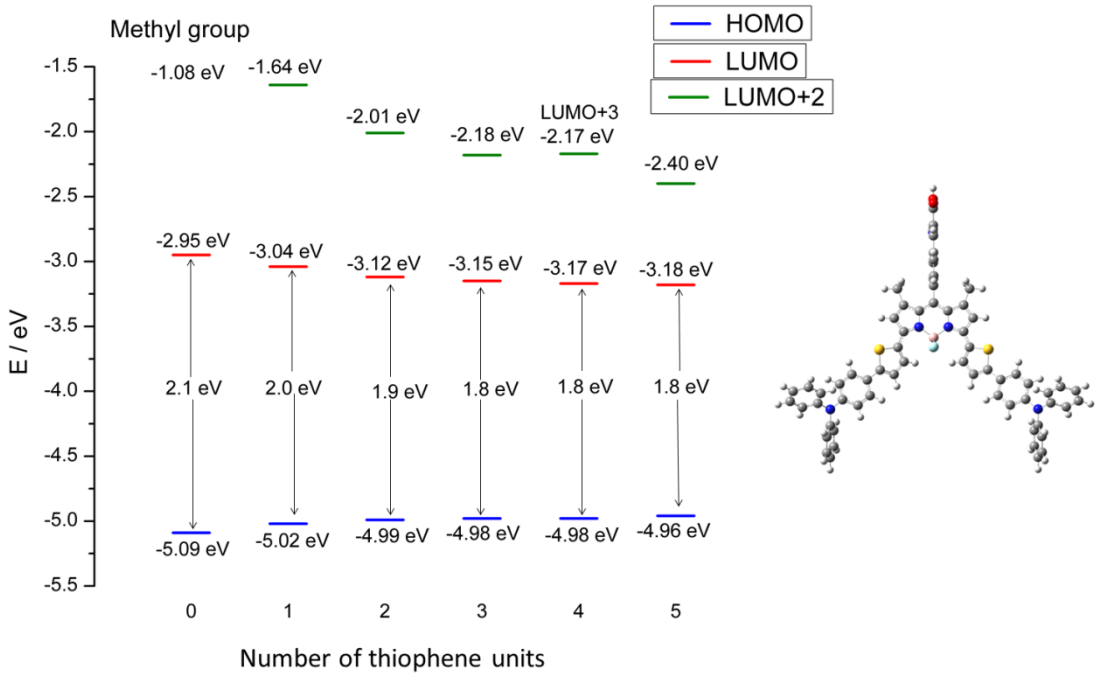

FIGURE 5.7 The energy levels of the methyl group in the 1,7 position in BODIPY with various lengths of thiophene rings. The chain increases from left to right and the number of oligothiophene units is shown above the molecules. The orbitals appear from up to down, LUMO+2, LUMO, and HOMO. The number below the dye molecules is the energy of the orbital.

Again, the energies are converged as follows: -2.40 eV, -3.18 eV, and -4.96 eV for LUMO+2, LUMO, and HOMO, respectively. Here we observe that the energy of the LUMO orbital is higher than it was in the previous cases. This finding is logical, as the localization of LUMO (Figure 5.8) has a drastic change. The LUMO is no longer located on the anchoring group except in the case of 0 thiophene rings. This is due to the steric effect that is caused by the methyl group. They are positioned close to the anchoring group—in this case, cyanoacrylic acid—so that it twists the anchor orthogonal to the rest of the structure. Since the anchoring group is orthogonal, the orbitals do not overlap between the chain and the anchoring group. Even though it is not desirable for the n-type dye molecule not to have LUMO localized on the anchoring group, in this case, the methyl group can lengthen the lifetime of charge separation state. This property is good as long the lifetime of the electron–hole pair does not rapidly reduce back to the ground state.

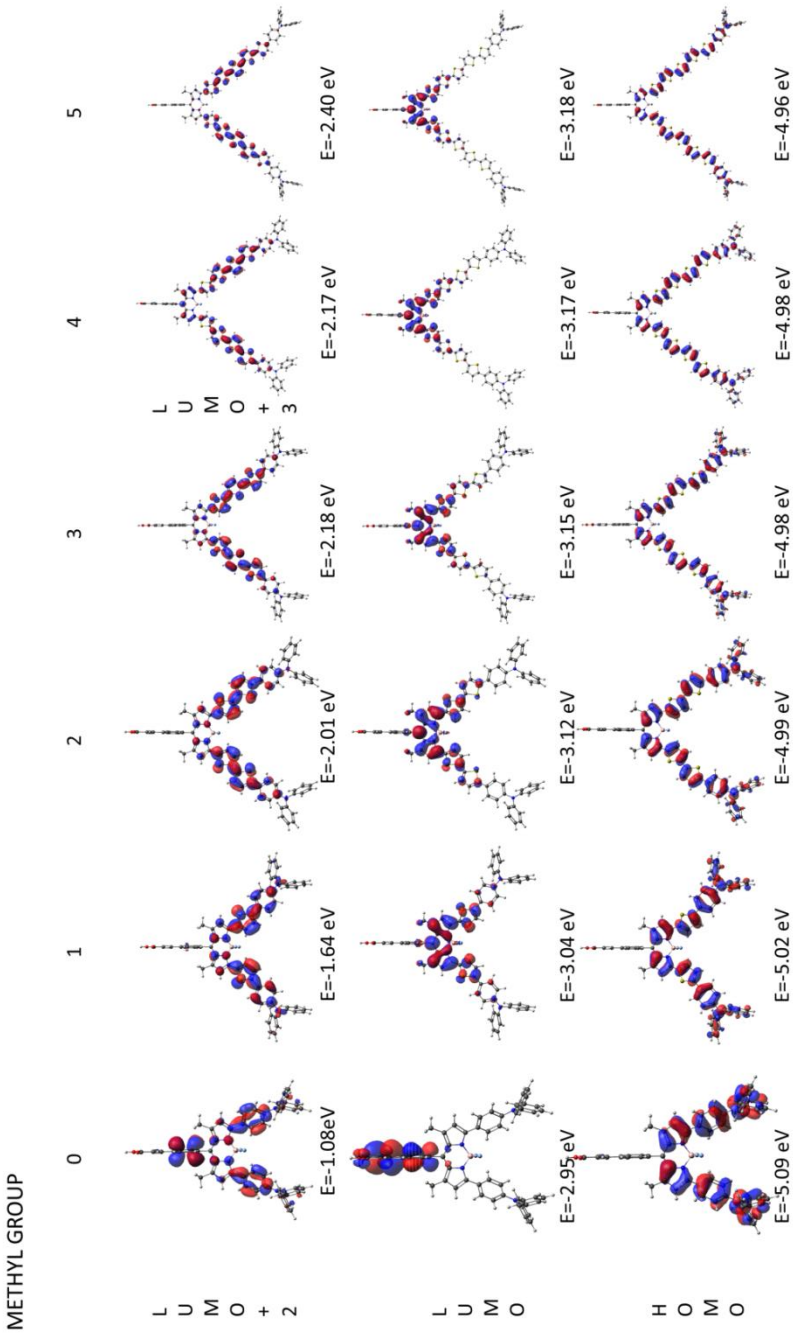

FIGURE 5.8 The methyl group in the 1,7 position in BODIPY with different lengths of thiophene rings. The chain increases from left to right and the number of oligothiophene units is shown above the molecules. Orbitals are from up to down, LUMO+2, LUMO, and HOMO, except for the case with 4 rings as the LUMO+3 presented. The number below the dye molecules is the corresponding orbital energy.

TABLE 5.3 Transitions of BODIPYs with the methyl group in positions 1 and 7, types of the strongest excitation, corresponding absorption wavelengths (λ), oscillator strengths (f), and percentage of the contributing orbitals (%).

Model	Orbital	λ / nm	f-value	%
0	HOMO → LUMO+1	660	0.6	99
	HOMO → LUMO+2	347	0.8	87
	HOMO-8 → LUMO+1			3
1	HOMO → LUMO	731	1.1	99
	HOMO-3 → LUMO	403	1.4	54
	HOMO → LUMO+2			39
2	HOMO → LUMO	779	1.1	99
	HOMO → LUMO+2	465	2.1	83
	HOMO-3 → LUMO			12
3	HOMO → LUMO	797	1.3	98
	HOMO → LUMO+2	498	2.0	91
4	HOMO → LUMO	808	1.3	96
	HOMO → LUMO+3	526	2.3	89
	HOMO-1 → LUMO+3			9
5	HOMO → LUMO	820	1.4	93
	HOMO → LUMO+2	551	2.4	84
	HOMO-1 → LUMO+3			13

Table 5.3 and Figure 5.9 show the electron transitions within the dye molecules. Again, the transitions are similar to the previous cases; two strong peaks are observed in Figure 5.9. The strongest transition is from HOMO to LUMO+2 and the second-strongest transition is from HOMO to LUMO. Unlike the previous cases, all excitations happen inside the thiophene chain. Therefore, the transfer of electrons to the possible surface is blocked.

Again, the 0 model has a stronger transition from HOMO to LUMO+1 than from HOMO to LUMO+2. As explained in chapter 5.1.1, this can be due to the chosen functional and CAM-B3LYP can provide additional information. From now on, any non-typical transitions are expected to happen due to the chosen functional.

In conclusion, the greatest impact of methyl group is for the removed localization of LUMO from the anchor. Since the orbitals are not localized on the anchoring group, it can lengthen the lifetime of the electron–hole pair and create a positive impact on the CT reactions. The minor effect is on the energy level of the LUMO. Otherwise, the energy level saturation and transition energy are similar with the results of vinylene group.

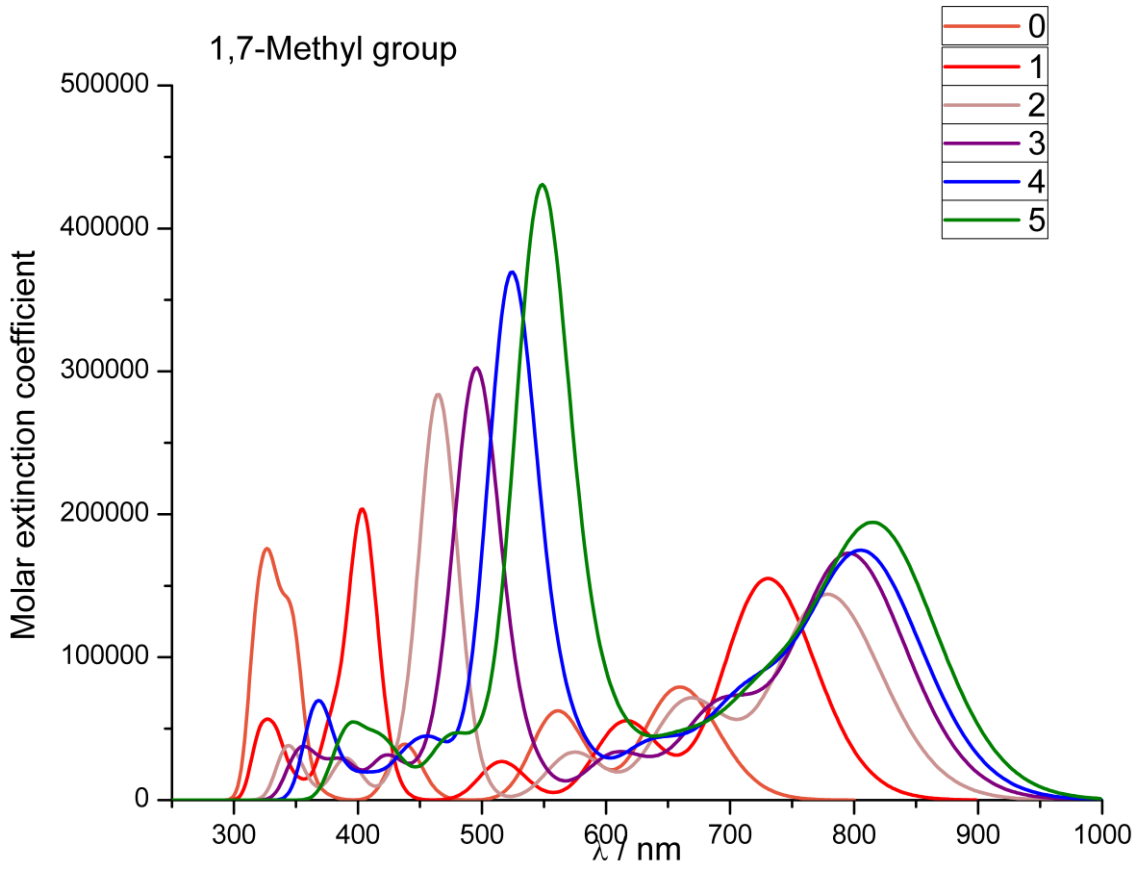

FIGURE 5.9 Simulated UV-Vis of the BODIPY with methyl groups and with different chain lengths.

5.1.4 Without a donor group

The last difference is in the absence of the donor group, TPA. Again, the energy levels are shown in Figure 5.10, the localization of orbitals is depicted in Figure 5.11, and UV-vis spectrum in presented in Figure 5.12 alongside the electron transitions in the Table 5.4. The model for the molecules was provided in Figure 3.6c. The anchoring group is cyanoacrylic acid.

As in previous cases, except in the case of the methyl group, the energy levels are converged (Figure 5.10) as follows: -2.40 eV, -3.41 eV, and -5.09 eV for LUMO+2, LUMO, and HOMO, respectively. It is immediately noted that the energy of the HOMO level is converged lower in energy than in the previous cases. The low saturation energy of HOMO is explained due to the absence of the TPA unit. In previous cases, since

the HOMO is partially localized on the TPA unit, it remains fixed. In the present case, the localization of the HOMO orbital has changed; thus, its (saturation) energy has changed as well. However, LUMO+2 and LUMO have similar values of energy in comparison to the previous cases. The LUMO+2 and LUMO remain similar by the shape compared to the previous cases.

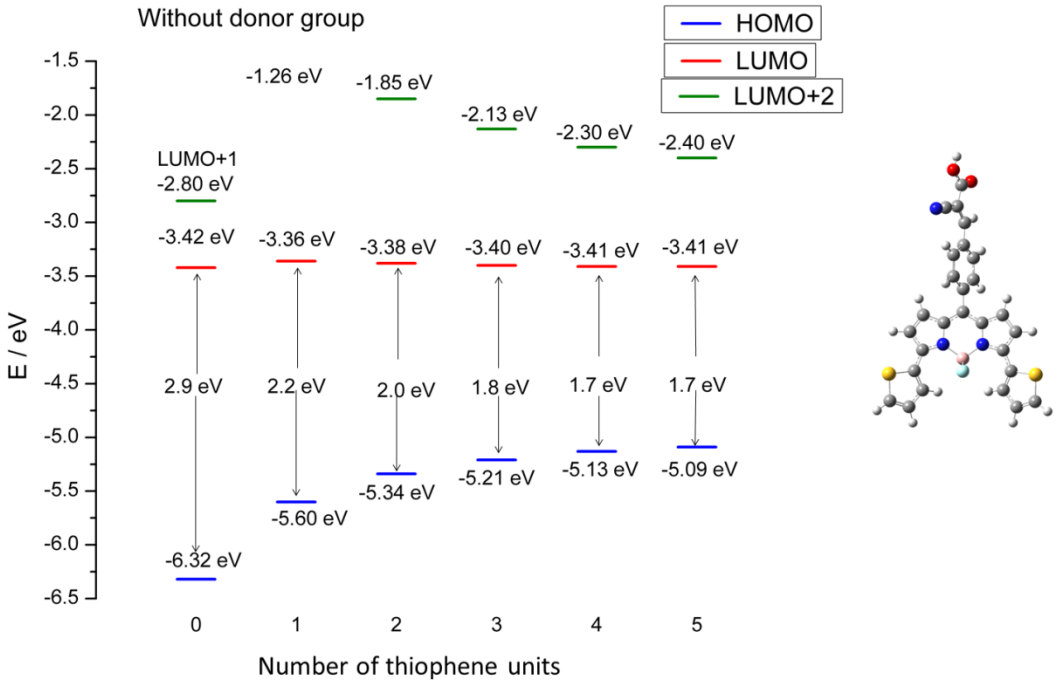

FIGURE 5.10 The energy levels of BODIPY derivatives without the TPA moiety (donor). The chain increases from left to right and the number of thiophene units is shown above the molecules. The orbitals are arranged up to down, LUMO+2, LUMO, and HOMO. The number below the dye molecules is the energy of the orbital. For model 0, the LUMO+1 is shown instead of LUMO+2, as it is more likely that the electron is transported on LUMO+1 than LUMO+2.

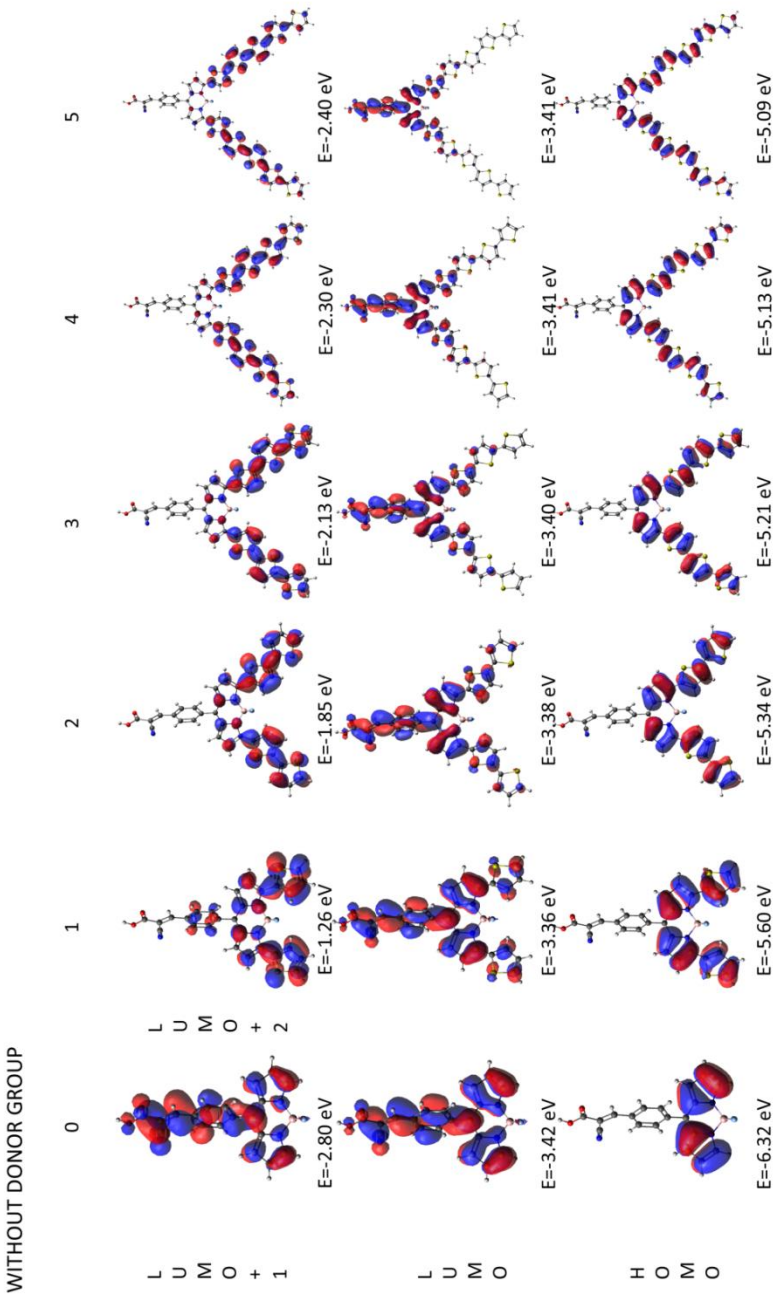

FIGURE 5.11 BODIPY derivatives without the TPA moiety (donor). The chain increases from left to right and the number of thiophene units is shown above the molecules. The orbitals are arranged up to down, LUMO+2, LUMO, and HOMO, except for molecule 0, as the LUMO+1 presented. The table 5.4 indicates that it has the strongest excitation, so it is shown instead of LUMO+2. The number below the dye molecules is the energy of the orbital.

TABLE 5.4. Transitions of BODIPY derivatives without the TPA moiety (donor), types of the strongest excitation, corresponding absorption wavelengths (λ), oscillator strengths (f), and percentage of the contributing orbitals (%).

Model	Orbital	λ / nm	f-value	%
0	HOMO-1 → LUMO	373	0.6	97
	HOMO-1 → LUMO+1	308	0.5	92
1	HOMO-1 → LUMO	425	0.7	97
	HOMO → LUMO+2	312	0.7	70
	HOMO-4 → LUMO+1			14
	HOMO → LUMO+3			7
2	HOMO → LUMO	719	0.7	100
	HOMO → LUMO+2	395	1.1	81
	HOMO-3 → LUMO			12
3	HOMO → LUMO	792	0.9	100
	HOMO → LUMO+2	447	1.4	93
4	HOMO → LUMO	841	1.1	99
	HOMO → LUMO+2	490	1.5	95
5	HOMO → LUMO	872	1.1	99
	HOMO → LUMO+2	519	2.1	91

Table 5.4 shows the excitations within the dye molecules alongside the UV-vis spectrum that is presented in Figure 5.12. Again, they are similar to the previous case because two strong excitations are seen. The first is from HOMO to LUMO+2 (inside the thiophene chain) and the second is from HOMO to LUMO (from the chain to the anchoring group). Therefore, the electron transition to the surface is possible because the LUMO orbital is localized on the anchoring group (Figure 5.11).

To summarize, the greatest impact of the absence of TPA is the low orbital energy of HOMO. However, the transition energies are similar to the results of the vinylene group. Therefore, the TPA can be removed to reduce the energy of HOMO and LUMO, which can be useful for the p-type dye molecules where the HOMO's low energy is advantageous. In addition, the removal of the TPA is not necessary for BODIPY because it does not otherwise improve its properties.

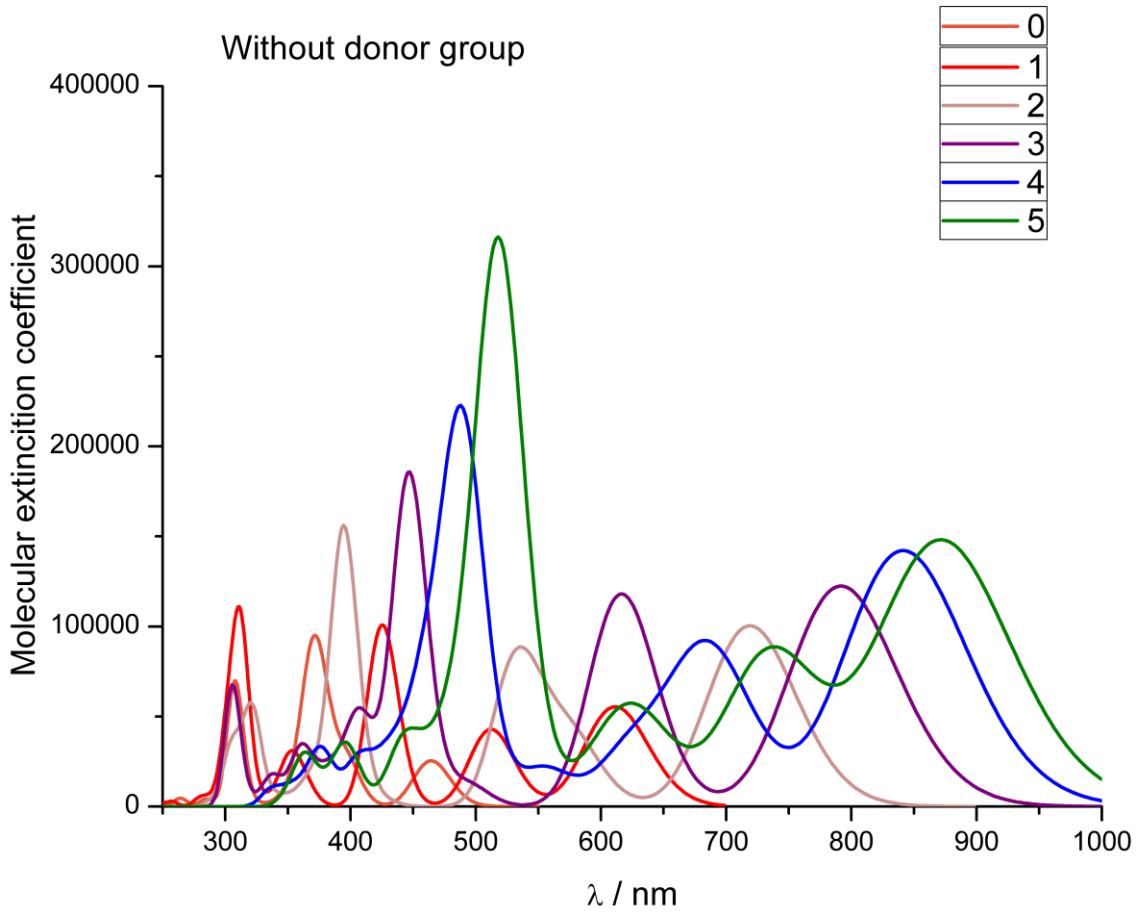

FIGURE 5.12 Simulated UV-Vis of the BODIPY derivatives without the TPA moiety (donor).

5.1.5 Summary

The results of BODIPY show various useful changes in the localization of orbitals, namely LUMO, and the energy level saturation. First, the anchoring group affected the localization of LUMO by removing it from the anchoring group. The character of the anchoring group can also be used to control the electron transfer. CARB drew the electron density on the anchoring group and PHOS pushed it away from the anchor toward the thiophene chain. Therefore, they could be ideal for the n- and p-type dye molecules, respectively. Second, the methyl groups acted as a steric block for LUMO if it was placed close to the anchoring groups. Therefore, they lengthened the life of the electron–hole pair, which had a positive impact. Finally, the absence of the donor group was the only one that affected the energy level alignment. This arrangement can be used to fix the energy level for certain ranges within DSSCs.

In all cases, a shift to lower frequency and an energy level saturation were observed when the chain had several thiophene units. However, the energy change became smaller when the chain was longer (i.e., the energy was saturated with 3–5 thiophenes). The strongest transitions were from HOMO to LUMO+1 or LUMO+2 (inside donor, TPA+thiophene) and from HOMO to LUMO (from donor to the acceptor, thiophene+anchoring group), which is desirable for n-type dye molecules.

As stated in the beginning, the screening of BODIPY derivatives was done at the request of the experimental group [99]. According to these theoretical results, BODIPY with methyl groups and a vinylene group is suggested. The anchoring group remains unchanged (cyanoacrylic acid). The vinylene group is suggested to due to its small, but hopefully stabilized, impact on the structure. The methyl groups are intended to lengthen the charge separation state. The synthesis was recently finished and it was experimentally easier to add the methyl group in positions 2 and 6 instead of 1 and 7. The synthesized molecule was screened according to a higher level of theory to fully explain all electronic properties. These calculations include long-distance CT excitations and range-separated DFT. Since the synthesis recently occurred, the calculations and analysis were in progress while this manuscript was being written, thus, the results are not reported here. It can be said that the mentioned calculations have great importance in understanding the CT properties. In addition, these complete results are expected to be published in a journal in the future.

5.2 Modeling of nickel oxide and titanium dioxide: isolated systems

5.2.1 Nickel oxide

The NiO is studied in order to understand its properties for an isolated surface and to develop a standard reference for the interacting system. When it is known where and how the VBM and CBM are composed, the differences on the surface structure will be visible and can be discussed because of the interaction with the dye molecule. Therefore, the study is focused on the electronic structure. The DOS and band structures of the NiO bulk and the NiO(100) surface are presented in Figures 5.13 and 5.14, respectively. In Figure 5.14, the partial DOS (PDOS) of the 3d orbitals is also visualized for the surface. The model for the calculations is illustrated in Figure 3.9.

According to Figures 5.13 and 5.14, the indirect band gap of the NiO bulk is 4.5 eV and that of surface slab model (Figure 3.9) is 4.0 eV. The DOS (Figures 5.13 and 5.14) demonstrates that the Ni atomic orbitals, which have the e_g and t_{2g} symmetry, are split so that the t_{2g} orbitals are occupied and the e_g orbitals lie in the conduction band. They show that the VBM is constructed of O 2p-orbitals, while the CBM is of Ni 3d-orbitals. When comparing Figures 5.13 and 5.14, there is little difference between the DOS of the bulk and surface: i) Both have a strong density of Ni 3d-orbitals at the CBM and ii) the VBM is constructed of 2p-orbitals of oxygen. The only significant difference is at the very edge of the valence band, where the surface has states localized on the oxygen (band structure, Figure 5.14). [1]

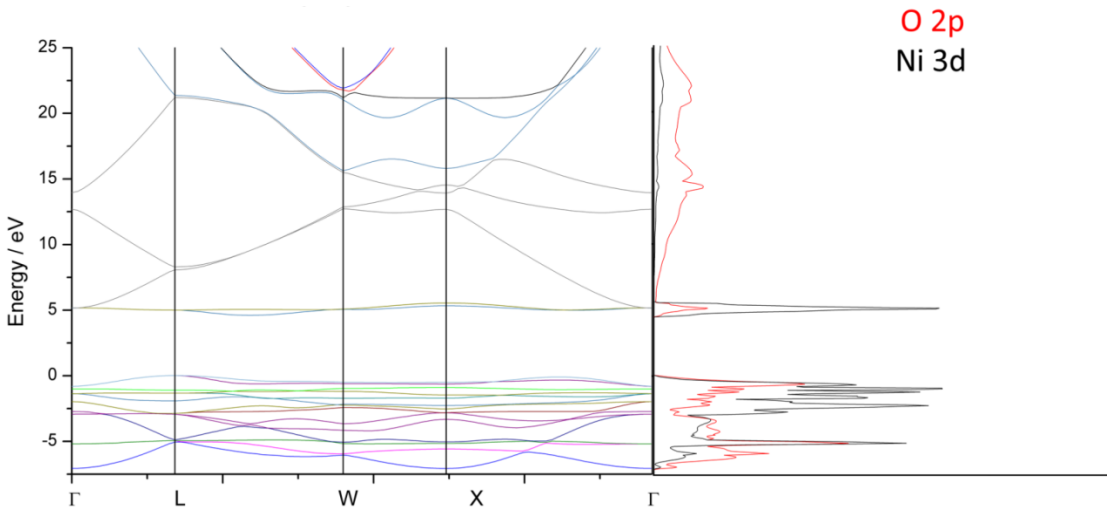

FIGURE 5.13 Band structure (left) and DOS (right) of the NiO bulk.[1]

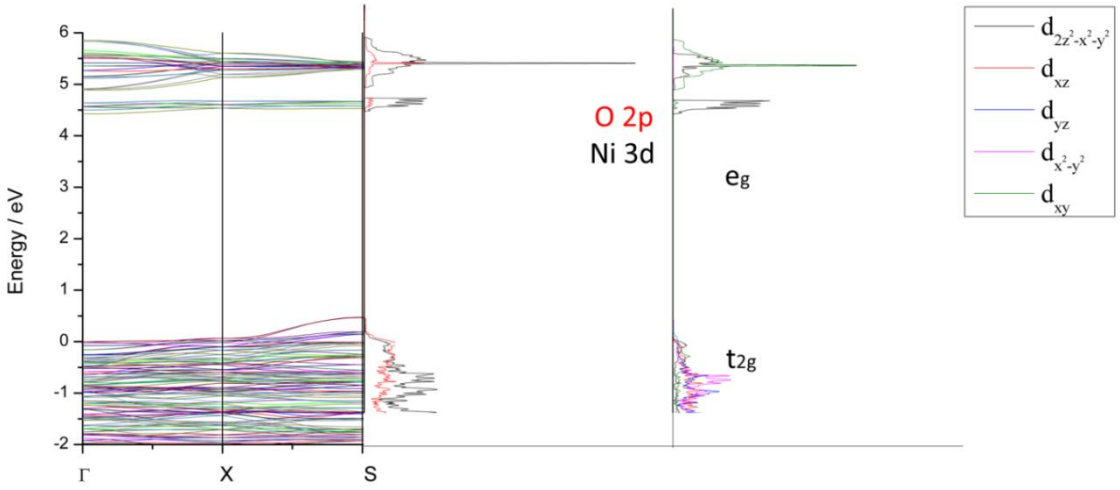

FIGURE 5.14 Band structure (left), DOS (middle), and partial DOS of Ni 3d orbitals (right) on the NiO (100) surface.[1]

From our calculated band energies, the effective masses of charge carriers can be evaluated with this equation:

$$m^* = \frac{\hbar^2}{\frac{d^2E}{dk^2}}\,, \tag{5.1}$$

where m* is the effective mass of the electron, $\hbar$ is Planck's constant divided by 2π, and d^2E/dk^2 is the second derivative of energy with respect to the wave vector k. The m^* is inversely proportional to the hole mobility. To find the second derivative for Equation 5.1, the first derivatives are discretized with three closely spaced equidistant k-points as

$$\frac{dE}{dk} = \frac{\Delta E}{\Delta k} = \frac{E_2 - E_1}{k_2 - k_1} = E_1', \tag{5.2}$$

and

$$\frac{dE}{dk} = \frac{\Delta E}{\Delta k} = \frac{E_3 - E_2}{k_3 - k_2} = E_3', \tag{5.3}$$

Now, the second derivative can be evaluated as

$$\frac{d^2E}{dk^2} = \frac{E_3' - E_1'}{\Delta k} = \frac{E_3 - 2E_2 + E_1}{\Delta k^2}, \tag{5.4}$$

which is the three-point equation. According to Equation 5.4, a substitution of energies around the valence maximum gives

$$\frac{\mathrm{d^2E}}{\mathrm{dk^2}} = \frac{-0.73940 - 2*(-0.73928) + (-0.73946)}{(0.34176 - 0.32277)^2} = -0.80975,$$

which finally gives the electron effective mass

$$\mathrm{m^*} = \frac{1}{-0.80975} \approx -1.2.$$

The Equation 5.1 describes the effective mass of the electron, not the hole, which is being calculated above. However, hole and electron can be treated as equal with opposite properties so the hole's effective mass is of opposite sign, +1.2. All of the values are from our calculations and are given in atomic units (Hartr)ee. The effective mass of the hole in the surface is 0.6. This means that the surface conductivity is higher than the bulk conductivity. Figures 5.13 and 5.14 also show that the conductivity of the hole is highest at the symmetry points of L (½, ½, ½) and S (½,½, 0) in the Brillouin zone for the bulk and surface, respectively. Hence, the conductivity is highest on the surface of the slab.[1]

5.2.2 Titanium dioxide

The second part of the SC surface study focuses on the nitrogen-doped TiO_2(101) anatase surface. It is investigated with various levels of nitrogen dopants, N=0, 3, 5, 7, 9, or 0%, 2%, 3%, 5%, and 6%, respectively (Figure 3.10). It is known that nitrogen is a substitutional impurity in oxygen sites (N_O) and, therefore, increases the hole conductivity. During this part, there is motivation to determine how it affects the TiO_2(101) surface and whether or not it can be used as an electrode inside a p-DSSC when it is doped by nitrogen.

The coordinates (Figure 3.10) that are used as a starting point for the geometry relaxations are provided by Adriano Panepinto [104]. In all cases, the VBM, CBM, band gap, and gap state positions with the pristine surface are compared. Then, the intensity of the possible gap state peaks were investigated and a Mulliken population analysis was performed to see the electronic rearrangement inside the surface. The intensity of the states is related to the height of one peak (marked in Figures, the reference in Figure 5.15) on the CBM that is the same for all of the structures. It is fixed to the value of 1.00 in every separate case. The possible gap state peaks are then normalized according to it. It is expected to see that the intensity and position of the gap states change between various levels of dopants.

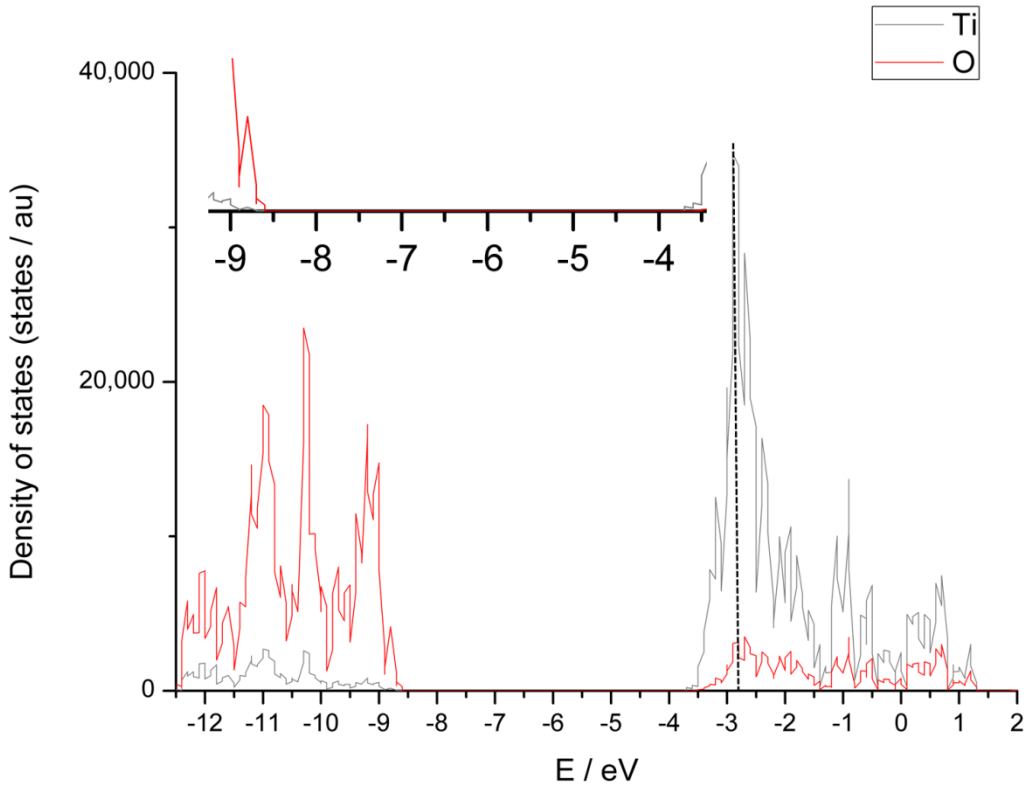

FIGURE 5.15 Partial DOS of the undoped TiO_2(101) surface. The red line shows the states of oxygen and the grey line indicates the states of titanium. The detail is from the VBM region and the dashed line shows the state/peak that will be normalized (the height is set to 1.00) in later cases.

The DOS for the undoped TiO_2(101) surface is shown in Figure 5.15 and the structure of the model was previously presented in Figure 3.10. With regard to the energy level alignment, Figure 5.15 shows that the CBM is -3.75 eV and the VBM is -8.61 eV; hence, the band gap is 4.86 eV. The corresponding experimental values are -3.76 eV, -6.96 eV, and 3.2 eV. [88, 118] CBM is in very good agreement, but the VBM is lower in energy; thus, the band gap is over estimated in comparison to the experiments. This overestimation is typical for hybrid functionals, yet it is unusual for GGA methods, for example. The more detailed information of the methodology was presented earlier in chapter 4.2. Now that the reference values are known for the energy levels, the dopants are introduced inside the structure.

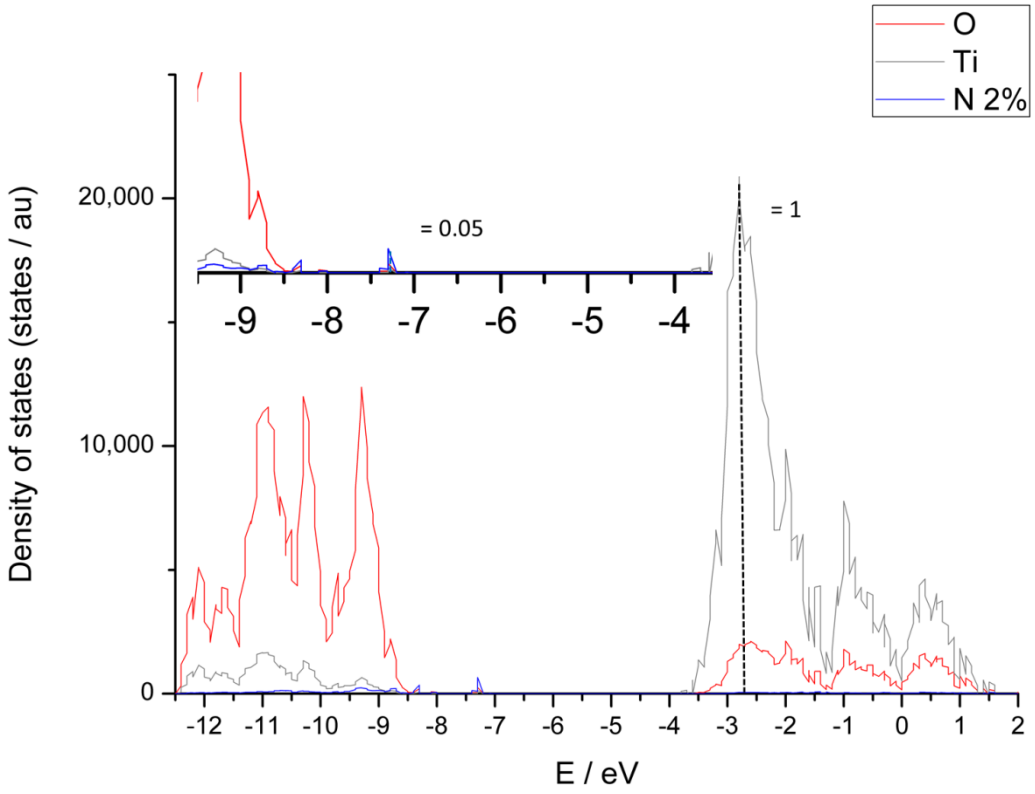

FIGURE 5.16 Partial DOS of the undoped TiO_2(101) surface. The red line shows the states of oxygen, the grey line indicates the states of titanium, and blue line portrays the states of nitrogen. The detail is from the VBM region and the dashed line shows the peak that will be normalized (the height is set to 1.00). In comparison, the state of the nitrogen has a height of 0.05.

The first case is with the doping of 2%, $Ti_{48}O_{93}N_3$ (Figure 3.10). As explained earlier, the replaced oxygens are chosen randomly and optimized. The replacement does not distort the lattice structure as the bond lengths of nitrogens in exact positions are unchanged compared to oxygen. The same phenomenon is recorded for all of the cases, so it will not be discussed in later cases.

The energy levels are investigated in comparison with the undoped surface. The CBM has the energy of -3.77 eV, the VBM -8.64 eV, and the band gap is 4.87 eV. When comparing the values in the previous case, it is noted that the values are at the same magnitude. Also, the electronic structure is very similar by shape as the DOS is almost unchanged (Figures 5.15 and 5.16). This is proven by the similar shape of the DOS and the investigation of the contribution of the atoms (VB is focused on oxygens and

CB on the titanium). The visible change between the undoped and doped DOS is the gap state, which is localized on nitrogens. The position of this gap state is -7.2 eV and its intensity, as related to the fixed peak, is 0.05.

The calculations indicate that the highest occupied state is below -7.2 eV, so the states of the nitrogen are occupied. This finding means that if the hole is injected to the surface, it is transferred on the VBM; hence, gap states are potential traps. In fact, nitrogen has one electron less than oxygen and, therefore, it can occupy the electron on 2p-orbitals. In this case, the electrons from the gap states can be transferred to the holes of TiO_2 surface and, thus, act like trap states.

Mulliken population analysis is performed to investigate the CT inside the TiO_2 surface. The analysis shows that i) all of the nitrogens receive ~1.00 e^-, while ii) the surrounding titanium atoms equally lose electrons. However, when the electron loss of titanium atoms is compared to the case of an undoped surface, the titanium atoms lose more electrons to the oxygen (0.02–0.04 difference). This is because the oxygen is more electronegative, which means that it draws electrons stronger to itself than does nitrogen.

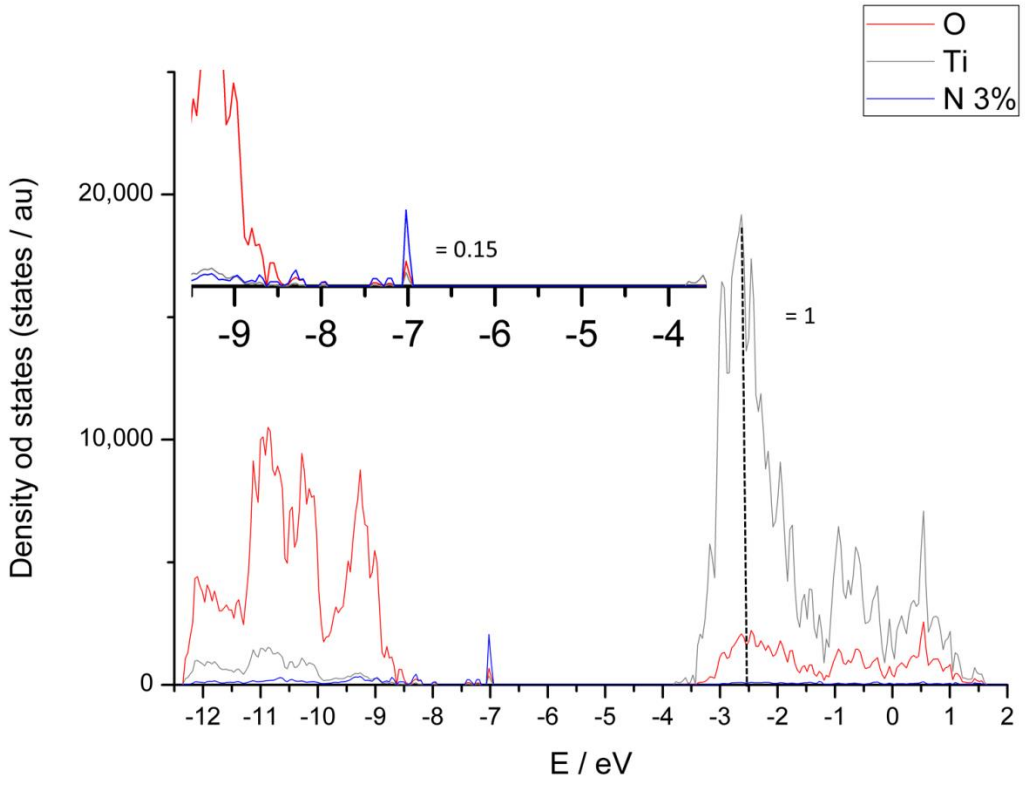

FIGURE 5.17 The partial DOS of the undoped TiO_2(101) surface. The red line shows the states of oxygen, the grey line indicates the states of titanium, and blue line represents the states of nitrogen. The detail is from the VBM region and the dashed line shows the peak that will be normalized (the height is set to 1.00). In comparison, the state of the nitrogen has a height of 0.15.

In the second case, five (5) oxygens are replaced ($Ti_{48}O_{91}N_5$) by nitrogen; that is, the surface has a doping rate of 3%. The structure was previously shown in Figure 3.10 and the partial DOS is seen in Figure 5.17. In comparison with the pristine TiO_2 surface, the partial DOS is, again, similar in terms of the shape and the construction of the states (CB is focused on the titanium and the VB on the oxygen). In addition, CBM has the value of -3.77 eV and VBM of -8.67 eV; hence, the band gap is 4.90 eV. It can be stated that, so far, the level of doping makes no difference for the electronic structure. The Mulliken population analysis shows results that are similar to those of the previous case: i) The nitrogens receive ~1.00 electron and ii) the surrounding titanium loses less electrons than the pristine surface. Due to the similar results that are found within the Mulliken population analysis, it will only presented in the following cases if it provides interesting information.

As in the previous case, the highest occupied (-7.2 eV) state in this case is also focused on the nitrogen inside of the band gap. As explained earlier, this creates the traps' states inside the p-type DSSC. It is also intriguing that the gap states, as well as the states of the TiO_2 surface, is practically unchanged so far. However, the intensity of the gap states is changed (Figure 5.17) from 0.05 to 0.15. It is bigger than it was in the previous case, which is logical as the level of the doping is higher (2% *vs.* 3%) in comparison to the previous case. However, the ratio is not equal (2:3 = 0.67 ≠ 0.33 = 0.05:0.15). Given these numbers, it can be said that the one peak is not presenting one specific nitrogen, but one or more within the structure.

In the third case, seven (7) oxygens ($Ti_{48}O_{89}N_7$) are replaced by the nitrogens according to Figure 3.10. The level of doping is now 5% and its partial DOS is presented in Figure 5.18. Now a clear difference is seen in the DOS as three gap states are appeared instead of one. Their intensities are 0.13, 0.10, and 0.08, from left to right. The sum of the intensities (0.31) is higher than it was in the previous case, which is explained just as it was before: There are more nitrogens, so there is a higher intensity and the states are more localized on the nitrogens. In contrast to the previous cases, now the states are separable as a single peak is not seen in the partial DOS. The gap state that has the highest energy is practically unchanged and two other states are below this state.

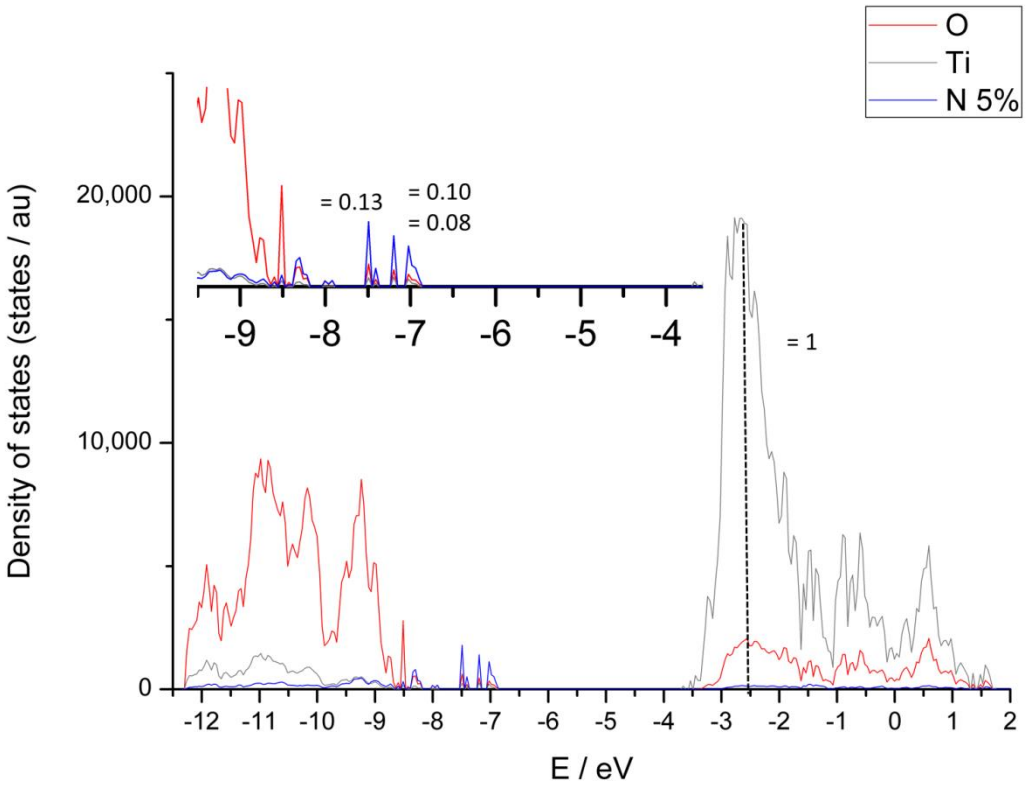

FIGURE 5.18 Partial DOS of undoped TiO_2(101) surface. The red line shows the states of oxygen, the grey line indicates the states of titanium, and blue line shows the states of nitrogen. The detail is from the VBM region and the dashed line shows the peak that will be normalized (the height is set to 1.00). In comparison, the states of the nitrogen have heights of 0.13, 0.10, and 0.08, from left to right.

In contrast, the energy levels have changed in comparison to the previous cases. The CBM is -3.71 eV, VBM is -8.56 eV, and the band gap is 4.85 eV. In this case, the energy levels have increased by approximately 0.1 eV. However, the band gap is unchanged. The highest occupied state is -7.1 eV. Again, this is similar to the previous cases where the nitrogen states are occupied. Therefore, these states cannot conduct holes inside the surface. Even though the results are similar to the previous cases, it is still intriguing to note that the energy levels have increased. Because the only difference between the systems is in the amount of nitrogen (i.e., geometry), it is just assumed that it is the cause of the changes in the structure.

Finally, 9 oxygens were replaced by the nitrogens to create a doping level of 6%. The structure ($Ti_{48}O_{87}N_9$) is presented in the Figure 3.10 and the DOS in Figure 5.19. It shows that the CBM is -3.69 eV and VBM is -8.66 eV; hence, the band gap is 4.97 eV.

Surprisingly, this structure is similar to the cases of 2% and 3% instead of the previous case (5%) in comparison to the energy levels. Then again, the structure of the band gap is similar to the previous case because Figure 5.19 reports two gap states with intensities of 0.08 and 0.16 (sum 0.24). The sum is higher than in the two first cases, but smaller than in the previous case. This finding confirms that the differences are due to the (structural) geometry inside the surface. Finally, the highest occupied state is -7.1 eV and, according to Figure 5.19, it is located on the nitrogens. Therefore, the electron's conductivity properties do not change with regard to the amount of nitrogen.

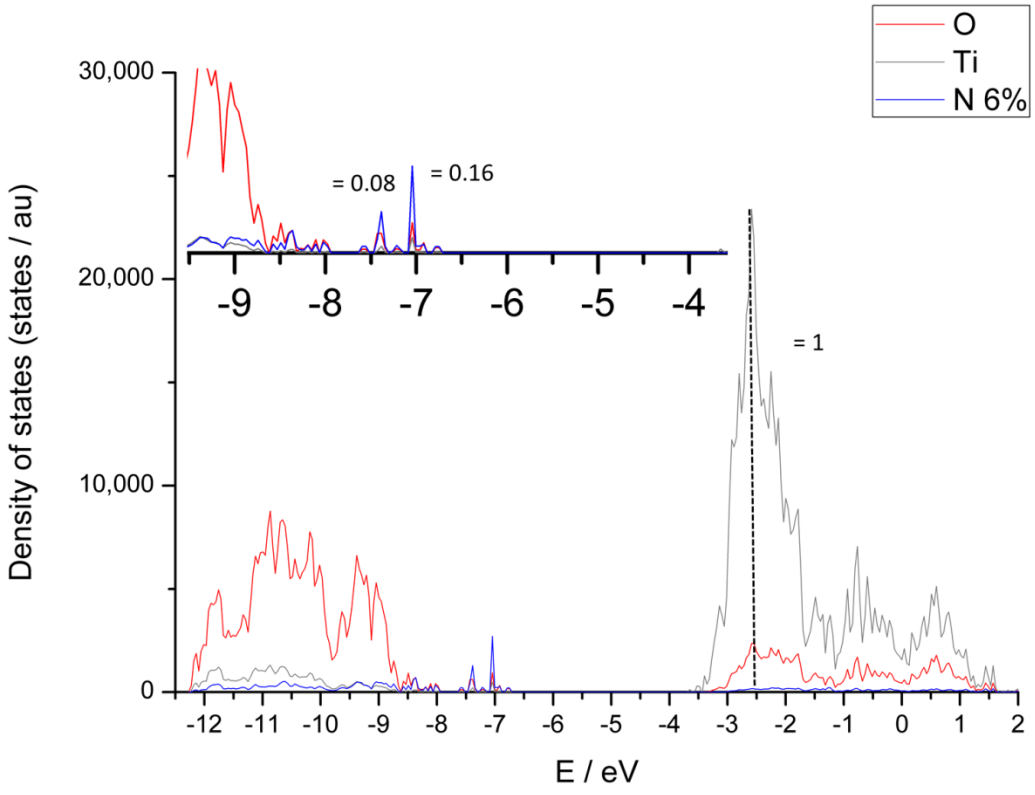

FIGURE 5.19 Partial DOS of undoped TiO_2(101) surface. The red line shows the states of oxygen, the grey line indicates the states of titanium, and the blue line shows the states of nitrogen. The detail is from the region of VBM and the dashed line shows the peak that will be normalized (the height is set to 1.00). In comparison, the states of the nitrogen have heights of 0.08 and 0.16, from left to right.

TABLE 5.5 The VBM, CBM, WF_L, WF_R, band gap, and electrostatic potential for TiO_2 with various levels of nitrogen (N_O) dopants. All values are in eV.

N_O / %	E_g / eV	VBM / eV	CBM / eV
0	4.9	-8.6	-3.7
2	4.9	-8.6	-3.8
3	4.9	-8.7	-3.8
5	4.8	-8.6	-3.7
6	5.0	-8.7	-3.7

In conclusion, the level of doping creates a small difference in energy level alignment. The energy levels remain identical (Table 5.5) despite the amount of nitrogens. The most significant differences are seen in the electronic structure inside the band gap. The number of peaks and the intensity are both increased. However, the energetics (levels and band gap) remain similar, except in the case of doping of 5%. Despite the latter, all of the phenomena can be explained in terms of the atomic character of the nitrogen. Nitrogen has one less electron, so it is less electronegative than oxygen. This weakens the hole conductivity properties through the trap states. In this case, the aim was not reached as the gap states are possible trap states for DSSC. Thus, TiO_2 with N is not an ideal electrode for p-DSSC and the aim was not achieved.

5.3 Modeling of perylene monoimide derivatives: isolated and interacting cases

This section provides the results from interacting systems of PMI dye molecules and information to understand if PMIs are interacting with NiO(100) surface. Also, the physics and chemistry behind the interactions are presented. Part of the study and explanations are shown in the chapter 5.4 where different anchoring groups in contact with NiO(100) are presented.

The molecular orbitals and transitions of the free dye molecules derived from PMI (Figure 3.7) were examined to gain understanding of the intramolecular excitations for the CT processes. In order to obtain the information, DFT and TDDFT calculations were performed. The electron transitions are depicted by using molecular orbital images in Figures 5.20–22 alongside the transitions, which are presented in Table 5.6.

The transitions are typical for the D–A dye molecules: The first excitations are from HOMO to LUMO+1 (inside the donor). The UV-Vis spectra of the dye molecules are presented in Figure 5.20 alongside the corresponding excitations, which are presented in Table 5.6. The strongest transitions take place in all dyes at 490-535 nm. TPA–PMI has another strong transition at 395 nm, which is at the border of the UV light. [1] The absorptions and excitations support the previous spectroscopic studies [53]: The first excitation takes place inside the donor of the p-type D-A dye; that is, inside TPA in TPA–PMI and inside PMI within the rest of cases. Further, the CT reaction is from the donor (LUMO+1) to the acceptor (LUMO) moiety of the dye molecule within all studied molecules. Only TPA–PMI has one strong transition solely inside the acceptor, which is from HOMO-1 to LUMO. [1] In this case, the electron is already far from the surface and it is able to transfer directly to the electrolyte. However, the excited state can relax back to the ground state. If the relaxation is fast, then it prevents the electron from transferring to the electrolyte and there is no hole in the donor moiety that can be transferred to the SC.

The energy level alignment, DOS, was also studied and is presented in Figure 5.23. The calculated HOMO–LUMO gaps of the studied dye molecules are 2.5 eV for TPA–PMI, 1.9 eV for PMI–NDI, 1.8 eV for PMI–PhNDI, and 1.9 eV for PMI–PhC60.[1]

TABLE 5.6 The excitations of the free dye molecules, type of orbitals involved in the strongest electron transitions and the corresponding absorption wavelengths (λ), oscillator strengths (f), and the percentages of the contributing orbitals (%).[1]

Molecule	**Excitation**	**Orbital**	***λ* / nm**	***f***	**%**
TPA–PMI					
	1	HOMO-2 → LUMO	568	0.1	3
		HOMO → LUMO			96
	2	HOMO-1 → LUMO	493	1.0	98
	6	HOMO → LUMO+1	395	1.1	95
	7	HOMO → LUMO+2	375	0.2	96
PMI–NDI					
	1	HOMO → LUMO	768	0.0	100
	2	HOMO → LUMO+1	528	0.7	99
	5	HOMO-1 → LUMO+1	430	0.1	97
	7	HOMO-2 → LUMO+1	392	0.1	98
	14	HOMO-6 → LUMO	365	0.2	80
PMI–PhNDI					
	1	HOMO → LUMO	771	0.0	100
	2	HOMO → LUMO+1	532	0.7	99
	6	HOMO-1 →LUMO+1	424	0.1	97
	10	HOMO-1 → LUMO+1	380	0.1	94
	15	HOMO-3 → LUMO+1	368	0.1	24
		HOMO → LUMO+3			38
	16	HOMO-9 → LUMO	365	0.3	91
PMI–PhC60					
	1	HOMO-1 → LUMO	982	0.0	5
		HOMO → LUMO			94
	10	HOMO-5 → LUMO	596	<0.1	89
	17	HOMO-1 → LUMO+3	534	0.7	95

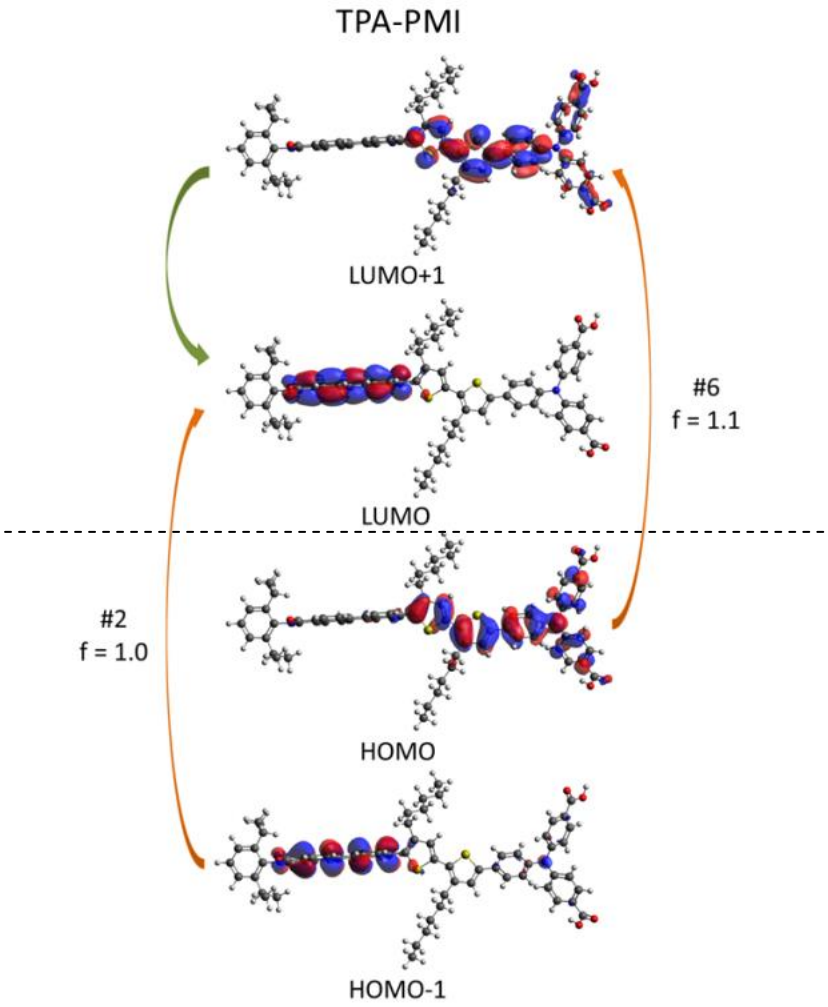

FIGURE 5.20 The orbitals and transitions of TPA–PMI. The orange and green arrows represent an electron's excitations and relaxation, respectively. The corresponding transitions are presented in Table 5.5. The unoccupied states are above the dashed line and the occupied states are below it. [1]

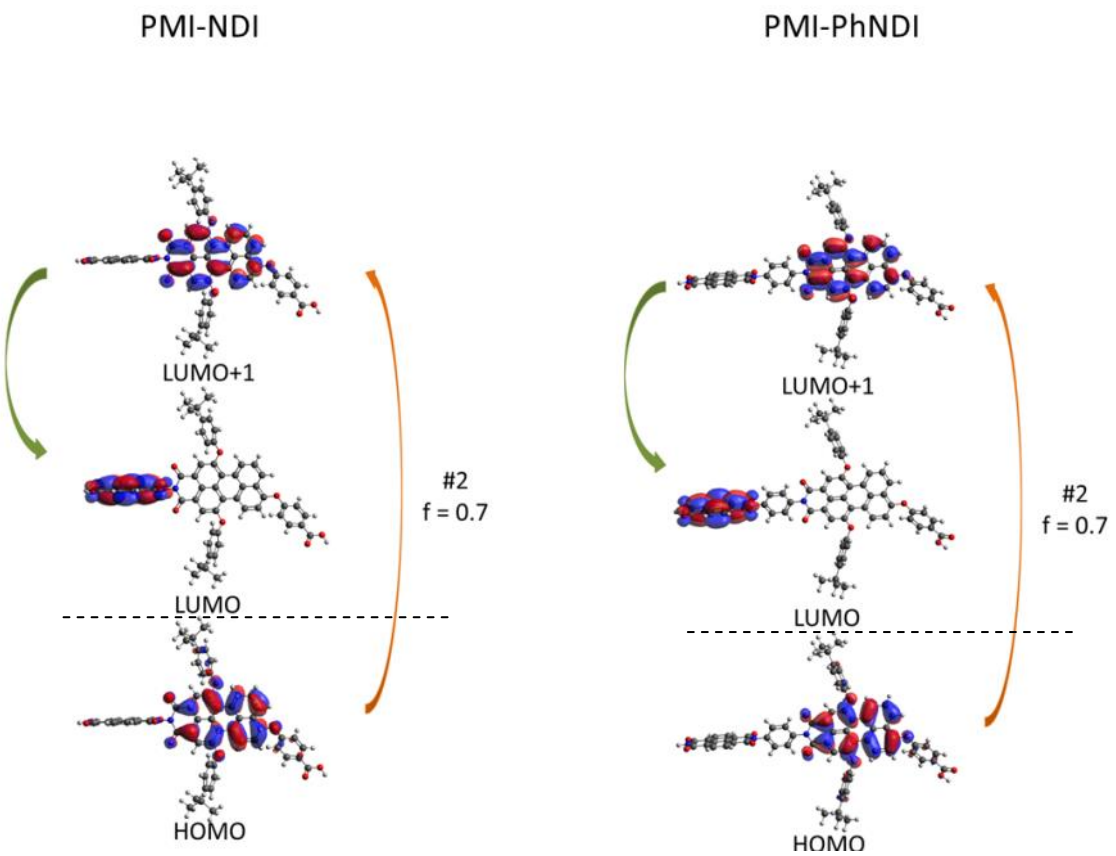

FIGURE 5.21 The orbitals and transitions of PMI–NDI (left) and PMI–PhNDI (right). The orange arrows represent the excitations of an electron, and the green arrow signifies its relaxation. The corresponding transitions are presented in Table 5.5. Again, the dashed line separates the unoccupied states from the occupied states. [1]

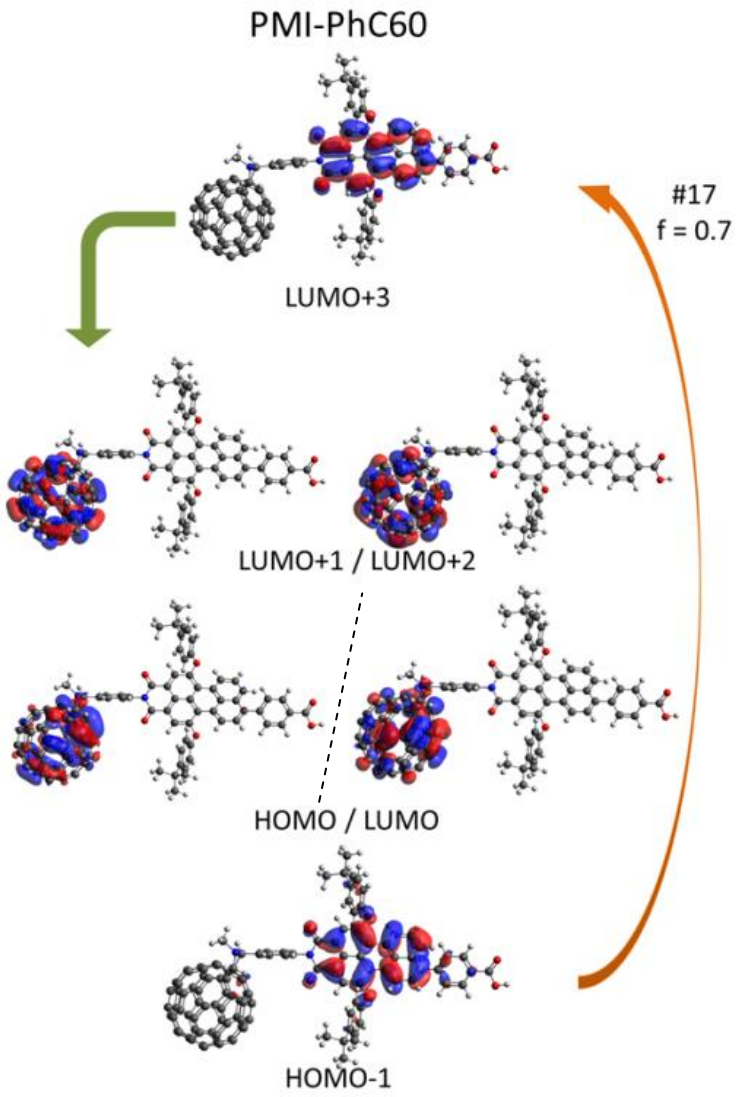

FIGURE 5.22 The orbitals and transitions of PMI–PhC60. The orange arrows present the excitations of an electron, and the green arrow signifies its relaxation. The corresponding transitions are presented in Table 5.5. Again, the dashed line separates the unoccupied states from the occupied states.

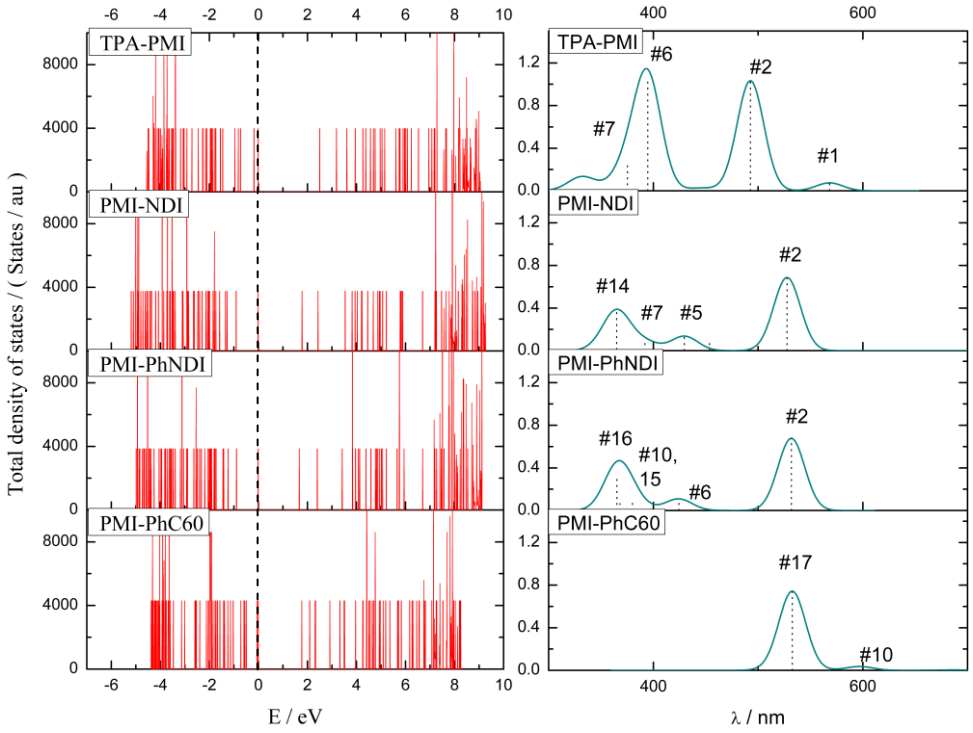

FIGURE 5.23 On the left are the total DOSs (orbital energies) for periodic dye TPA–PMI, PMI–NDI, PMI–PhNDI, and PMI–PhC60 molecules. The zero is set at the HOMO level of each molecule. Because the models are molecules in PBC, a set of sharp peaks are observed. Higher peaks are due to several orbitals being close in energy. On the right is the simulated UV–Visible spectra PMI derivatives and the strongest excitations. [1]

The geometries of the combined dye-surface models were previously in Figure 3.11. The geometries of the dyes TPA–PMI and PMI–NDI on the NiO(100) surface are relaxed. The shortest distance between two dye molecules is 4.5 Å, which allows the neighboring molecules to interact and may affect the adsorption energies and explain the differences between TPA–PMI and PMI–NDI. As shown earlier, TPA–PMI (Figure 3.11) is able to chemisorb either via one or two carboxylic acid groups and prefers an upright position on the surface, while PMI–NDI tilts toward the NiO(100) surface. [1] The adsorption energies are given in Table 5.6. The geometries of PMI–PhNDI and PMI–PhC60 were more challenging to optimize because of their structures (i.e., the phenyl linker between the donor and the acceptor and the large fullerene acceptor). However, some features can be predicted from the calculated results of PMI–NDI on the NiO surface. The prediction is justified because of the same anchoring group and donor moiety in PMI–NDI and PMI–PhNDI. Moreover, the carboxyphenyl anchoring group in PMI–PhC60 is more rigid than the carboxyphenoxy anchor group in PMI–NDI.

This is justifiable as well because the distance between the donor moiety and the NiO surface is comparable in each of these systems. The tilting is seen for the partially relaxed structure of PMI–PhNDI, which is well founded because the angle is expected to be about the same due to the sp^3 hybridization of the ether oxygen in the carboxyphenoxy anchor. In the interacting system of PMI–PhC60, the phenyl group of the anchoring group, which is directly bound to the PMI donor, causes the structure to be straight as a result of the sp^2 hybridized aromatic carbon atoms. [1]

Within these four interacting systems, it is possible for hydrogen bonds to occur in two ways: i) the hydrogen from the carboxyl group is adsorbed on the surface near the dye molecule when the hydrogen bond is between hydrogen and carboxyl oxygen, C-O(-Ni)•••H-O). However, in this case, the hydrogen bond is possible only if the hydrogen will remain near the adsorbed dye molecule. In these calculations, we chose to place hydrogen next to the molecule and a hydrogen bond of 2.3 Å is observed. ii) The second case applies only to TPA–PMI, which has two anchoring groups and one of them is in “the air” due to the tilted orientation. It is possible to form the hydrogen bond between the carboxyl oxygen and the hexyl group (C-O•••H-C). The distance of this hydrogen bond is 3.1 Å.[1]

TABLE 5.7 Adsorption energies (in eV) for models TPA–PMI-a, TPA–PMI-b, and PMI–NDI and HOMO–LUMO gaps (eV) of free, periodic, and surface dye models.[1]

	TPA–PMI		**PMI–NDI**	**PMI–PhNDI**	**PMI–PhC60**
	a	**b**			
Adsorption energy	-4.1	-2.8	-1.3	N/A	N/A
HOMO–LUMO gap (free)	2.5		1.9	1.8	1.9
HOMO–LUMO gap (periodic)	2.5		1.8	1.7	1.8
HOMO–LUMO gap (surface)	2.5	2.4	1.7	N/A	N/A

The DOSs and the band structures (Figures 5.24–5.26) were calculated for chemisorbed TPA–PMI and PMI–NDI on the four-layer-thick NiO(100), 8x8 surface-slab model. The band gaps of these combined systems are due to the frontier orbitals of the dyes being 2.5 eV for TPA–PMI-a, 2.4 eV for TPA–PMI-b, and 1.7 eV for PMI–NDI. [1] These findings are relatively close to the calculated HOMO–LUMO gaps of the free and periodical models (Table 5.7). TPA-PMI has exactly the same HOMO-LUMO gap and others have 0.1 eV decrease between free and periodic models. Due to the small change in energy levels, it can be stated that there is no difference between the free and periodic model. It can be seen that the adsorption lowers the HOMO–LUMO gap by 0.1–0.2 eV. [1] Closer examination of the energy levels of TPA–PMI-b reveals that the HOMO increases 0.1 eV and LUMO+1 decreases 0.5 eV due to the binding mode. Moreover, the NiO band gap drops from 4.06 eV to 3.96 eV, if chemisorption takes place through a single anchoring group, and to 3.90 eV if it takes place through two groups. Transitions that are expected according to the study of relaxed, isolated dye molecules for these systems are presented in Figures 5.24–5.26. The calculated effective hole mass, m*, is 0.7 for both TPA–PMI and PMI–NDI on the NiO(100) surface. Because the calculated m* is 1.2 for the NiO bulk and 0.6 for the NiO(100) surface, the surface conductivity for the combined system of PMI–NDI is higher than the bulk conductivity of NiO. [1]

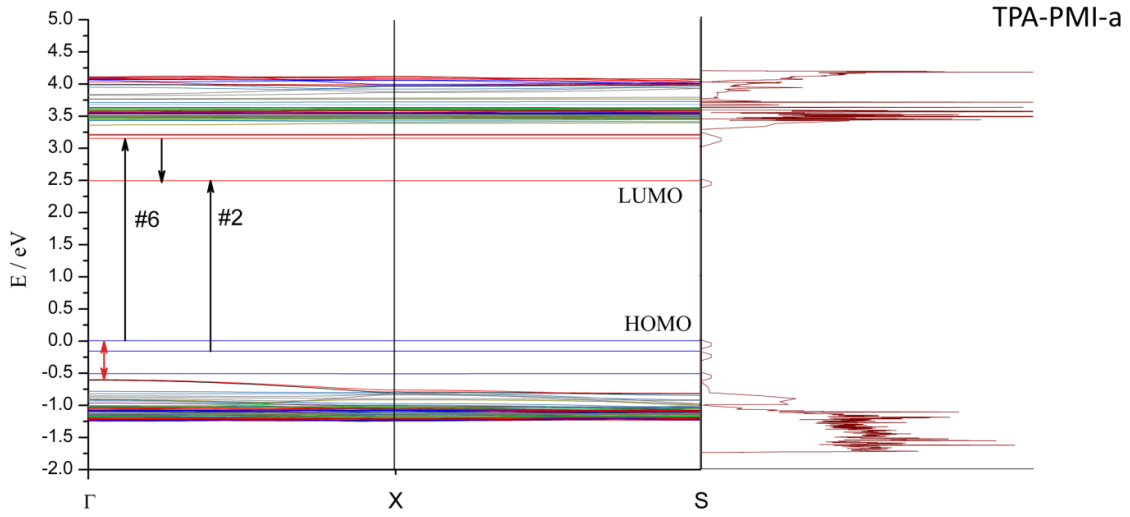

FIGURE 5.24 The DOS and band of the combined systems TPA–PMI-a. The straight lines (blue for occupied, red for unoccupied) are for the molecule and the curved lines signify the surface. The black arrows express the electronic excitations and relaxations in the dye molecule. The red arrow indicates the distance from the VBM of the NiO (100) surface to the HOMO of the dye molecule.[1]

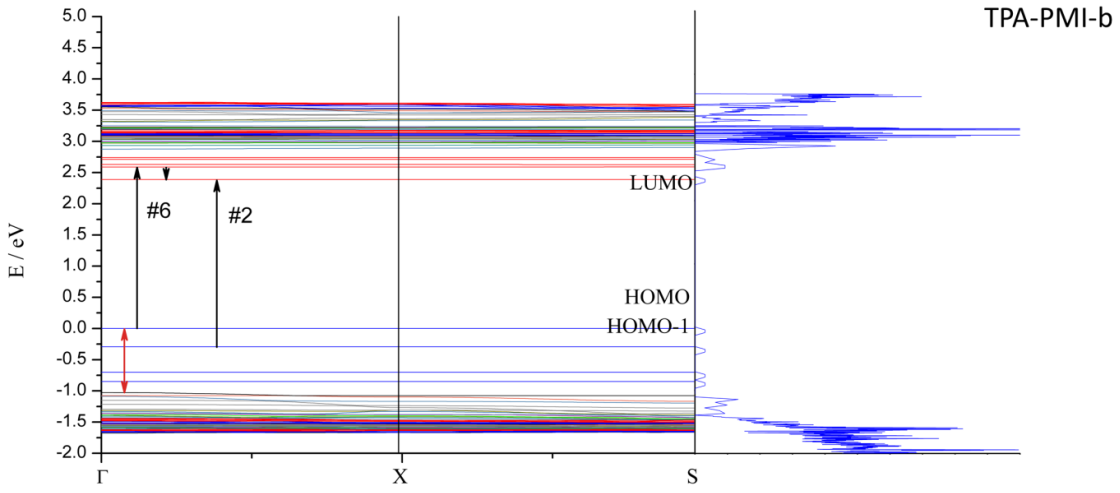

FIGURE 5.25 DOS and band of the combined systems TPA–PMI-b. The straight lines (blue for occupied, red for unoccupied) are for the molecule and the curved lines for the surface. The black arrows express the electronic excitations and relaxations in the dye molecule. The red arrow indicates the distance from the VBM of the NiO (100) surface to the HOMO of the dye molecule.[1]

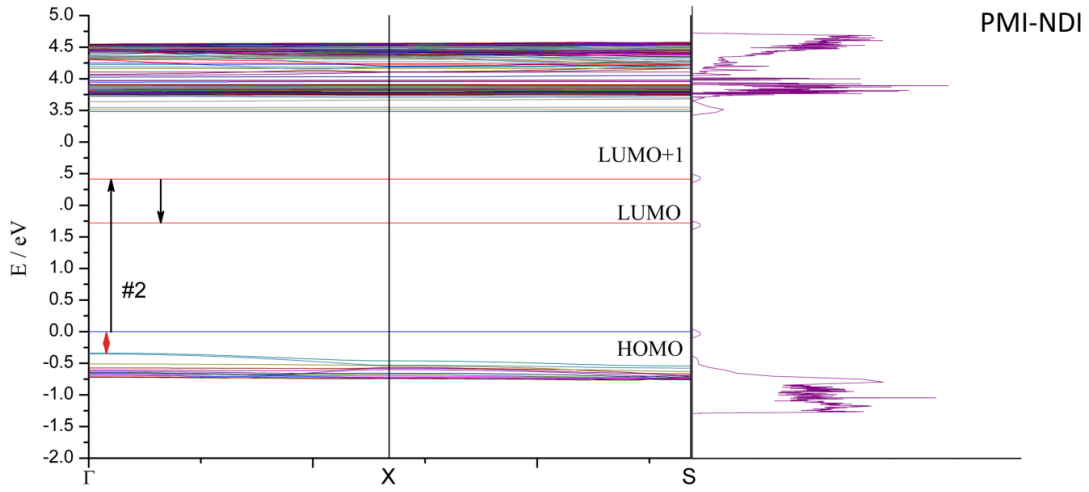

FIGURE 5.26 The DOS and band of the combined systems PMI–NDI. The straight lines (blue for occupied, red for unoccupied) are for the molecule and the curved lines are for the surface. The black arrows express the electronic excitations and relaxations in the dye molecule. The red arrow indicates the distance from the VBM of the NiO (100) surface to the HOMO of the dye molecule.[1]

In the DOS and band calculations, the band gaps of the combined systems of PMI–PhNDI and PMI–PhC60 were not opening properly with the functional and basis sets that were applied despite the usage of the gap widening tools that were described in chapter 4. Thus, a proper description of the electronic structures was not obtained. The band structure of the NiO(100) surface remains mostly unchanged, whether or not it is covered with the dye, except for the shift in energy. Another difference is that the dispersion is located on the Γ(0,0,0) point in the combined system and on the S(½,½,0) point when there is no adsorbate on the NiO surface. Since the surface and the dye molecule interact only weakly, it is assumed that the electronic transitions are similar to those predicted by the TDDFT calculations for the isolated dye molecules. [1]

5.3.1 Conclusion

In all band structures, the TPA–PMI and PMI–NDI within the HOMO are located above the VBM of the SC because a perfect NiO model is used instead of p-type NiO with Ni vacancies and high packing of the dye molecule. Both affect the energy level order between the surface and organic layer. Increased NiO p-doping raises the VBM above the dye HOMO level that is needed to drive the holes to the NiO surface. A similar potential drop is needed for electrons to flow from the dye to the electrolyte to complete the charge separation in the dye-semiconductor junction. For this reason, the dye molecules relative to each other can be compared by looking at the energy difference between the NiO VBM and the dye HOMO level. [1]

The calculated HOMO–LUMO gap of TPA–PMI on the NiO (100) surface is 2.5 eV for the single-anchoring model and 2.4 eV for the two-anchoring model. First, the large gap makes the dye TPA–PMI ideal for collecting sunlight in a tandem device. Second, the distance between the HOMO and conduction band is 0.60 eV in TPA–PMI-a and 1.03 eV in TPA–PMI-b. The HOMO–LUMO gap of 1.7 eV that was calculated for PMI–NDI on the NiO (100) surface (Figures 5.21–23) is smaller than that of TPA–PMI, making PMI–NDI less ideal for a p-type dye, and its HOMO is located 0.34 eV above the VBM, which is less than in the case of TPA–PMI. This means that it is located deeper in the valence band in the actual p-NiO and there is more driving force for the CT to the dye. Moreover, PMI–NDI is the smallest dye molecule that was investigated; therefore, all of the structural parts of the combined system (the donor, the acceptor, and the surface) are close together, which may make it easier for the CT from one part to another. [1]

5.4 Modeling trisphenylamine with different anchoring groups: isolated and interacting systems

The aim of this part is to understand the intramolecular interactions when the anchoring group is in contact with the surface. In addition, it is expected to determine guidelines for the electronic properties to suggest new possible anchoring groups. The study with CARB, DIOL, and PYR (Figures 3.8 and 3.12) reveals how they interact on the NiO(100) surface and which anchoring group is the most suitable for the functionality of DSSC.

First, the electronic structure is investigated. For this purpose, the partial DOS is presented and analyzed. The DOS of the isolated and interacting components are compared together to understand the changes due to the interaction. This is followed by the analysis of the electrostatic potential and dipole moment. As explained before and shown in Equation 4.10, the electrostatic potential and dipole moment are directly proportional; hence, only the difference in electrostatic potential is presented and analyzed. The direction of the dipole moment is analyzed through the electrostatic potential and Mulliken population analysis. The results of the NiO surface are analyzed alongside the TPA–PYR. The relaxed geometry refers to an isolated dye molecule in which the coordinates are relaxed to the lowest energy. The twisted geometry is evident within two steps: i) first, the interacting system is relaxed (i.e., the dye molecule is allowed to relax to a new geometry when in contact with NiO); ii) after the geometry is relaxed, the NiO is removed and the received structure of the dye molecule is considered to be twisted (without any hydrogen). For the twisted geometry, a single-point calculation is performed to obtain electronic properties.

It is good to note that in this part, zero is set in a different position. In previous part, the main focus was to analyze if the energy level alignment is favorable (VBM > HOMO), thus VBM was set to zero. In this part, also the change between isolated and interacting systems is analyzed, thus, the zero is set according to the dipole moment (explained later in this chapter). Thus, (absolute values of) energy levels are incomparable between chapters 5.3 and 5.4. The band gaps are comparable.

5.4.1 Nickel oxide and pyridine anchor

NiO was already studied in detail in chapter 5.2. However, the surface model (Figure 3.9) that is used in this study is thinner than it was in the previous chapter. The use of the thinner surface is justified by the test calculations with varied surface sizes, which

showed little difference near the VBM region: i) the shapes are nearly identical and ii) are less than 0.0 eV in energy. In conclusion, the use of a thinner surface is justified. The electronic properties (DOS) are briefly discussed in terms of the change and the variation within the electrostatic potential is set up as a reference.

5.4.1.1 Isolated nickel oxide and pyridine

The NiO(100) surface and its results for an isolated system (electrostatic potential and DOS) are shown in Figure 5.27. For the isolated NiO (the red lines in the figures), it is observed that the electrostatic potential in the vacuum region is the same at both sides of the NiO slab model. This is due to the symmetrical space group (*Fm3m*) of the used slab model. The VBM of the NiO is -4.81 eV, according to Figure 5.27. Even though the main intention is to study the interactions in the chemisorbed system, it is worthwhile to mention that there is a nice accordance with respect to the experimental VBM available from the UPS measurements: -5.4 eV [42] *vs*. -4.81 eV.

The first anchoring group is TPA–PYR and its results for both isolated structures (in comparison to isolated NiO) are illustrated in Figures 5.27 (relaxed geometry) and 5.28 (twisted geometry). In the absence of intermolecular interactions, the isolated NiO and TPA–PYR share the same vacuum energy. Therefore, the electrostatic potential of the dye molecule is aligned in the vacuum of NiO with respect to the potential on the left side of the TPA–PYR (i.e., the level of the anchoring group is set to zero (Figures 5.27 and 5.28, right).

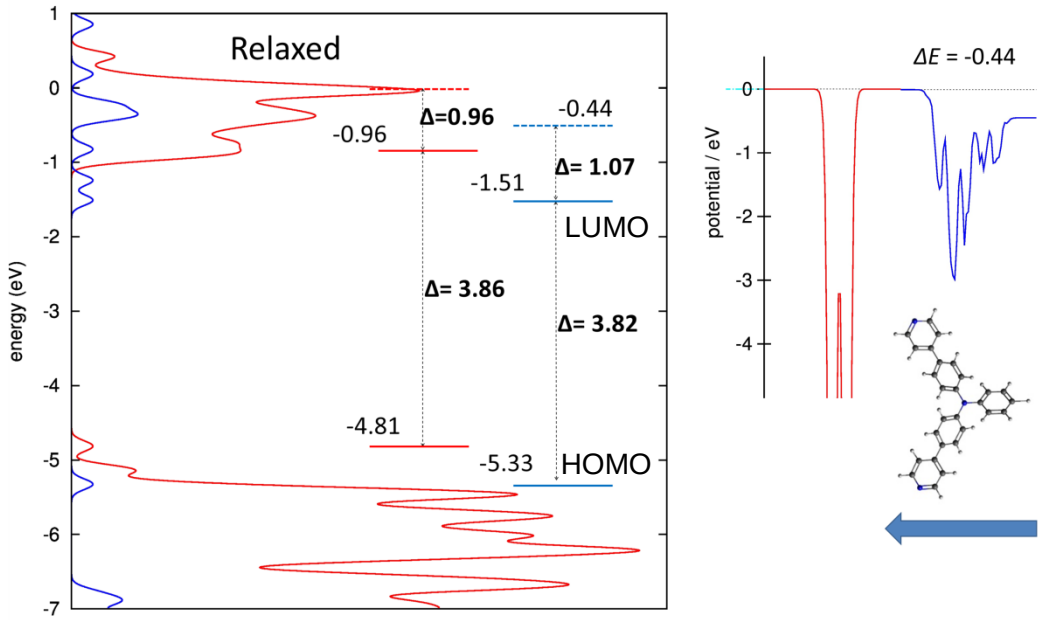

FIGURE 5.27 On the left is the DOS for the relaxed NiO surface (red) and relaxed TPA–PYR (blue); the planar averaged electrostatic potential is on the right. The VBM (solid red), CBM (solid red), HOMO (solid blue), LUMO (solid blue), and the change in the electrostatic potential (dashed red and dashed blue) are marked for the NiO and TPA–PYR. The band gap, the HOMO–LUMO gap, and the difference between the vacuum level and the CBM or LUMO are marked with Δ. In addition, the direction of the dipole moment (the blue arrow) with respect to the change in the electrostatic potential of TPA–PYR is illustrated on the right. All values are in eV.

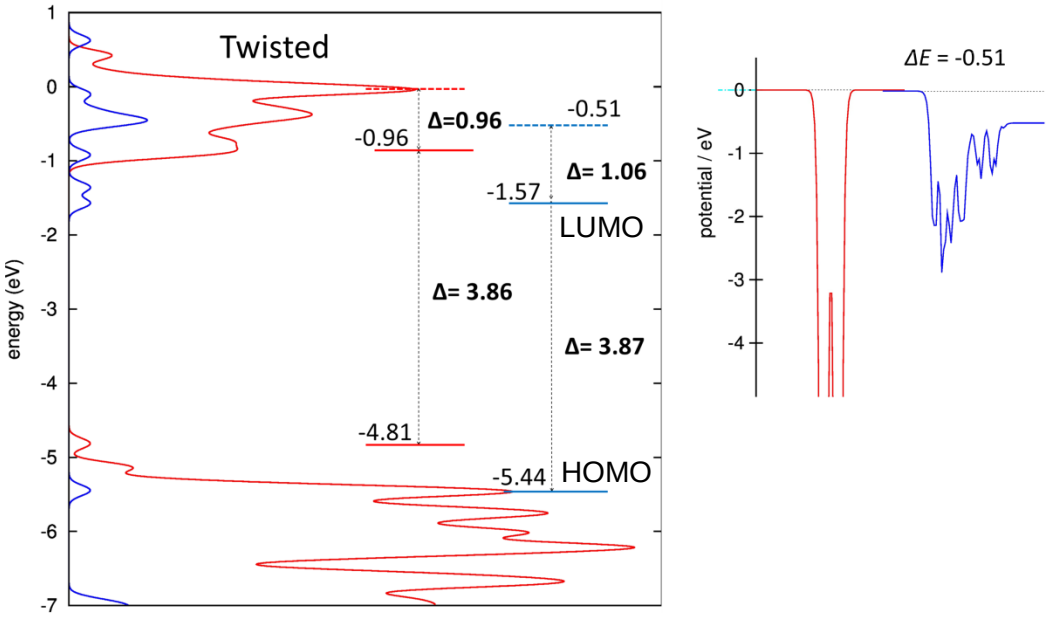

FIGURE 5.28 The DOS for the relaxed NiO surface (red) and twisted TPA–PYR (blue) are on the left; the planar averaged electrostatic potential is on the right. The VBM (solid red), CBM (solid red), HOMO (solid blue), LUMO (solid blue), and the change in the electrostatic potential (dashed red and dashed blue) are marked for the NiO and TPA–PYR. The band gap, the HOMO–LUMO gap, and the difference between the vacuum level and CBM or LUMO are marked with Δ. All values are in eV.

First, the electrostatic potential is analyzed and its effects on the vacuum level shift between the two sides of the slab. For TPA–PYR, downshifts of -0.44 eV and -0.51 eV are observed in the relaxed and twisted systems, respectively. The downshift goes from the left to the right of the molecule (from the anchoring group to the TPA); hence, the dipole moment is from TPA to PYR, thus leading to the situation in which the PYR, i.e., anchoring group is the negative part. In fact, it is confirmed by the Mulliken population analysis, which shows that the anchoring group receives 0.07 electrons, both in the relaxed and twisted structures. Thus, the change of the potential is due to the dipole moment (due to the electron rearrangement) of the single molecule. The small change (0.07 eV) in the electrostatic potential between the relaxed and the twisted TPA–PYR can be explained by the geometrical torsion.

As the main point of this thesis is the energy level alignment between the two, the DOS is analyzed. In the case of PYR as the anchoring group and considering the isolated

components, the HOMOs of the relaxed and twisted dye molecules lie at 0.52 eV and 0.63 eV, respectively. Lower energy of HOMO with respect to the VBM of NiO makes it possible for the thermodynamic spontaneous injection of the hole from the HOMO to VBM to occur. This is a crucial requirement for the p-type DSSC working mechanism. Therefore, it can be assumed, just by investigating the isolated systems, that the spontaneous hole injection is possible from TPA–PYR to NiO.

5.4.1.2 Interacting system

The chemisorbed TPA–PYR on the NiO(100) is illustrated in Figure 5.29. We observed i) a -0.64 eV downshift on the side of the molecule in the vacuum; henceforth, the dipole moment is toward the surface (i.e., the NiO is the negative part of the system and the TPA–PYR is the positive). This would mean that NiO receives electrons from the dye molecule, which is the opposite behavior of the system. Unfortunately, Mulliken population analysis indicated that the NiO donates 0.14 electrons to the TPA–PYR, or in other words, the surface is positively charged. However, what phenomenon causes the shift in the electrostatic potential, since it states that the dye molecule should be the positive part of the system? Further investigation shows that the TPA–PYR goes through an electron rearrangement: PYR accepts 0.18 electrons and TPA donates 0.04 electrons inside the dye molecule. Under those circumstances, the anchoring group is the most negative part of the system, as it accepts electrons from both the surface and TPA moiety. Thus, it is assumed that the dipole moment of the dye molecule dominates the dipole moment of the interacting system. Another key point that supports the claim is the electrostatic shift because the difference is small: 0.20 eV (relaxed) and 0.13 eV (twisted), compared to the isolated systems.

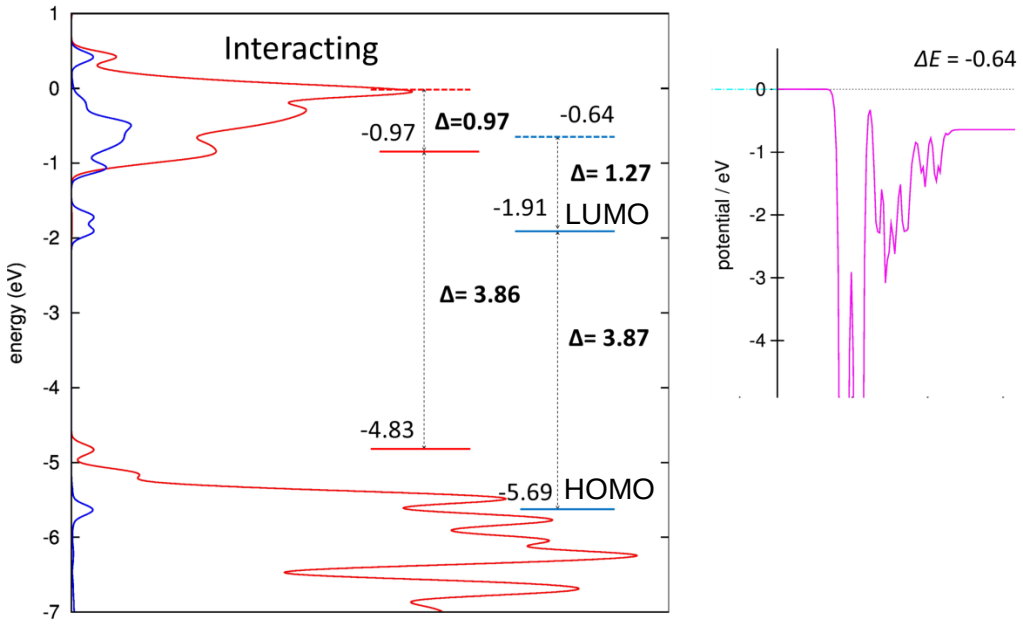

FIGURE 5.29 The DOS for the relaxed system of the TPA–PYR (blue) on the NiO surface (red) is on the left and the planar averaged electrostatic potential (magenta) is on the right. The VBM (solid red), CBM (solid red), HOMO (solid blue), LUMO (solid blue), and the change in the electrostatic potential (dashed red and dashed blue) are marked for the NiO and TPA–PYR. The band gap, HOMO–LUMO gap, and the difference between the vacuum level and CBM or LUMO are marked with Δ. All values are in eV.

Another observation from Figures 5.27–5.29 is that the DOS of the NiO interacting with TPA is similar to that of isolated NiO regarding the energy level alignment. In addition, the energy level alignment of the TPA and NiO is similar to the previously discussed isolated systems. Due to the downshift (-0.64 eV) of vacuum (i.e., the shift in the electrostatic potential), the HOMO of the dye decreased. Now, it lies 0.88 eV below the VBM and the spontaneous CT is easily enabled. The TPA shows no major changes in its electronic structure near the VBM region. However, the position of the HOMO level with respect to the vacuum is affected (i.e., the energy of HOMO decreases from 0.80 eV (relaxed) to 0.60 eV (twisted)). The shifts are rigid between the systems because the difference in energy, such as the HOMO–LUMO gap, do not change. The results suggest that the TPA–PYR rests on the surface with a minimal amount of interaction (Mulliken population analysis). The adsorption energies of the dye molecule were also calculated. They are -1.14 eV and -1.27 eV for relaxed and twisted, respectively.

To conclude, the energy levels of the dye molecule in the interacting system shifted due to the change in the electrostatic potential. This outcome is shown in Figures 5.27–5.29, which demonstrates that the shifts in the vacuum are rigid between the systems. The twisting pushes energy levels or TPA–PYR deeper, but they remain at the same scale between all three systems. Therefore, TPA–PYR rests on the surface and has minimal interaction with the surface through the chemisorption.

5.4.2 1,2-Diol

The effect of the second chemisorbed anchoring group on the surface, which is DIOL, was studied. The models of the systems are seen in Figures 3.8 and 3.12 and the results in Figures 5.30–5.33. Unlike PYR, DIOL has hydrogens on hydroxyl groups; thus, the hydrogens are removed from the anchoring group before chemisorption and a neutral molecule (radical) is created. The effect of the hydrogen removal is investigated (Figure 5.31) by taking a single point of the relaxed structure without hydrogens. The electrostatic potential is shown only as a number from now on.

5.4.2.1 Isolated dye molecule

The results are presented in Figures 5.30–5.32. The electrostatic potential was analyzed first. For the TPA–DIOL, an upshift of +0.06 eV and downshifts of -1.95 eV, and -1.57 eV are noted in a relaxed, relaxed without hydrogens, and twisted dye molecule, respectively. Accordingly, the relaxed TPA–DIOL has a small dipole moment from DIOL (positive moiety) to TPA (negative moiety). In contrast, relaxed without hydrogens (Figure 5.31) and twisted (Figure 5.32) TPA–DIOLs show that the anchoring group is the negative moiety. As a matter of fact, removing the hydrogens has the greater impact than twisting the structure, because (-1.95 eV) < (-1.57 eV).

Due to the (small) shift in the vacuum, it is clear that the anchoring group is barely drawing the electrons from the structure. As a matter of fact, Mulliken's population analysis proves it: Inside the relaxed structure, DIOL receives 0.01 electrons, which is also directly proportional to the upshift. In contrast, DIOL without the hydrogens receives 0.26 electrons and the DIOL inside the twisted system receives 0.15 electrons, which are also directly proportional to the downshifts. Figures 5.30–5.32 show the partial DOS of the isolated compounds alongside the HOMO and VBM of dye and NiO, respectively. In Figure 5.30, the HOMO is above VBM by 0.31 eV; thus, the electron from VBM has to overcome an energy barrier of the same value for the spontaneous

CT. For the next two cases, relaxed without hydrogen and twisted, the situation is the opposite (Figures 5.31 and 5.32), because HOMOs are below the VBM. Now the spontaneous CT is possible.

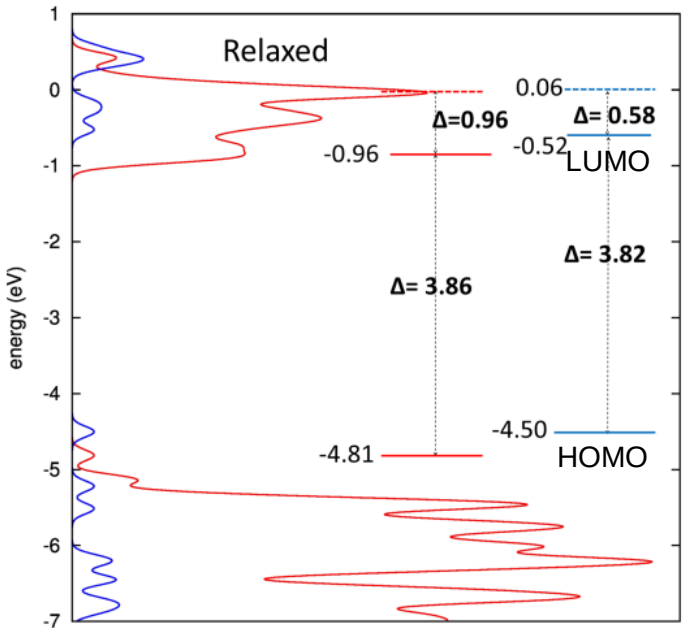

FIGURE 5.30 The DOS for a relaxed NiO surface (red) and relaxed TPA–DIOL (blue). VBM (solid red), CBM (solid red), HOMO (solid blue), LUMO (solid blue), and the change in the electrostatic potential (dashed red and dashed blue) are marked for the NiO and TPA–DIOL. The band gap, HOMO–LUMO gap, and the difference between the vacuum level and CBM or LUMO are marked with Δ. The empty gap states are marked with a broken blue line. All values are in eV.

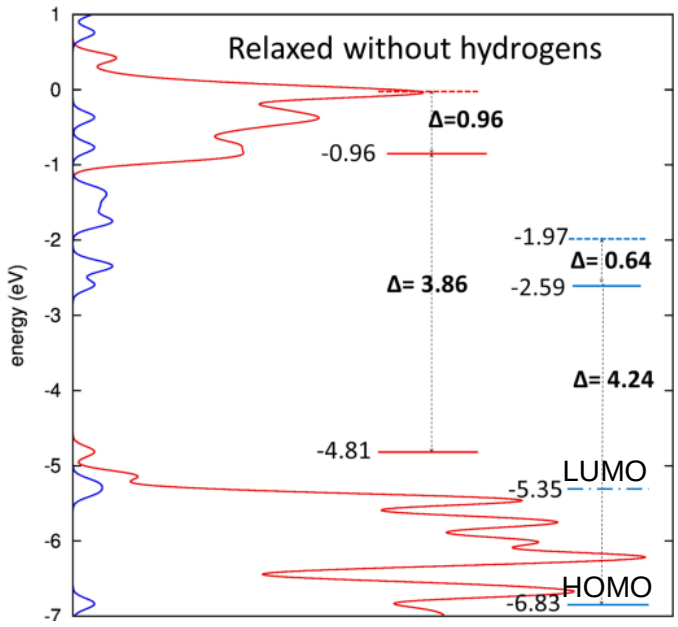

FIGURE 5.31 The DOS for a relaxed NiO surface (red) and relaxed without hydrogens TPA–DIOL (blue). VBM (solid red), CBM (solid red), HOMO (solid blue), LUMO (solid blue), and the change in the electrostatic potential (dashed red and dashed blue) are marked for the NiO and TPA–DIOL. The band gap, HOMO–LUMO gap, and the difference between the vacuum level and CBM or LUMO are marked with Δ. Empty gap states are marked with a broken blue line. All values are in eV.

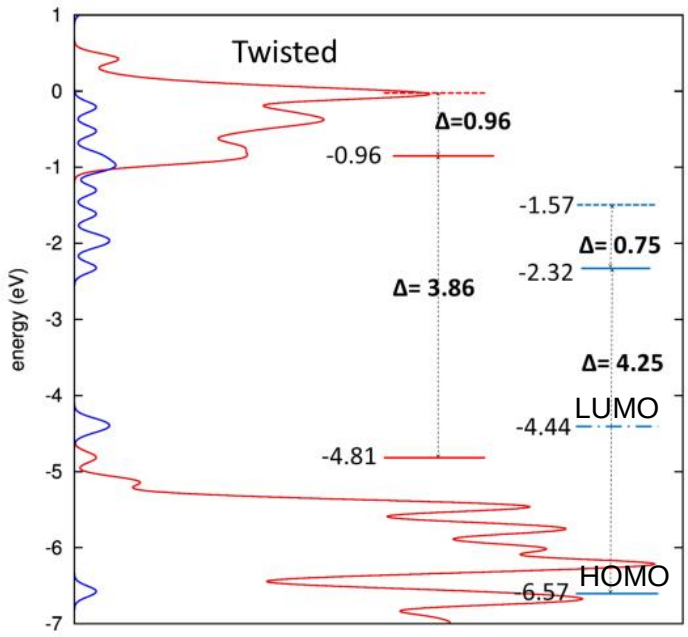

FIGURE 5.32 The DOS for a relaxed NiO surface (red) and twisted TPA–DIOL (blue). VBM (solid red), CBM (solid red), HOMO (solid blue), LUMO (solid blue), and the change in the electrostatic potential (dashed red and dashed blue) are marked for the NiO and TPA–DIOL. The band gap, HOMO–LUMO gap, and the difference between the vacuum level and CBM or LUMO are marked with Δ. Empty gap states are marked with a broken blue line. All values are in eV.

However, in the last two cases, two states appear inside the HOMO–LUMO gap: -5.35 eV in relaxed without hydrogens and -4.44 eV in twisted. Further investigation with eigenvectors shows that the states are empty states (LUMOs) and are localized on the anchoring group. They can act as possible trap states if they are present inside the interacting system and above the VBM, as seen in Figure 5.32. This is due to the following reaction: When the electron is excited above the LUMO level, it is possible that it relaxes on these empty states instead of the actual LUMO (-2.59 eV and -2.32 eV in relaxed without hydrogens and twisted) and back to VBM, if the NiO has already injected the electron on the HOMO. Otherwise, the energy level alignment is desirable, as the VBM is higher in energy than HOMO. As in the previous case, it is expected that the energy level alignment does not change when switching to the interacting system.

5.4.2.2 Interacting system

Now that the TPA–DIOL is chemisorbed on the surface, the following is observed according to Figure 5.33: i) the change in electrostatic potential (-1.37 eV) is closest to the isolated twisted system (-1.57 eV). Second, the downshift is along the side of the molecule, so the molecule is the positive part and the surface is the negative part in the interacting system. Again, this finding is opposite the outcome of the Mulliken population analysis, which shows that the surface donates 0.20 electrons to the dye molecule. For this reason, the intramolecular CT is investigated as in the previous case. Indeed, it shows that DIOL receives 0.96 electrons and TPA loses -0.75 electrons. This is a magnitude of 1 electron CT inside the dye molecule. It is clear that, especially in this case, the intramolecular CT and the dipole moment of the isolated dye dominate the shift in the vacuum.

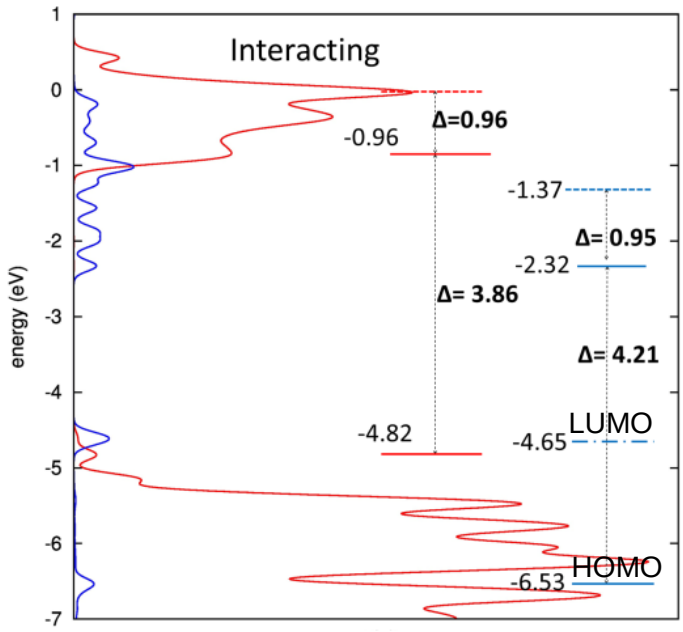

FIGURE 5.33 The DOS for the relaxed system of TPA–DIOL (blue) on the NiO surface (red). VBM (solid red), CBM (solid red), HOMO (solid blue), LUMO (solid blue), and the change in the electrostatic potential (dashed red and dashed blue) are marked for the NiO and TPA–DIOL. The band gap, HOMO–LUMO gap, and the difference between the vacuum level and the CBM or LUMO are marked with Δ. Empty gap states are marked with a broken blue line. All values are in eV.

Similar to TPA–PYR, the energy level alignment of TPA–DIOL has not changed in respect to the isolated, twisted, and dye without hydrogens cases. Also, the shape of the DOS is similar to the same isolated cases, which means that an empty state (-4.65 eV in Figure 5.33) is present and is 0.17 eV above the VBM. As predicted, they are possible trap states within the p-DSSC. Otherwise, the energy level alignment is desired because the VBM is above the HOMO. Finally, the adsorption energies are -4.38 eV and -1.42 eV for relaxed without hydrogens and twisted, respectively. Interestingly, the values show that the binding of the DIOL anchoring group should be stronger without twisting. Thus, when comparing it to the TPA–PYR, it can be said that the DIOL binds stronger to the NiO surface.

To summarize, the TPA–DIOL behaves in a similar manner as TPA–PYR, where the dipole moment of the dye molecule dominates the dipole moment inside the interacting system. In contrast to the TPA–PYR, intramolecular CT is stronger, which is explained by the Mulliken population analysis. It shows that approximately one electron is donated inside the TPA–DIOL, which is a greater amount than in TPA–PYR. Otherwise, the interaction with the surface is minimal as the intermolecular CT transfer is small: 0.21 electrons are transported between the surface and the dye molecule. Thus, despite the favorable energy-level alignment, trap states exists inside the gap.

5.4.3 Carboxylate

The last anchoring group that we investigated is CARB, which is most commonly used for dye molecules in DSSC applications. The models for the anchoring group are presented in Figures 3.8 and 3.12, and the results (DOS) appear in Figures 5.34–5.37. Again, the TPA–CARB is studied as an isolated molecule (relaxed, without hydrogens, and twisted) and chemisorbed on the surface.

5.4.3.1 Isolated dye molecule.

The DOSs are shown in Figures 5.34–5.36 for the isolated systems. In all cases, observed downshifts are on the side of the TPA as follows: -0.26 eV (relaxed), -1.59 eV (without hydrogen), and -2.05 eV (twisted). Therefore, in all cases the dipole moment occurs from the TPA (positive moiety) to the CARB (negative moiety). Again, this is confirmed by the Mulliken population analysis, as the CARB receives 0.28 (relaxed),

0.91 (without hydrogen), and 0.87 (twisted) electrons from the TPA moiety. From these results, it is evident that the removal of the hydrogens has a great impact for the electrostatic potential as the shift decreases from -0.26 eV to -1.59 eV. In addition, the twisting of the geometry lowers the vacuum shift, even though the CT is lower inside the twisted geometry than it is in the TPA–CARB without hydrogens. Therefore, the vacuum shift is a combination of both. As in the cases of PYR and DIOL, it is expected that the results with the interacting system are similar to the twisted TPA–CARB.

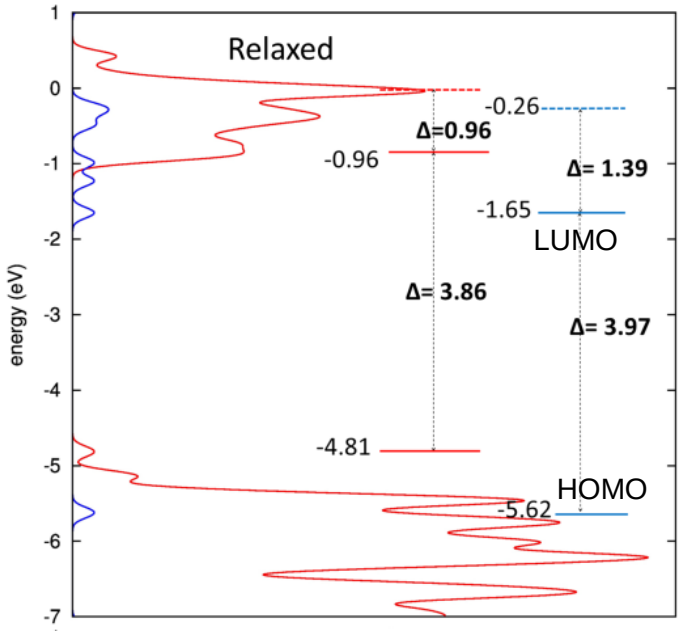

FIGURE 5.34 The DOS for the relaxed NiO surface (red) and relaxed TPA–CARB (blue). VBM (solid red), CBM (solid red), HOMO (solid blue), LUMO (solid blue), and the change in the electrostatic potential (dashed red and dashed blue) are marked for the NiO and TPA–CARB. The band gap, HOMO–LUMO gap, and the difference between vacuum level and CBM or LUMO are marked with Δ. All values are in eV.

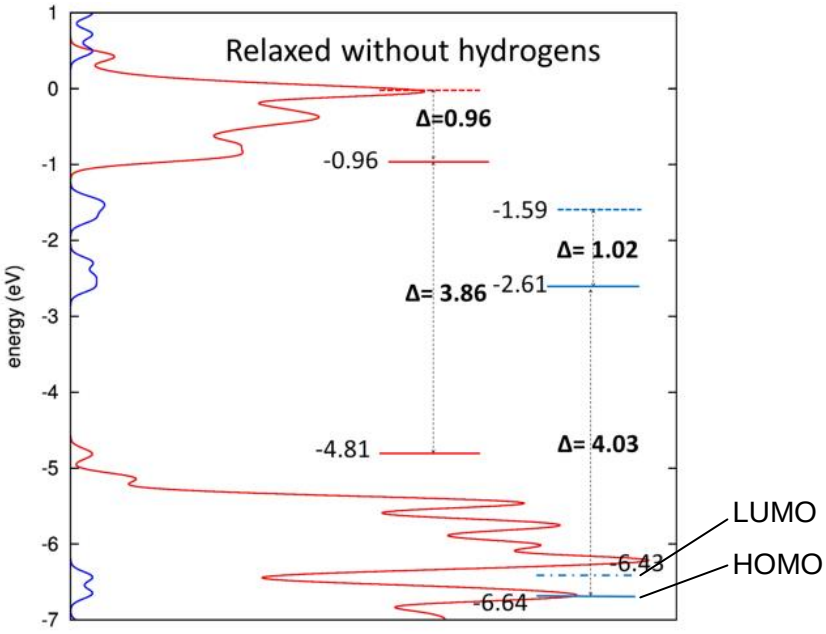

FIGURE 5.35 The DOS for the relaxed NiO surface (red) and relaxed without hydrogens TPA–CARB (blue). VBM (solid red), CBM (solid red), HOMO (solid blue), LUMO (solid blue), and the change in the electrostatic potential (dashed red and dashed blue) are marked for the NiO and TPA–CARB. The band gap, HOMO–LUMO gap, and the difference between vacuum level and CBM or LUMO are marked with Δ. Empty gap states are marked with a broken blue line. All values are in eV.

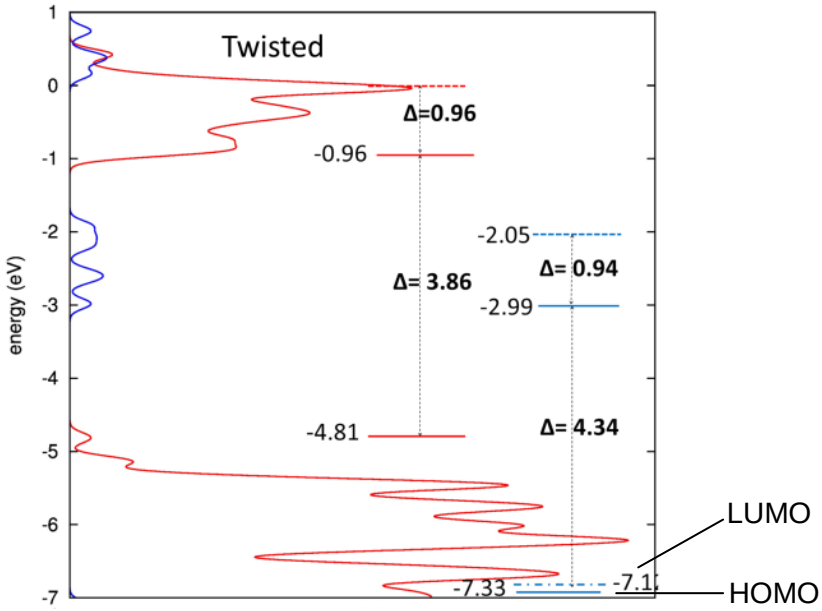

FIGURE 5.36 The DOS for the relaxed NiO surface (red) and twisted TPA–CARB (blue). VBM (solid red), CBM (solid red), HOMO (solid blue), LUMO (solid blue), and the change in the electrostatic potential (dashed red and dashed blue) are marked for the NiO and TPA–CARB. The band gap, HOMO–LUMO gap, and the difference between vacuum level and CBM or LUMO are marked with Δ. Empty gap states are marked with a broken blue line. All values are in eV.

The energy levels of the HOMOs of the isolated TPA–CARBs are lower in energy than the VBM in all cases. As a matter of fact, the downshift pushes the energy levels even deeper inside the VB. As a result, the spontaneous hole injection from the dye molecule to the surface is possible. In addition, the empty states are observed: -6.43 eV and -7.11 eV for relaxed without hydrogens and twisted, respectively. However, they are approximately 0.2 eV above the HOMO of the TPA–CARB and approximately 2.0 eV below the VBM in both cases, so they do not act as trap states. In conclusion, the TPA–CARB shows good properties as an anchoring group in an isolated system.

5.4.3.2 Interacting system

Finally, the TPA–CARB is chemisorbed on the NiO surface (results in Figure 5.37) and drastic changes take place. The most notable is i) the upshift of 0.64 eV along the side of the dye molecule, which means that the surface is the positive moiety of the system.

This is confirmed by the Mulliken population analysis, as the surface loses -1.35 electrons, which is the opposite for the previous anchoring groups PYR and DIOL. Additionally, TPA receives 0.83 electrons; CARB receives 0.52 electrons. As a result, the shift in the vacuum is now the dipole moment of the complete system instead of being dominated by the dye molecule.

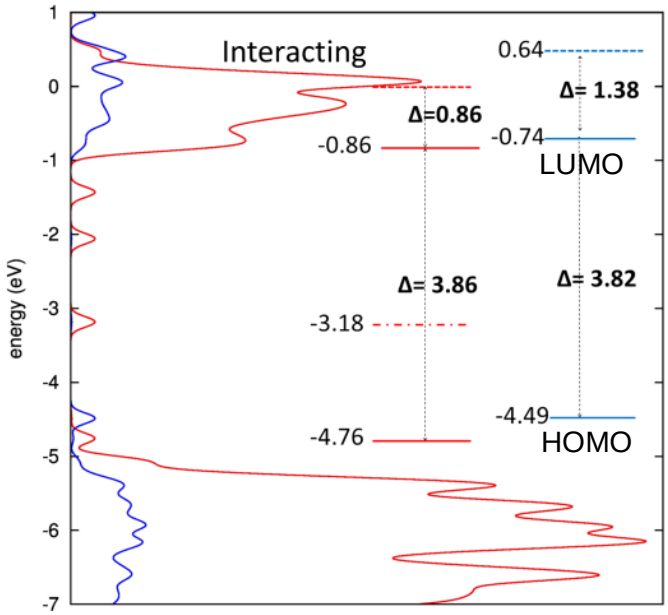

FIGURE 5.37 The DOS for the relaxed system of TPA–CARB (blue) on the NiO surface (red). VBM (solid red), CBM (solid red), HOMO (solid blue), LUMO (solid blue), and the change in the electrostatic potential (dashed red and dashed blue) are marked for the NiO and TPA–CARB. The band gap, HOMO–LUMO gap, and the difference between the vacuum level and CBM or LUMO are marked with Δ. Empty gap states are marked with a broken red line. All values are in eV.

Unfortunately, the upshift of the vacuum increases the energy levels of TPA–CARB. Even though the shape of the energy levels is similar, the HOMO is 0.27 eV above the VBM. Therefore, the electron has to go through an energy barrier in order to have a spontaneous CT between the dye and SC. Secondly, (empty) gap states (from the surface) are seen in Figure 5.37. Since they are empty, they can act as a possible trap state, as in the case of TPA–DIOL. As a result, the energy level alignment of the TPA–CARB does not support the spontaneous CT reaction inside p-DSSCs. The adsorption energies are -4.13 eV for both relaxed without hydrogens and twisted structures. It is clear that the CARB binds the strongest to the surface when comparing the values with

PYR and DIOL. Therefore, CARB has the strongest interaction with the surface, even though the energy level alignment is unfavorable.

To summarize, the results of the TPA–CARB intermolecular CT explains the upshift of the combined system. This is presented by the Mulliken population analysis. Even though this outcome may be true, the energy level alignment does not support spontaneous CT because the HOMO of TPA–CARB is higher in energy than the VBM of NiO. Nevertheless, a pristine NiO(100) surface was used as a model, although in practice NiO(100) is doped. The presence of dopants could increase the VBM and make it possible for a spontaneous CT, as in the case of CARB.

5.4.3.3 Summary

Under these circumstances, calculations show that PYR is the best anchoring group. First, the energy level alignment supports spontaneous CT. Second, it does not create trap states during the interaction with the surface. Lastly, it draws electrons from the surface to the dye molecule. However, PYR does not bind as strongly as other anchoring groups on the surface, as seen in Table 5.8. CARB has the strongest binding and strongest interaction with the surface (Mulliken population analysis). However, its energy level alignment does not support spontaneous hole injection.

Table 5.8 Adsorption energies (in eV) for different anchoring groups in relaxed (without hydrogens) and twisted geometries.

	PYR	**DIOL**	**CARB**
Relaxed	-1.14	-4.38	-4.13
Twisted	-1.27	-1.42	-4.13

It is very intriguing to see the opposite properties with two anchoring groups; thus, it would be interesting to theoretically study PYR when it is in greater contact with NiO with different dye molecules.

6 Conclusions

Solar cells are gaining an increasing amount of interest. One of the possibilities is to use dye-sensitized solar cells because they are flexible, tunable, and environmentally friendly. This study focused on p-type dye-sensitized solar cells since they are not as widely studied as n-type dye sensitized solar cells, yet an efficient p-DSSC is needed for pn-DSSC to reach its theoretical (40%) efficiency. The aim is to understand electronic interactions when the dye molecule is in contact with the semiconductor surface so that the phenomena which affect the CT can be addressed. The compounds presented in this thesis are studied for the first time, with B3LYP, linear combination of atomic orbitals (LCAO), and CRYSTAL09 altogether. Also, these dye-semiconductor systems—especially these—are not widely studied by modeling.

The study was done completely via computational methods mentioned above. First, the minimum energy geometries, electronic structures, and excitations of boron-dipyrrolemethene (BODIPY) and its derivatives were investigated. The aim of this research was to suggest a molecule for synthesis. Also, semiconductor surfaces, titanium dioxide and nickel oxide (TiO_2 and NiO), were modeled and relaxed and their electronic structures were studied. NiO was studied to determine the differences between the pristine and interacting surface. In the case of TiO_2, the aim was to investigate whether or not nitrogen doping could enhance TiO_2 as an electrode for p-DSSC. Finally, four derivatives of perylene monoimide (PMI) and three anchoring groups (carboxyl, 1,2-diol, pyridine) based on trisphenyl amine (TPA) were crafted on the NiO(100) surface to gain information regarding whether or not the energy level alignment favors spontaneous CT (*E[valence band maximum] > E[highest occupied molecular orbital]*) and if the surface and dye molecule interact (intermolecular electron rearrangement).

Derivatives of BODIPY show alterations between the structural changes. The visible changes are within the electron density and energy levels of orbitals. First, the strongest electron transition is inside the donor and the second strongest transition is from

donor to the acceptor. Second, the energy level saturation is observed with an increasing number of thiophene units. Third, the vinylene group makes no difference for the previously studied BODIPY. Fourth, it is desirable for the LUMO to be close to the surface, on the anchoring group, in BODIPY so that the electron is transported closer to the surface: i) the anchoring and ii) the methyl groups remove the localization of the LUMO orbitals. The effect is due to i) the electron withdrawing character of the anchoring group and ii) the steric effect created by the methyl group position. However, the steric effect by the methyl group can lengthen the lifetime of an electron–hole pair; therefore, it is beneficial. iii) The absence of a donor group, TPA, decreases the energy of the HOMO. This is because the HOMO is partially localized on the TPA and the molecule is smaller in comparison to the other screened BODIPY structures. From these results, BODIPY with vinylene (no change) and methyl groups (the lifetime of an electron–hole pair) were chosen as a suggestion for the synthesis. The study of dopants in TiO_2 shows that the substitutional nitrogen at the oxygen site does not distort the lattice. The notable effect of nitrogen doping is visible inside the gap. The (empty) nitrogen states appear near the valence band edge and they can enhance the hole conductivity (p-type).

The studies of chemisorbed PMI and TPA on NiO surface have not widely been performed by LCAO. Hence, the results are intriguing and provide deeper insight into what is happening between the dye molecule and the semiconductor surface. The calculations of the interacting systems show intriguing results of the electronic structure of PMI derivatives and anchoring groups. First, the complete dye molecules (derivatives of the PMI dyes) have unfavorable energy level alignment (the highest occupied molecular orbital is above the valence band maximum) for a spontaneous electron transfer reaction. However, it is shown that the smaller the molecule, the closer it is to the surface and, therefore, it is easier to transfer the charge to the surface. The unfavorable energy level alignment is assumed to be due to the carboxylate, which is supported by the study with the three anchoring groups. The jump in electrostatic potential shows that it is affected by the character of the anchoring group, TPA with pyridine, and 1,2-diolanchoring groups are able to transfer the electron from the semiconductor to the dye molecule due to the favorable energy level alignment because the highest occupied molecular orbital is below the valence band maximum. In contrast, for TPA with a carboxylate anchoring group, it is more difficult to transfer the charge to the semiconductor surface as the energy level alignment is the opposite: The highest molecular orbital is above the valence band maximum. The electrostatic potential is shown to be a result from the dipole moment of the system. The latter is caused either by the intramolecular CT (pyridine or 1,2-diol), intermolecular CT (CARB), or both. Thus, a pyridine anchoring group could show potential, yet it does not bind strongly on the NiO surface.

The study provided lots of new and intriguing information of the functionality of the dye molecules, anchoring groups, and their interactions in contact with the semiconductor surface. To summarize, the study shows that the anchoring group might have a bigger role within the CT reactions than was expected. If the anchoring group draws electrons too very strongly on itself, it pushes the energy levels lower in energy. Removal of hydrogens can create possible trap states after chemisorption. For the future and for the anchoring group, it would be interesting to test other possibilities (e.g., phosphonate) as an anchoring group. Also, pyridine would be interesting to test on a complete dye molecule and with various acceptor and donor groups to see how it interacts with the surface under new circumstances. In addition, it would be interesting to study how the suggested systems work in practice. Finally, the nickel vacancies within the semiconductor surface that are in contact with the dye molecule would be intriguing to research.

References

1. Kontkanen, O.V., Niskanen, M., Hukka, T.I., and Rantala, T.T., Electronic Structure of p-type perylene monoimide-based donor acceptor dyes on the nickel oxide (100) surface: a DFT approach. Physical Chemistry Chemical Physics, 2016. 18: p. 14382.

2. Renewables 2017: Global Status report. http://www.ren21.net/wp-content/uploads/2017/06/17-8399_GSR_2017_Full_Report_0621_Opt.pdf , Accessed: 5.8.2017.

3. When Will Fossil Fuels Run out? http://www.carboncounted.co.uk/when-will-fossil-fuels-run-out.html , Accessed: 5.8.2017.

4. The End of Fossil fuels. https://www.ecotricity.co.uk/our-green-energy/energy-independence/the-end-of-fossil-fuels , Accessed: 5.8.2017.

5. The World Factbook. https://www.cia.gov/library/publications/the-world-factbook/geos/xx.html , Accessed: 6.8.2017.

6. Nattestad, A., Perera, I., and Psiccia, L., Developments in and prospects for photocathodic and tandem dye-sensitized solar cells. Journa Photochemistry Photobiology C, 2016. 28: p. 44.

7. Grätzel, M., Photoelectrochemical cells. Nature, 2001. 414: p. 338.

8. O'Regan, B. and Grätzel, M., A low-cost, high-efficiency solar-cell based on dye-sensitized colloidal TiO_2 films. Nature, 1991. 353: p. 737.

9. Bequerel, E., Recherches sur les effets de la radiation chimique de la lumière solaire, au moyen des courants électriques. Comptes Rendus de l'Académie Des Science, 1839. 9: p. 145.

10. Moser, J., Notiz über Verstärkung photoelektrischer Ströme durch optische Sensibilisirung. Monatshefte für Chemie/Chemical Monthly, 1887. 8(1): p. 373.

11. West, W., First hundred years of spectral sensitization, Photographic Science and Engineering, 1974. 18: p. 35.

12. Chapin, D.M., Fuller, C.S., and Pearson, G.L., Journal of applied physics, 1954. 25: p. 676.

13. Vlachopolous, N., Liska, P., Augustynski, J., and Grätzel, M., Very Efficient Visible Light Energy Harvesting and Conversion by Spectral Sensitization of High Surface Area Polycrystalline Titanium Oxide Films. Journal of American Chemical Society, 1988. 110: p. 1216.

14. Green, M.A., Third generation photovoltaics: ultra-high conversion efficiency at low cost. Progress in Photovoltaic: Research Applications, 2001. 9(2): p. 123.

15. Wenham, S. and Green, M., Silicon solar cells. Progress in Photovoltaics: Research and Applications, 1996. 4(1): p. 3.

16. Zhao, J., Wang, A., and Green, M.A., 24.5% efficiency PERT silicon solar cells on SEH MCZ substrates and cell performance on other SEH CZ and FZ substrates. Solar Energy Materials and Solar Cells, 2001. 66(1): p. 27.

17. Schultz, O., Glunz, S., and Willeke, G., ACCELERATED PUBLICATION: Multicrystalline silicon solar cells exceeding 20% efficiency. Progress in Photovoltaics: Research and Applications, 2004. 12(7): p. 553.

18. Barnham, K.W.J., Mazzer, M., and Clive, B., Resolving the energy crisis: nuclear or photovoltaics? Nature materials, 2006. 5: p. 161.

19. Charles, R.G., Davies, M.L., and Douglas, P. Third generation photovoltaics—Early intervention for circular economy and a sustainable future. in Electronics Goes Green 2016+(EGG), 2016: IEEE.

20. Gibson, E.A., Le Pleux, L., Fortage, J., Pellegrin, Y., Blart, E., Odobel, F., Hagfeldt, A., and Boschloo, G., Role of the Triiodine/Iodine Redpx Couple in Dye Regeneration in p-Type Dye Sensitized Solar Cells. Langmuir, 2012. 28: p. 6485.

21. Shockley, W. and Queisser, H.J., Detailed balance limit of efficiency of p-n junction solar cells. Journal of applied physics, 1961. 32(3): p. 510.

22. Hagfeldt, A., Boschloo, G., Sun, L., Kloo, L., and Pettersson, H., Dye Sensitized Solar Cells. Chemical Reviews, 2010. 110: p. 6595.

23. Yang, W., Noh, J., Jeon, N., Kim, Y., Ryu, S., Seo, J., and Seok, S., High-performance photovoltaic perovskite layers fabricated through intramolecular exchange. Science, 2015. 248: p. 1234.

24. Saliba, M., Orlandi, S., Matsui, T., Aghazada, S., Cavazanni, M., and Nazeeruddin, M., A molecularly engineered hole-transporting material for efficient perovskite solar cells. Nature Energy 2016. 1: p. 15017EP.

25. Li, X., Bi, D., Yi, C., Décoppet, J.-D., Luo, J., Zakeeruddin, S.M., Hagfeldt, A., and Grätzel, M., A vacuum flash–assisted solution process for high-efficiency large-area perovskite solar cells. Science, 2016. 353(6294): p. 58.

26. Fu, N., Huang, C., Liu, Y., Li, X., Lu, W., Zhou, L., Peng, F., Liu, Y., and Huang, H., Organic-free anatase TiO2 paste for efficient plastic dye-sensitized solar cells and low temperature processed perovskite solar cells. ACS Applied Materials & Interfaces, 2015. 7(34): p. 19431.

27. Wu, F., Zhu, L., Zhao, S., Q., S., and Yang, C., Engineering or organic dyes for highly efficient p-type dye-sensitized solar cells. Dyes and Pigments, 2016. 124: p. 93.

28. Odobel, F., Farré, Y., Raissi, M., Fihey, A., Pellegrin, Y., Blart, E., and Jacquemin, D., A blue diketopyrrolopyrrole sensitizer with high efficiency in NiO based dye-sensitized solar cells. ChemSusChem., 2017.

29. Pham, T.T.T., Saha, S.K., Provost, D., Farré, Y., Raissi, M., Pellegrin, Y., Blart, E., Vedraine, S., Ratier, B., Aldakov, D., Odobel, F., and Bouclé, J., Towards Efficient Solid-State p-Type Dye-Sensitized Solar Cells: The Dye Matters. Journal of Physical Chemistry C, 2016.

30. Hagberg, D.P., Jiang, X., Gabrielsson, E., Linder, M., Marinado, T., Brinck, T., Hagfeldt, A., and Sun, L., Symmetric and unsymmetric donor functionalization. comparing structural and spectral benefits of chromophores for dye-sensitized solar cells. Journal of Materials Chemistry, 2009. 19(39): p. 7232.

31. Jain, A., Shin, Y., and Persson, K.A., Computational predictions of energy materials using density functional theory. Nature Reviews Materials, 2016. 1: p. 15004.

32. Balanay, M.P. and Kim, D.-H., Theoretical study on correlations between dye-iodine interactions and open-circuit voltages in dyes containing furan thiophene. Computational and Theoretical Chemistry, 2014. 1029: p. 1.

33. Aryasetiawan, F. and Gunnarsson, O., Electronic structure of NiO in the GW approximation. Physical review letters, 1995. 74(16): p. 3221.

34. Warnan, J., Pellegrin, Y., Blart, E., Zhang, L., Brown, A., Hammarström, L., Jacquemin, D., and Odobel, F., Acetylacetone anchoring group for NiO-based dye-sensitized solar cell. Dyes and Pigments, 2014. 105: p. 174.

35. Wykes, M., Odobel, F., Adamo, C., Ciofini, I., and Labat, F., Anchoring groups for dyes in p-DSSC application: insights from DFT. Journal of Molecular Modeling, 2016. 22(12): p. 289.

36. Ooyama, Y., Inoue, S., Nagano, T., Kushimoto, K., Ohshita, J., Imae, I., Komaguchi, K., and Harima, Y., Dye-Sensitized Solar Cells Based On Donor-Acceptor p-Conjugated Fluorescent Dyes with a Pyridine Ring as an Electron-Withdrawing Anchoring Group. Angewandte Chemie Interntaional Edition, 2011. 123: p. 7567.

37. Baldenebro-López, J., Castorena-González, J., Flores-Holguín, N., Almaral-Sánchez, J., and Glossman-Mitnik, D., Density functional theory (DFT) study of triphenylamine-based dyes for their use as sensitizers in molecular photovoltaics. International journal of molecular sciences, 2012. 13(4): p. 4418.

38. Farré, Y., Zhang, L., Pellegrin, Y., Planchat, A., Blart, E., Boujtita, M., Hammarström, L., Jacquemin, D., and Odobel, F., Second Generation of Diketopyrrolopyrrole Dyes for NiO-Based Dye-Sensitized Solar Cells. The Journal of Physical Chemistry C, 2016. 120(15): p. 7923.

39. Daeneke, T., Yu, Z., Lee, G.P., Fu, D., Duffy, N.W., Makuta, S., Tachibana, Y., Spiccia, L., Mishra, A., Bäuerle, P., and Bach, U., Dominating Energy Losses in NiO p-Type Dye-Sensitized Solar Cells. Advanced Energy Materials, 2015. 5: p. 1401387.

40. Zhang, L. and Cole, J.M., Anchoring groups for dye-sensitized solar cells. ACS Applied Materials & Interfaces, 2015. 7(6): p. 3427.

41. Powar, S., Bhargava, R., Daeneke, T., Götz, G., Bäuerle, P., Geiger, T., Kuster, S., Nüesch, F.A., Spiccia, L., and Bach, U., Thiolate/disulfide based electrolytes for p-type and tandem dye-sensitized solar cells. Electrochimica Acta, 2015. 182: p. 458.

42. Wang, K.-C., Jeng, J.-Y., Shen, P.-S., Chang, Y.-C., Diau, E.W.-G., Tsai, C.-H., Chao, T.-Y., Hsu, H.-C., Lin, P.-Y., P., C., Guo, T.-F., and Wen, T.-C., p-type Mesoscopic Nickel Oxide/Organometallic Perovskite Heterojunction Solar Cells. Scientific Reports, 2014. 4: p. 1.

43. Yella, A., Mai, C.L., Zakeeruddin, S.M., Chang, S.N., Hsieh, C.H., Yeh, C.Y., and Grätzel, M., Molecular engineering of push–pull porphyrin dyes for highly efficient dye-sensitized solar cells: The role of benzene spacers. Angewandte Chemie, 2014. 126(11): p. 3017.

44. Fürer, S.O., Luu, L.Y.N., Bozic-Weber, B., Constable, E.C., and Housecroft, C.E., Improving performance of copper(I)-based dye sensitized solar cells through I^{-3}/I^{-} electrolyte manipulation. Dyes and Pigments, 2016. 132: p. 72.

45. Corani, A., Li, M.-H., Shen, P.-S., Chen, P., Guo, T.-F., El Nahhas, A., Zheng, K., Yartsev, A., Sundström, V., and Ponseca Jr, C.S., Ultrafast Dynamics of Hole Injection and Recombination in Organometal Halide Perovskite Using Nickel Oxide as p-Type Contact Electrode. The Journal of Physical Chemistry Letters, 2016. 7(7): p. 1096.

46. Lasser, L., Ronca, E., Pastore, M., De Angelis, F., Cornil, J.r.m., Lazzaroni, R., and Beljonne, D., Energy Level Alignment at Titanium Oxide–Dye Interfaces: Implications for Electron Injection and Light Harvesting. The Journal of Physical Chemistry C, 2015. 119(18): p. 9899.

47. Mathew, S., Yella, A., Gao, P., Humphry-Baker, R., Curchod, B.F.E., Ashari-Astani, N., Tavernelli, I., Rothlisberger, U., Nazeerudin, M.K., and Grätzel, M., Dye-Sensitized solar cells with 13% efficiency achieved through the molecular engineering or porphyrin sensitizers. Nature Chemistry, 2014. 6: p. 242.

48. DSSC. http://gcell.com/dye-sensitized-solar-cells/advantages-of-dscc/flexible-solar-cells, Accessed: 27.7.2017

49. Niskanen, M., Kuisma, M., Cramariuc, O., Golovanov, V., Hukka, T.I., Tkachenko, N., and Rantala, T.T., Porphyrin adsorbed on the (101 [combining macron] 0) surface of the wurtzite structure of ZnO–conformation induced effects on the electron transfer characteristics. Physical Chemistry Chemical Physics, 2013. 15(40): p. 17408.

50. Yella, A., Lee, H.-W., Tsao, H.N., Yi, C., Chandiran, A.K., Nazeeruddin, M.K., Diau, E.W.-G., Yeh, C.-Y., Zakeeruddin, S.M., and Grätzel, M., Porphyrin-sensitized solar cells with cobalt (II/III)–based redox electrolyte exceed 12 percent efficiency. Science, 2011. 334(6056): p. 629.

51. Rochford, J., Chu, D., Hagfeldt, A., and Galoppini, E., Tetrachelate Porphyrin Chromophores for Metal Oxide Semiconductor Sensitization: Effect of the Spacer Lenght and Anchoring Group Position. Journal of American Chemical Society, 2007. 129: p. 4655.

52. Xu, W., Peng, B., Chen, J., Liang, M., and Cai, F., New triphenylamine-based dyes for dye-sensitized solar cells. The Journal of Physical Chemistry C, 2008. 112(3): p. 874.

53. Le Pleux, L., Smeigh, A.L., Gibson, E., Pellegrin, Y., Blart, E., Boschloo, G., Hagfeldt, A., Hammarström, L., and Odobel, F., Synthesis, photophysical and photovoltaic investigations of acceptor-functionalized perylene monoimide dyes for nickel oxide p-type dye-sensitized solar cells. Energy and Environmenta Science, 2011. 4: p. 2075.

54. Odobel, F., Pellegrin, Y., Gibson, E.A., Hagfeldt, A., Smeigh, A.L., and Hammarström, L., Recent advances and future directions to optimize the performances of p-type dye-sensitized solar cells. Coordination Chemistry Reviews, 2012. 256: p. 2414.

55. Nattestad, A., Mozer, A.J., Fischer, M.K.R., Cheng, Y.-B., Mishra, A., Bäuerle, P., and Bach, U., Highly efficient photocathodes for dye-sensitized tandem solar cells. Nature Materials, 2010. 9: p. 31.

56. Odobel, F., Pellegrin, Y., Anne, F.B., and Jacquemin, D., Molecular engineering of efficient dyes for p-type semiconductor sensitization, in High-Efficiency Solar Cells. 2014, Springer. p. 215.

57. Niedzialek, D., Duchemin, I., de Queiroz, T.B., Osella, S., Rao, A., Friend, R., Blase, X., Kümmel, S., and Beljonne, D., First principles calculations of charge transfer excitations in polymer–fullerene complexes: Influence of excess energy. Advanced Functional Materials, 2015. 25(13): p. 1972.

58. Hahn, T., Geiger, J., Blase, X., Duchemin, I., Niedzialek, D., Tscheuschner, S., Beljonne, D., Bässler, H., and Köhler, A., Does Excess Energy Assist Photogeneration in an Organic Low-Bandgap Solar Cell? Advanced Functional Materials, 2015. 25(8): p. 1287.

59. Pellegrin, Y., Le Pleux, L., Blart, E., Renaud, A., Chavillon, B., Szuwarski, N., Boujtita, M., Cario, L., Jobic, S., and Jacquemin, D., Ruthenium polypyridine complexes as sensitizers in NiO based p-type dye-sensitized solar cells: Effects of the anchoring groups. Journal of Photochemistry and Photobiology A: Chemistry, 2011. 219(2): p. 235.

60. Chang, C.-H., Chen, Y.-C., Hsu, C.-Y., Chou, H.-H., and Lin, J.T., Squaraine-arylamine sensitizers for highly efficient p-type dye-sensitized solar cells. Organic letters, 2012. 14(18): p. 4726.

61. Anne, F.B., Galland, N., and Jacquemin, D., Computing redox potentials for dyes used in p-type dye-sensitized solar cells. International Journal of Quantum Chemistry, 2012. 112(24): p. 3763.

62. Böer, K.W., Survey of semiconductor physics: Electrons and other particles in bulk semiconductors. 1990, New York: Van Nostrand Reinhold.

63. Odobel, F. and Pellegrin, Y., Recent advances in the sensitization of wide-band-gap nanostructured p-type semiconductors. Photovoltaic and photocatalytic applications. The Journal of Physical Chemistry Letters, 2013. 4(15): p. 2551.

64. Nattestad, A., Zhang, X., Bach, U., and Cheng, Y.-B., Dye-sensitized CuAlO2 photocathodes for tandem solar cell applications. Journal of Photonics for Energy, 2011. 1(1): p. 011103.

65. Yu, M., Natu, G., Ji, Z., and Wu, Y., p-type dye-sensitized solar cells based on delafossite CuGaO2 nanoplates with saturation photovoltages exceeding 460 mV. The Journal of Physical Chemistry Letters, 2012. 3(9): p. 1074.

66. Sumikura, S., Mori, S., Shimizu, S., Usami, H., and Suzuki, E., Photoelectrochemical characteristics of cells with dyed and undyed nanoporous p-type semiconductor CuO electrodes. Journal of Photochemistry and Photobiology A: Chemistry, 2008. 194(2): p. 143.

67. Xu, X., Cui, J., Han, J., Zhang, J., Zhang, Y., Luan, L., Alemu, G., Wang, Z., Shen, Y., and Xiong, D., Near field enhanced photocurrent generation in p-type dye-sensitized solar cells. Scientific Reports, 2013. 4: p. 3961.

68. Perera, I.R., Daeneke, T., Makuta, S., Yu, Z., Tachibana, Y., Mishra, A., Bäuerle, P., Ohlin, C.A., Bach, U., and Spiccia, L., Application of the Tris (acetylacetonato) iron (III)/(II) Redox Couple in p-Type Dye-Sensitized Solar Cells. Angewandte Chemie International Edition, 2015. 54(12): p. 3758.

69. Powar, S., Daeneke, T., Ma, M.T., Fu, D., Duffy, N.W., Götz, G., Weidelener, M., Mishra, A., Bäuerle, P., and Spiccia, L., Highly Efficient p-Type Dye-Sensitized Solar Cells based on Tris (1, 2-diaminoethane) Cobalt (II)/(III) Electrolytes. Angewandte Chemie, 2013. 125(2): p. 630.

70. Xu, X., Zhang, B., Cui, J., Xiong, D., Shen, Y., Chen, W., Sun, L., Cheng, Y., and Wang, M., Efficient p-type dye-sensitized solar cells based on disulfide/thiolate electrolytes. Nanoscale, 2013. 5(17): p. 7963.

71. Raja, S., Satheeshkumar, C., Rajakumar, P., Ganesan, S., and Maruthamuthu, P., Influence of triazole dendritic additives in electrolytes on dye-sensitized solar cell (DSSC) performance. Journal of Materials Chemistry, 2011. 21(21): p. 7700.

72. Sun, L., Zhang, T., Zhu, B., Wu, C., Yan, L., and Su, Z., Theoretical design and study on hexamolybdate-based organic-inorganic hybrids with double D-p-A chains for high performance p-type dye-sensitized solar cells (DSSC). Dyes and Pigments, 2017. 137: p. 372.

73. Heimel, G., Salzmann, I., Duhm, S., and Koch, N., Design of Organic Semiconductors from Molecular Electrostatics. Chemistry of Materials, 2011. 23: p. 259.

74. Kahn, A. and Koch, N., Adv. Mater., 2003. 15: p. 271.

75. He, J., Lindström, H., Hagfeldt, A., and Lindquist, S.-E., Dye-sensitized nanostructured tandem cell-first demonstrated cell with a dye-sensitized photocathode. Solar Energy Materials and Solar Cells, 2000. 62: p. 265.

76. Shen, Z.-X., List, R., Dessau, D., Wells, B., Jepsen, O., Arko, A., Barttlet, R., Shih, C., Parmigiani, F., and Huang, J., Electronic structure of NiO: Correlation and band effects. Physical Review B, 1991. 44(8): p. 3604.

77. Shen, Z.-X., List, R., Dessau, D., Arko, A., Barttlet, R., Jepsen, O., Wells, B., and Parmigiani, F., Angle resolved photoemission of NiO (001). Solid state communications, 1991. 79(7): p. 623.

78. Shen, Z.-X., Shih, C., Jepsen, O., Spicer, W., Lindau, I., and Allen, J., Aspects of the correlation effects, antiferromagnetic order, and translational symmetry of the electronic structure of NiO and CoO. Physical review letters, 1990. 64(20): p. 2442.

79. Schrön, A., Granovskij, M., and Bechstedt, F., Influence of on-site Coulomb interaction U on properties of MnO (001) 2× 1 and NiO (001) 2× 1 surfaces. Journal of Physics: Condensed Matter, 2013. 25(9): p. 094006.

80. Lany, S., Osorio-Guillén, J., and Zunger, A., Origins of the doping asymmetry in oxides: Hole doping in NiO versus electron doping in ZnO. Physical Review B, 2007. 75(24): p. 241203.

81. Irwin, M.D., Servaites, J.D., Buchholz, D.B., Leever, B.J., Liu, J., Emery, J.D., Zhang, M., Song, J.-H., Durstock, M.F., and Freeman, A.J., Structural and electrical

functionality of NiO interfacial films in bulk heterojunction organic solar cells. Chemistry of Materials, 2011. 23(8): p. 2218.

82. Greiner, M.T., Helander, M.G., Wang, Z.-B., Tang, W.-M., and Lu, Z.H., Effetcs of Processing Conditions on the Work Function and Energy-Level Alignment of NiO Thin Films. Journal of Physical Chemistry C, 2010. 114: p. 19777.

83. Kuhlenbeck, H., Odörfer, G., Jaeger, R., Illing, G., Menges, M., Mull, T., Freund, H.-J., Pöhlchen, M., Staemmler, V., Witzel, S., Scharfschwerdt, C., Wennemann, K., Liedtke, T., and Neumann, M., Molecular adsorption on oxide surfaces: Electronic structure and orientation of NO on NiO(100)/Ni(100) and NiO(100) as determine from electron spectroscopies and ab initio cluster calculations. Physical Review B., 1991. 43(3): p. 1969.

84. Jiang, H. and Shen, Y.-C., Ionization potentials of semiconductors from first-principles. The Journal of Chemical Physics, 2013. 139(16): p. 164114.

85. Wang, P., Guo, Y., Yuan, S., Yan, C., Lin, J., Liu, Z., Lu, Y., Bai, C., Lu, Q., and Dai, S., Advances in the structure and materials of perovskite solar cells. Research on Chemical Intermediates, 2016. 42(2): p. 625.

86. De Angelis, F., Di Valentin, C., Fantacci, S., Vittadini, A., and Selloni, A., Theoretical studies on anatase and less common TiO2 phases: bulk, surfaces, and nanomaterials. Chemical reviews, 2014. 114(19): p. 9708.

87. Mo, S.-D. and Ching, W., Electronic and optical properties of three phases of titanium dioxide: Rutile, anatase, and brookite. Physical Review B, 1995. 51(19): p. 13023.

88. Scanlon, D.O., Dunnill, C.W., Buckeridge, J., Shevlin, S.A., Logsdail, A.J., Woodley, S.M., Catlow, C.R.A., Powell, M.J., Palgrave, R.G., and Parkin, I.P., Band alignment of rutile and anatase TiO2. Nature materials, 2013. 12(9): p. 798.

89. Bai, Y., Mora-Sero, I., De Angelis, F., Bisquert, J., and Wang, P., Titanium dioxide nanomaterials for photovoltaic applications. Chemical reviews, 2014. 114(19): p. 10095.

90. Lee, H.-J., Kim, D.-Y., Yoo, J.-S., Bang, J.-W., Kim, S.-J., and Park, S.-M., Anchoring cadmium chalcogenide quantum dots (QDs) onto stable oxide semiconductors for QD sensitized solar cells. Bulletin of the Korean Chemical Society, 2007. 28(6): p. 953.

91. Tae, E.L., Lee, S.H., Lee, J.K., Yoo, S.S., Kang, E.J., and Yoon, K.B.A., A Strategy To Increase the Efficiency of the Dye-sensitized TiO_2 Solar Cells Operated by Photoexcitation of Dye-to-TiO_2 Charge-Transfer Bands. Journal of Physical Chemistry B, 2005. 109: p. 22513.

92. Martsinovich, N. and Troisi, A., Theoretical studies of dye-sensitised solar cells: from electronic structure to elementary processes. Energy & Environmental Science, 2011. 4(11): p. 4473.

93. Guerrero, G., Alauzun, J.G., Granier, M., Laurencin, D., and Mutin, P.H., Phosphonate coupling molecules for the control of surface/interface properties and the synthesis of nanomaterials. Dalton Transactions, 2013. 42(35): p. 12569.

94. Golovkova, T.A., Kozlov, D.V., and Neckers, D.C., Synthesis and properties of novel fluorescent switches. The Journal of organic chemistry, 2005. 70(14): p. 5545.

95. Arbeloa, T.L., Arbeloa, F.L., Arbeloa, I.L., Garcıa-Moreno, I., Costela, A., Sastre, R., and Amat-Guerri, F., Correlations between photophysics and lasing properties of dipyrromethene–BF 2 dyes in solution. Chemical physics letters, 1999. 299(3): p. 315.

96. Wood, C., Summers, G., and Gibson, E., Increased photocurrent in a tandem dye-sensitized solar cell by modifications in push–pull dye-design. Chemical Communications, 2015. 51(18): p. 3915.

97. Loudet, A. and Burgess, K., BODIPY dyes and their derivatives: syntheses and spectroscopic properties. Chemical reviews, 2007. 107(11): p. 4891.

98. Leen, V., Leemans, T., Boens, N., and Dehaen, W., 2-and 3-Monohalogenated BODIPY Dyes and Their Functionalized Analogues: Synthesis and Spectroscopy. European Journal of Organic Chemistry, 2011. 2011(23): p. 4386.

99. Nicolas Leclere (contact person), http://icpees.unistra.fr/ingenierie-des-polymeres/,Strasbourg group, France.

100. Morandeira, A., Fortage, J., Edvinsson, T., Le Pleux, L., Blart, E., Boschloo, G., Hagfeldt, A., Hammarström, L., and Odobel, F., Improved photon-to-current conversion efficiency with a nanoporous p-type NiO electrode by the use of a sensitizer-acceptor dyad. The Journal of Physical Chemistry C, 2008. 112(5): p. 1721.

101. Sawatzky, G. and Allen, J., Magnitude and origin of the band gap in NiO. Physical review letters, 1984. 53(24): p. 2339.

102. Alders, D., Tjeng, L., Voogt, F., Hibma, T., Sawatzky, G., Chen, C., Vogel, J., Sacchi, M., and Iacobucci, S., Temperature and thickness dependence of magnetic moments in NiO epitaxial films. Physical Review B, 1998. 57(18): p. 11623.

103. Henrich, V. and Cox, P., The Surface Science of Metal Oxides, Cambridge U. New York, 1994.

104. Panepinto, Adriano, PhD student in Université de Mons and studying TiO_2 with nitrogen dopings. Thus, his work is not yet published. He helped to build the models for nitrogen doped TiO_2.

105. Howard, C., Sabine, T., and Dickson, F., Structural and thermal parameters for rutile and anatase. Acta Crystallographica Section B: Structural Science, 1991. 47(4): p. 462.

106. Viitala, M., (2011) First-principles studies of organic adsorption on SnO_2 surfaces. (Tampere University of Technology. Publication; Vol 1018),Tampere University of Technology.

107. Cramer, C.J., Essentials of computational chemistry: theories and models. 2013: John Wiley & Sons.

108. Patterson, J.D., Density-functional theory of atoms and molecules: Robert G. Parr and Weitao Yang. Oxford University Press, New York, and Clarendon Press, Oxford (1989)

109. Cramariuc, O., (2006) Computational Characterization of Photoabsorption and Structure of Porphyrin-Fullerene Dyads. (Tampere University of Technology. Publication; Vol 644),Tampere University of Technology.

110. Leach, A., R., Molecular Modeling: Priciples and Applications. 2nd ed. 2001.

111. Dovesi, R., Saunders, V.R., Roetti, C., Orlando, R., Zicovich-Wilson, C.M., Pascale, F., Civalleri, B., Doll, K., Harrison, N.M., Bush, I.J., D'Arco, P., and Llunell, M., CRYSTAL09, in CRYSTAL09 User's Manual. 2009, University of Torino: Torino.

112. Dovesi, R., Orlando, R., Civalleri, B., Roetti, C., Saunders, V.R., and Zicovich-Wilson, C.M., CRYSTAL: a computational tool for the ab initio study of the electronic properties of crystals. Zeitschrift für Kristallographie-Crystalline Materials, 2005. 220(5/6): p. 571.

113. Becke, A.D., Phys. Re V. A 1988, 38, 3098.(b) Becke. J. Chem. Phys, 1993. 98: p. 5648.

114. Lee, C., Yang, W., and Parr, R.G., Development of the Colle-Salvetti correlation-energy formula into a functional of the electron density. Physical Review B, 1988. 37(2): p. 785.

115. Stephens, P.J., Devlin, F.J., Chabalowski, C.F., and Frisch, M.J., Journal of Physical Chemistry, 1994. 98: p. 11623.

116. Muscat, J., Wander, A., and Harrison, N.M., On the prediction of band gaps from hybrid functional theory. Chemical Physics Letters, 2001. 342: p. 397-401.

117. Towler, M.D., Allan, N.L., Harrison, N.M., Saunders, V.R., Mackrodt, W.C., and Aprà, E., Ab Initio Study of MnO and NiO. Physical Review B, 1994. 50(8): p. 5041.

118. Scaranto, J. and Giorgianni, S., A quantum-mechanical study of CO adsorbed on TiO 2: A comparison of the Lewis acidity of the rutile (110) and the anatase (101) surfaces. Journal of Molecular Structure: THEOCHEM, 2008. 858(1): p. 72.

119. Gatti, C., Saunders, V., and Roetti, C., Crystal field effects on the topological properties of the electron density in molecular crystals: The case of urea. The Journal of Chemical Physics, 1994. 101(12): p. 10686.

120. Peintinger, M.F., Oliveira, D.V., and Bredow, T., Consistent Gaussian basis sets of triple-zeta valence with polarization quality for solid-state calculations. Journal of Computational Chemistry, 2013. 34(6): p. 451.

121. Gaussian 09, R.D., M. J. Frisch, G. W. Trucks, H. B. Schlegel, G. E. Scuseria, M. A. Robb, J. R. Cheeseman, G. Scalmani, V. Barone, B. Mennucci, G. A. Petersson, H. Nakatsuji, M. Caricato, X. Li, H. P. Hratchian, A. F. Izmaylov, J. Bloino, G. Zheng, J. L. Sonnenberg, M. Hada, M. Ehara, K. Toyota, R. Fukuda, J. Hasegawa, M. Ishida, T. Nakajima, Y. Honda, O. Kitao, H. Nakai, T. Vreven, J. A. Montgomery, Jr., J. E. Peralta, F. Ogliaro, M. Bearpark, J. J. Heyd, E. Brothers, K. N. Kudin, V. N. Staroverov, R. Kobayashi, J. Normand, K. Raghavachari, A. Rendell, J. C. Burant, S. S. Iyengar, J. Tomasi, M. Cossi, N. Rega, J. M. Millam, M. Klene, J. E. Knox, J. B. Cross, V. Bakken, C. Adamo, J. Jaramillo, R. Gomperts, R. E. Stratmann, O. Yazyev, A. J. Austin, R. Cammi, C. Pomelli, J. W. Ochterski, R. L. Martin, K. Morokuma, V. G. Zakrzewski, G. A. Voth, P. Salvador, J. J. Dannenberg, S. Dapprich, A. D. Daniels, Ö. Farkas, J. B. Foresman, J. V. Ortiz, J. Cioslowski, and D. J. Fox, Gaussian, Inc., Wallingford CT., 2009.

Tampereen teknillinen yliopisto
PL 527
33101 Tampere

Tampere University of Technology
P.O.B. 527
FI-33101 Tampere, Finland

ISBN 978-952-15-4097-4
ISSN 1459-2045